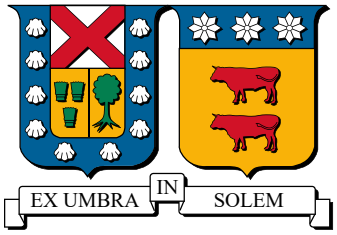

UNIVERSIDAD TÉCNICA
FEDERICO SANTA MARÍA

DEPARTAMENTO DE ELECTRÓNICA

Acoustic Imaging with Distributed Acoustic Sensing Data Using Delay-and-Sum Beamforming in the Time Domain

Master's Thesis

In partial fulfilment of the requirements for the degree of

Ingeniero Civil Electrónico

and the degree of

Magíster en Ciencias de la Ingeniería Electrónica

Author
Diego Alonso Badillo San Juan

Supervisor
Marcelo A. Soto Hernández, PhD

Valparaíso, 2024.

ABSTRACT

Distributed Acoustic Sensing (DAS) is an emerging technology that uses an optical fibre as a distributed vibration sensor. Strain variations in the fibre are measured by phase changes in the reflections captured by an interrogator at one end of the sensing fibre, thanks to Rayleigh back-scattering. These data enable the implementation of array processing algorithms to identify acoustic sources both in the near and far field. However, array processing for DAS data has certain limitations, as the acoustic field is indirectly sampled as longitudinal tension variations in the fibre, which may also experience coupling issues in some sections, complicating the direct application of array processing principles.

Beamforming is an array processing technique that focuses the *listening* capabilities of an array on a specific section of space by introducing phase shifts in the measurements from each sensor. The performance of *delay-and-sum beamforming* applied to DAS measurements is evaluated in a near-field scenario using a public dataset. In this case, a 1500 by 500 metre fibre is interrogated by a DAS sensor to measure controlled acoustic vibrations generated by a truck at various positions, with 55 positions arbitrarily selected for analysis. During the experiment, the fibre also measures vibrations from a distant earthquake, enabling evaluation in a far field scenario.

To overcome the limitations of array signal processing applied to *Distributed Acoustic Sensing*, a channel selection method based on a similarity score, calculated from phase correlation between channels, is implemented, capitalising on the high channel availability in DAS. It is demonstrated that, in most cases, a limited selection of channels improves the estimation of acoustic sources compared to using all available channels. Source localisation is achieved independently by triangulation and beamforming-based acoustic imaging for the near field, with the latter method being the main focus of this thesis, providing the potential for the estimation of multiple sources simultaneously. For the far field, acoustic imaging is employed across a range of propagation speeds and angles to estimate the direction of arrival of an earthquake.

RESUMEN

Distributed Acoustic Sensing (DAS) es una tecnología emergente que utiliza una fibra óptica como sensor distribuido de vibraciones. Las variaciones de tensión en la fibra se miden a través de las variaciones de fase en las reflexiones captadas por un interrogador en un extremo de la fibra de sensado, gracias a la retrodispersión de Rayleigh. Estos datos permiten aplicar algoritmos de procesamiento de arreglos para identificar fuentes acústicas tanto en el campo cercano como en el lejano. Sin embargo, el procesamiento de arreglos en datos DAS presenta ciertas limitaciones, ya que el campo acústico se muestrea indirectamente como variaciones de tensión longitudinal en la fibra, y esta puede tener problemas de acoplamiento en algunas secciones, lo que dificulta la aplicación directa de algunos principios de procesamiento de arreglos.

Beamforming es una técnica de procesamiento de arreglos que enfoca la capacidad de *escuchar* de un arreglo en una sección específica del espacio mediante la introducción de desfases en las mediciones de cada sensor. Se evalúa la técnica *delay-and-sum beamforming* aplicada a mediciones DAS en campo cercano utilizando un conjunto de datos públicos, donde una fibra de 1500 por 500 metros es interrogada por un sensor DAS para registrar vibraciones acústicas controladas generadas por un camión en distintas posiciones, seleccionando 55 de ellas de modo arbirario para análisis. Durante el experimento, la fibra también mide vibraciones de un terremoto ocurrido a una gran distancia de la fibra, lo que permite la evaluación en campo lejano.

Para abordar las limitaciones que enfrenta el uso de procesamiento de arreglos junto a *Distributed Acoustic Sensing*, se implementa un método de selección de canales basado en un puntaje de similitud calculado mediante la correlación de fase entre canales, aprovechando la alta disponibilidad de estos en DAS. Se demuestra que una selección limitada de canales, en la mayoría de los casos, mejora la estimación de fuentes acústicas en comparación con el uso de todos los canales disponibles. La localización de fuentes se logra de manera independiente mediante triangulación e imágenes acústicas basadas en *beamforming* para el campo cercano, siendo este último método el foco principal de esta tesis, proporcionando la potencialidad para la estimación de múltiples fuentes simultáneamente. Para el campo lejano, se emplean imágenes acústicas sobre un rango de velocidades de propagación y ángulos para la estimación de la dirección de llegada de un terremoto.

CONTENTS

Chapter 1

INTRODUCTION

Optical fibres, widely employed in telecommunications, enable the transmission of data over long distances with high bandwidth and minimal loss [1]. One of their primary limitations in this context is the physical phenomenon known as Rayleigh scattering, which causes power attenuation as light propagates through the fibre. Despite being a drawback in telecommunications, Rayleigh scattering can be advantageous in sensing contexts. The back-scattered light within the fibre is highly sensitive to environmental changes, such as temperature, pressure, and strain variations. This sensitivity allows optical fibres to be used for distributed sensing applications, where monitoring changes in back-propagated light enables the detection and measurement of external perturbations. In this context, Distributed Acoustic Sensing (DAS) is an emerging technology that uses optical fibres as vibration sensors, and its applications in a seismic context are evaluated in this thesis.

DAS sensors use phase differences measured by an interrogator at one end of the sensing optical fibre to detect strain variations along discretised sections of the fibre, referred to as channels. In practice, not all available channels provide useful measurements. Poor coupling between the fibre and the ground leads to unpredictable variations in the transfer function that maps phase variations to strain variations, both in gain and frequency response. Even with ideal coupling, the phase extraction process of back-scattered light can cause an uneven longitudinal response. Low-intensity back-scattered light at unpredictable sections of the fibre, caused by fading, results in unreliable phase extraction due to a low signal-to-noise ratio, affecting the reliability of strain estimations. These limitations, combined with the fact that the fibre primarily measures strain in the direction parallel to it, rather than directly sampling the acoustic field via particle displacement, results in different gain directivity for each channel [2, 3, 4]. The distributed nature of this way of using optical fibres as sensors provides a high availability of channels, making it possible to exploit this abundance to design a method that can distinguish, solely using the measurement information from each channel, which channels (i.e., sampled fibre positions) provide useful information and which do not [5].

Array processing [6] involves the use of a sensor array to enhance a signal in terms of signal-to-noise ratio (SNR), compared to a single sensor, by reducing the impact of noise, echoes, and reverberations. Additionally, it aims to characterise the field of waveforms being measured by estimating the directions of arrival for planar waves from the far-field and sources of emission for waves in the near-field, as well as estimating the number of sources when this number is countable. It is logical, therefore, to consider exploiting the high availability of DAS channels, interpretable as point sensors, for applying array processing algorithms. For example, array processing applied to Distributed Acoustic Sensing (DAS) data has been demonstrated as a proof of concept for identifying the direction of arrival of seismic waves [2, 5] and for estimating vehicle speeds on highways using underground optical fibres originally intended for telecommunications [7].

1.1 Objectives and contributions

The primary objective of this thesis is to characterise the acoustic field through imaging via delay-and-sum beamforming in the near field for source location estimation, using measurements from the publicly available PoroTomo dataset [8]. To achieve this, the state-of-the-art channel sorting method for array processing applications in distributed acoustic sensing data is comprehensively evaluated, building on the work presented in [5]. In the PoroTomo dataset, a truck generates broadband chirped acoustic signals from known positions around the fibre, which are measured by each channel, capturing both direct paths and ground reflections. The applicability of DAS measurements for generating near-field acoustic images is explored, explaining the limitations based on array processing theory, thoroughly detailed in its respective chapter, and DAS theory for interpreting the measurements.

Secondary objectives and contributions include evaluating the implementation of the channel sorting method for far-field earthquake characterisation using the same fibre. Additionally, an improvement in computational efficiency for hyperbolic triangulation applied to sorted channels is implemented, demonstrating that a reduced number of channels is sufficient to obtain statistically equal or better estimates for 55 arbitrarily selected source locations. Lastly, the thesis summarises important array processing concepts such as spatial aliasing, spatial resolution, and array geometry-induced ambiguities to understand and interpret the results, focusing on irregular arrays for application in scattered channels of an optical fibre.

1.2 Structure

The following is an outline of the remaining chapters that comprise this thesis:

- **Chapter 2: Wave Propagation Properties.** Fundamental concepts for wave propagation are defined, with an emphasis on terminology that will be utilised in subsequent chapters, such as for seismic waves and light propagating in an optical fibre.
- **Chapter 3: Array Processing.** The theory of sensor arrays necessary to correctly interpret results from beamforming techniques is introduced, with a focus on irregular arrays. Additionally, time domain delay-and-sum beamforming simulations are carried out to support the array processing theory.
- **Chapter 4: Distributed Acoustic Sensing.** An overview of the principles of Distributed Acoustic Sensing interrogation is presented, including details on how to retrieve strain variations at successive fibre sections from back-scattered Rayleigh scattering.
- **Chapter 5: Analysis of *DAS* Measurements.** The results of applying delay-and-sum beamforming to Distributed Acoustic Sensing data for seismic source estimation are discussed for both near and far field scenarios, following the work in [5].
- **Chapter 6: Conclusions.** A discussion of the main findings of the thesis is presented, suggesting directions for future research.

Chapter 2

WAVE PROPAGATION PROPERTIES

Wave propagation properties play a crucial role in many areas of science and engineering, from acoustics and optics to seismology and electromagnetism. Understanding these properties requires the use of mathematical models that accurately represent the behaviour of waves in various media.

Properties such as reflection, refraction, and attenuation of waves as they propagate in a medium can be exploited for non-invasive examination of a medium. For non-invasive inspection of a coaxial cable, a voltage pulse can be sent from one end and the resulting reflections are measured at the same end. By knowing the propagation speed of the pulse in the cable, it is possible to estimate the locations of impedance discontinuities. A similar concept is applicable to mechanical waves propagating through an elastic medium,[1] which makes non-invasive inspection of a terrain possible [9, 10, 11].

2.1 Coordinate systems

Depending on the context, a Cartesian or a spherical coordinate system may be used to represent space. Cartesian coordinates are represented by $\vec{x} = (x, y, z)$, with mutually perpendicular axes (as illustrated in Fig. 2.1). Spherical coordinates are denoted as (r, θ, ϕ), radius, azimuth and elevation respectively. In some literature the elevation angle ϕ may be defined starting from the z axis.

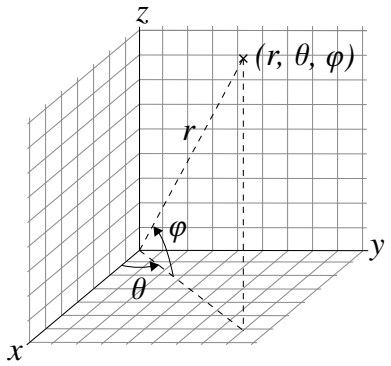

Fig. 2.1: Spherical (r, θ, ϕ) and Cartesian coordinates (x, y, z). Adapted from [12].

[1] A medium that has the ability to recover its original shape after being deformed.

The conversion from one system of coordinates to the other can be deduced using trigonometry:

$$x = r\cos\phi\cos\theta \tag{2.1.1a}$$
$$y = r\cos\phi\sin\theta \tag{2.1.1b}$$
$$z = r\sin\phi \tag{2.1.1c}$$

The use of each system of coordinates will depend on the situation. Spherical coordinates may be convenient when analysing the propagation from an isotropic source, by defining the origin on the source. Throughout this work, spherical coordinates will be used to identify directions of arrival of *plane waves* in the *far-field* scenario, which is explained further in Section 2.2.1.

2.2 Classification of waves based on distance from the source

Let $s(\vec{x}, t)$ be a signal propagating through space, then it satisfies Equation 2.2.1. This equation is known as the *wave equation*, and holds true both for electromagnetic waves and mechanical waves, where c is the wave propagation speed in the medium. In acoustics, for example, $s(\vec{x}, t)$ represents the sound pressure at a given point in space and time [6, 13].

$$\nabla^2 s = \frac{\partial^2 s}{\partial x^2} + \frac{\partial^2 s}{\partial y^2} + \frac{\partial^2 s}{\partial z^2} = \frac{1}{c^2}\frac{\partial^2 s}{\partial t^2} \tag{2.2.1}$$

2.2.1 Far field and plane waves

It can be shown that Equation (2.2.2) is a solution to the wave equation, where $\vec{k} = (k_x, k_y, k_z)$ is a constant vector called *wave propagation constant*. The *slowness vector* is defined as $\vec{\alpha} = \vec{k}/\omega$, with its magnitude reciprocal to the speed of propagation $|\vec{\alpha}| = 1/c$ [6].

$$s(\vec{x}, t) = Ae^{j(\omega t - \vec{k}\cdot\vec{x})} = Ae^{j\omega(t - \vec{\alpha}\cdot\vec{x})} \tag{2.2.2}$$

This solution receives the name *plane wave* because at any given instant of time t_0 where the dot product $\vec{k}\cdot\vec{x}$ is constant, $s(\vec{x}, t_0)$ gets the same value. Note that

$$\vec{k}\cdot\vec{x} = (k_x, k_y, k_z)\cdot(x, y, z) = k_x x + k_y y + k_z z = C \tag{2.2.3}$$

is the equation defining a plane, with $\vec{k}$ representing a normal vector to it, and C being a constant.

A remarkable deduction can be made from the wave equation (2.2.1). Since the partial derivative operator is linear and all other operations present in the wave equation, such as addition and multiplication by a constant, are also linear, any two signals $s_1(\vec{x}, t)$ and $s_2(\vec{x}, t)$ that satisfy the wave equation can be combined linearly to form a new solution $as_1(\vec{x}, t) + bs_2(\vec{x}, t)$, where a and b are scalars. This linearity can be exploited further by expressing a periodic signal as an infinite linear combination of complex exponential functions, which already are solutions to the wave equation.

$$s(\vec{x}, t) = s(t - \vec{\alpha}\cdot\vec{x}) = \sum_{-\infty}^{\infty} S_n e^{jn\omega_0(t - \vec{\alpha}\cdot\vec{x})} \tag{2.2.4}$$

Equation (2.2.4) has the complex exponential form of the Fourier, with fundamental frequency ω_0, meaning that $s(\vec{x}, t)$ can represent any periodic signal. The coefficients S_n can be calculated using

the orthogonal projection of $s(u)$ over the span of the exponential bases [14], and $n \in \mathbb{N}_0$.

$$S_n = \frac{1}{T}\int_{t_0}^{t_0+T} s(u)e^{-jn\omega_0 u}du \tag{2.2.5}$$

As a matter of fact, $s(\vec{x},t)$ is not restricted to be a periodic signal. By generalising Equation (2.2.4) to a continuous linear combination of exponentials, $s(\vec{x},t)$ can be any signal with an arbitrary non-periodic shape. Let

$$s(\vec{x},t) = s(t-\vec{\alpha}\cdot\vec{x}) = \frac{1}{2\pi}\int_{-\infty}^{\infty} S(\omega)e^{j\omega(t-\vec{\alpha}\cdot\vec{x})}d\omega \tag{2.2.6}$$

where the coefficients $S(\omega)$ are given by the Fourier transform

$$S(\omega) = \int_{-\infty}^{\infty} s(t)e^{-j\omega t}dt. \tag{2.2.7}$$

The linearity of the wave equation also implies that even an uncountable number of waves propagating in different directions can coexist, superposing constructively and destructively. This other important conclusion will be capitalised on in Chapter 3, where arrays of sensors are used to spatially filter signals arriving from different directions.

Far field

The term "far field" defines the space where waves propagate at a significant distance from their source, while the "near field" denotes the region proximal to the source of propagation, where the waves are more influenced by its exact location. There is no exact distance at which the far field starts and the near field ends, however, in antenna design theory, the far field is defined to start at the Fraunhofer distance $d_F = 2D^2/\lambda$, where D equals the length or diameter of the antenna, and λ is the wavelength [15]. In acoustics, the same Fraunhofer distance can be used to differentiate the near field form the far field, where D is the length of the transducer used to measure the acoustic waves [16].

Plane waves are used to model waves in the far field because the curvature of the wavefronts becomes negligible, and the wavefronts approximate to parallel planes (see Fig. 2.2). Spherical coordinates θ and ϕ are convenient to represent plane waves when only the direction of propagation is of interest.

Fig. 2.2: Spherical waves are used to model waves in the near field, while plane waves are used to model waves in the far field. Vector $\vec{k}$ is parallel to the direction of propagation at each point.

2.2.2 Near field and spherical waves

The wave equation (2.2.1) can be rewritten using spherical coordinates as follows.

$$\frac{1}{r^2}\frac{\partial}{\partial r}\left(r^2\frac{\partial s}{\partial r}\right)+\frac{1}{r^2\cos\phi}\frac{\partial}{\partial\phi}\left(\cos\phi\frac{\partial s}{\partial\phi}\right)+\frac{1}{r^2\cos^2\phi}\frac{\partial^2 s}{\partial\phi^2}=\frac{1}{c^2}\frac{\partial^2 s}{\partial t^2} \tag{2.2.8}$$

Since we are interested in the spherical solution of the wave equation, the value of $s(r,\theta,\phi,t)$ only depends on the radius r, then the constraint $\partial s/\partial\phi = 0$ is added to (2.2.8), which with extra manipulation yields [6]

$$\frac{\partial^2(rs)}{\partial r^2}=\frac{1}{c^2}\frac{\partial^2(rs)}{\partial t^2}. \tag{2.2.9}$$

With rs as a single variable, it can be shown that $rs(r,t) = Ae^{j(wt-kr)}$ is a solution to Eq. (2.2.9), which can be rewritten as

$$s(r,t)=\frac{A}{r}e^{j(\omega t-kr)}=\frac{A}{r}e^{j\omega(t-r/c)},\qquad r\neq 0, \tag{2.2.10}$$

where the amplitude of $s(r,t)$ decreases proportionally with the distance from the origin.

In a manner analogous to that of the plane waves, the linearity of the wave equation allows for the signal $s(r,t)$ to exhibit any form through being expressed as an infinite superposition of exponential solutions, by using the Fourier transform, and allows for multiple propagating signals coexisting in space with additive superpositions.

$$s(r,t)=\frac{1}{2\pi r}\int_{-\infty}^{\infty}S(\omega)e^{j\omega(t-r/c)}d\omega \tag{2.2.11}$$

Near field

The term "near field" defines the space where waves propagate relatively close to the source. Spherical waves are used to model waves in the near field because the curvature of the wavefronts is not negligible, and becomes more affected by the exact location of the source of propagation.

Despite the fact that spherical wave solutions were obtained using spherical coordinates, Cartesian coordinates will be used throughout this work to represent signals in the near field. As one of the principal aims of this work is to create acoustic images of a terrain, it is convenient to separate the space into a grid, facilitating the use of Cartesian coordinates for analysis.

2.3 Terminology of seismic waves

Seismic waves are elastic waves that originate from a seismic source, such an explosion, earthquake or vibrating seismic truck, and propagate through the Earth up to a range of 120 Hz [10]. The waves of this type are relevant to this thesis as measurements from these waves are used for implementing array processing algorithms, and their basic terminology is employed throughout this document.

Modes of propagation

Depending on the propagation environment, seismic waves are classified into body waves and surface waves. Each type, in turn, is classified based on the mode of propagation, that is, how particles oscillate in the elastic medium for the wave to propagate.

Body waves

Waves propagating through the **internal volume** of an elastic solid are called body waves, and can be sub-categorised depending on whether the particles of the elastic medium oscillate longitudinally (in the same direction of propagation), or transversely (perpendicular to the direction of propagation). The former receive the name **compressional**, longitudinal, primary or **P-waves**, while the latter are called **shear**, transverse, secondary or **S-waves** (see Fig. 2.3a). P-waves always propagate faster than S-waves, typically twice as fast, hence the name *primary* and *secondary*.

Body waves are usually non-dispersive within the seismic range of frequencies (up to 120Hz), meaning that their speed of propagation is independent of frequency [9, 10].

Surface waves

Waves propagating **along or near the surface or boundary** of an elastic solid are called surface waves, and are also sub-categorised depending on the mode of propagation in Love waves and Rayleigh waves. **Love waves** are like S-waves that generate when the surface layer shear speed is lower than the underlying layer, and oscillate perpendicular to the direction of propagation. The associated particle motion of **Rayleigh waves** is elliptical in a plane perpendicular to the surface and rotates backwards (see Fig. 2.3b).

Contrary to body waves, surface waves are dispersive, implying that their speed of propagation is affected by frequency, which make waveforms with a wide range of frequencies change as they propagate [9, 10].

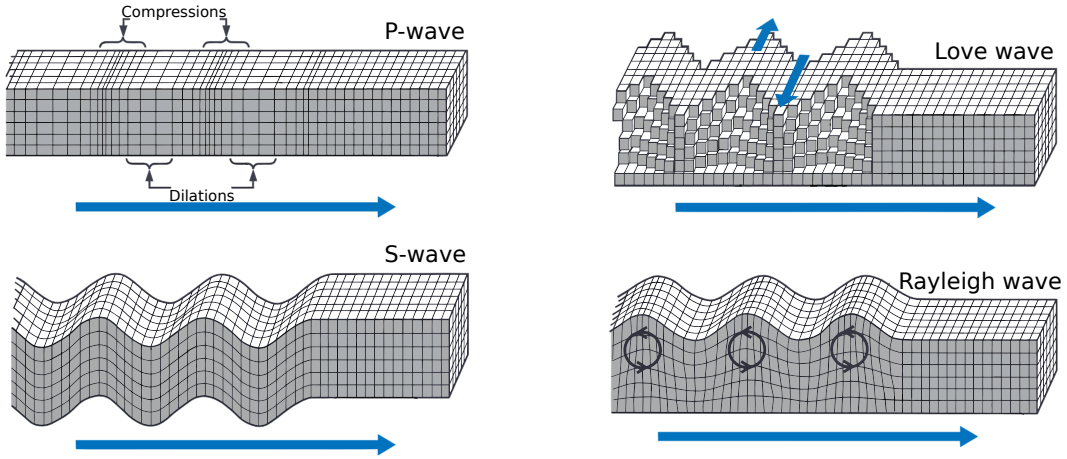

(a) Body waves. **(b)** Surface waves.

Fig. 2.3: Classification of seismic waves. Adapted from [17, 18].

Acoustic impedance

In seismic contexts, acoustic impedance Z is defined as the product of the rock density ρ and the compression propagation speed c_p, as shown in Eq. (2.3.1). This quantity is used for the modelling of reflection and transmission of waves that impinge perpendicularly on the interface of two media [10].

$$Z = \rho c_p \tag{2.3.1}$$

2.4 Properties of wave propagation in non-ideal media

So far, an *ideal* lossless and homogeneous medium was assumed when deriving the equations for plane and spherical waves from the wave equation. In reality, propagating media are more likely to be non-homogeneous, lossy, and may present non-linearities, which make propagating waves behave differently depending on the frequency and amplitude [6]. When the propagation medium is well known, it is useful to consider the properties of wave propagation that deviate from the ideal solutions for plane and spherical waves.

Attenuation

The $1/r$ factor obtained for the spherical solution (Eq. (2.2.10)) is intrinsically related to the geometry of the solution and how the energy must be kept constant between spherical fronts, which causes it to decay by a factor $1/r^2$ proportional to the increase in the area of the spheres, and so the amplitude decays by a factor $1/r$. This type of attenuation is known as ***geometric spreading*** [9] or ***geometric divergence*** [10].

Consider the following wave equation with an added damping term γ:

$$\nabla^2 s = \frac{1}{c^2}\frac{\partial^2 s}{\partial t^2} + \gamma \frac{\partial s}{\partial t}, \quad \gamma > 0 \tag{2.4.1}$$

It is demonstrable that a solution to this wave equation that incorporates a complex vector $\vec{k}$ with a non-zero imaginary component yields an exponential function with a real argument, thereby causing the wave to decay exponentially as it propagates. For instance, a plane wave solution with exponential decay would be as follows [6].

$$s(\vec{x}, t) = A e^{\vec{k}_{\mathrm{Im}} \cdot \vec{x}} e^{j\left(\omega t - \vec{k}_{\mathrm{Re}} \cdot \vec{x}\right)} \tag{2.4.2}$$

In the case of elastic waves, energy is gradually ***absorbed*** into the medium due to frictional losses when the medium is not perfectly elastic, and it is dissipated as heat. The amount of energy lost is proportional to the total available energy of the wave at any given moment, which leads to the exponential decay represented in Eq. (2.4.2). Elastic media, in general, present higher absorption at higher frequencies, which makes them behave like a low-pass filter [9].

Another type of attenuation, known as ***transmission losses*** [10], is caused by other properties of wave propagation, such as reflection, refraction, diffraction, and *mode conversion* [19]. Here, the energy is not lost, but its direction of propagation or *mode* of propagation is changed or forked. The mode of propagation is related to whether the direction of strain points parallel or perpendicular to the direction of propagation.

Dispersion

When signals propagate, they undergo not only attenuation but also temporal spreading, resulting in changes to their original waveform. If the propagation speed of the medium depends on frequency, a signal with a wide range of frequencies in its spectrum will experience changes in its shape during propagation. Fortunately, for this thesis, where seismic vibrations are analysed, dispersion is not a dominant feature in the seismic frequency range, which encompasses frequencies up to 120 Hz [10, 19].

Refraction

A medium that is non-homogeneous has properties that vary throughout space, resulting in changes in the speed and direction of wave propagation. At the interface between two regions of the medium with different propagation speeds, the direction of propagation changes when wavefronts impinge obliquely on it, causing the wavefronts to bend. This is known as *refraction*. This bending of the direction of propagation is usually modelled by Snell's law (2.4.3), where the angle of the refracted wave is a function of the angle of incidence and the propagation speeds of each medium.

$$\frac{\sin\theta_1}{c_1} = \frac{\sin\theta_2}{c_2} \tag{2.4.3}$$

Angles θ_1 and θ_2 are represented in Fig. 2.4a, where Eq. (2.4.3) holds true for waves of the same *mode* of propagation. In this seismic example, an incident P-wave has some of its compressional energy converted to reflected and refracted S-waves. This accounts for a type of transmission loss due to mode conversion, as discussed in the attenuation section. The angles of refraction and reflection of S-waves can be determined using the Zoeppritz equations [20], whose derivations are well explained in [19]. However, this is beyond the scope of this section.

On examining Eq. (2.4.3), one can notice the existence of a critical angle for which the refracted angle θ_2 is equal to 90º. This critical angle is given by

$$\frac{\sin\theta_c}{c_1} = \frac{\sin\frac{\pi}{2}}{c_2} \quad \Longrightarrow \quad \theta_c = \sin^{-1}\left(\frac{c_1}{c_2}\right). \tag{2.4.4}$$

When waves propagate in the same mode, if the angle of incidence exceeds θ_c, then all of the energy is reflected and none of it is refracted to the next medium. This is referred to as "total internal reflection" [9]. It should be emphasised that total internal reflection occurs only between waves of the same mode, as mode conversion causes transmission losses at the interface and generates reflected and refracted waves at other angles.

For seismic waves propagating through the earth, an important phenomenon occurs when waves impinge at the critical angle θ_c: the refracted wave of the same mode as the incident wave propagates along the interface boundary between both media at the medium with the higher propagation speed. The interface boundary wave induces a disturbance on the upper layer, generating waves that propagate away from the interface between the two media. These waves, referred to as *head waves*, persist until the interface wave completely attenuates (see Fig. 2.4b) [9, 10].

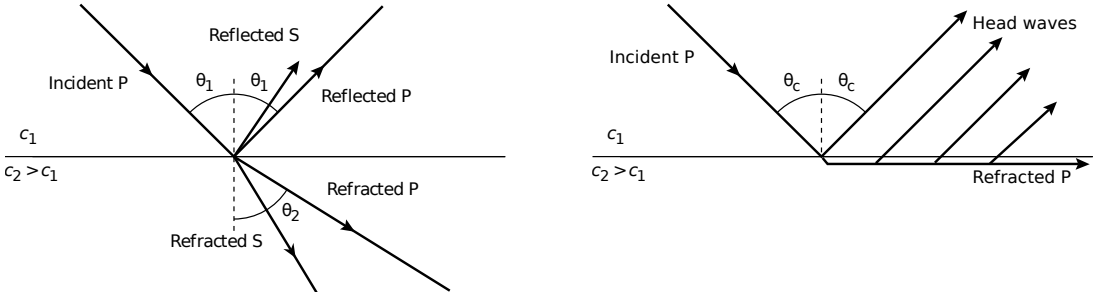

(a) Reflection and refraction. **(b)** Head waves.

Fig. 2.4: Refraction, reflection and head waves. Adapted from [9, 10].

Reflection and transmission

As already introduced in the previous section, wave reflection occurs at the interface of media with different propagation speeds. For oblique incident waves, Snell's law states that the angle of reflection with respect to the normal of the interface is equal to the angle of incidence, as the medium is the same. Also, mode conversion occurs, for which part of the reflected energy is converted to other modes of propagation at different angles, as shown in Fig. 2.5a as an example with an incident P-wave.

Reflection also occurs when the incidence is perpendicular to the interface. A model that is derived from the solutions of Zoeppritz equations [20], which is analogous to the reflectivity on a transmission line, is used to quantify the amplitudes of incident and transmitted waves. This model is based on acoustic impedances of the different media in the earth. The reflection coefficient Γ is defined as the ratio of the reflected wave amplitude A_r over the incident wave amplitude A_i. The transmission coefficient is defined as $\tau = 1 - \Gamma$, and Z_1, Z_2 are the acoustic impedances of each medium (see Fig. 2.5a).

$$\Gamma = \frac{A_r}{A_i} = \frac{\rho_2 c_2 - \rho_1 c_1}{\rho_2 c_2 + \rho_1 c_1} = \frac{Z_2 - Z_1}{Z_2 + Z_1}; \qquad \tau = \frac{A_t}{A_i} = 1 - \Gamma = \frac{2Z_1}{Z_2 + Z_1} \tag{2.4.5}$$

Diffraction

When waves with wavelengths comparable to the structures they encounter, they undergo diffraction, which causes the direction of propagation to change to a radial scattering. In the case of seismic waves, the edges of faulted layers (as shown in Fig. 2.5b) and small isolated objects like boulders within an otherwise homogeneous layer are common sources of diffraction [9, 6].

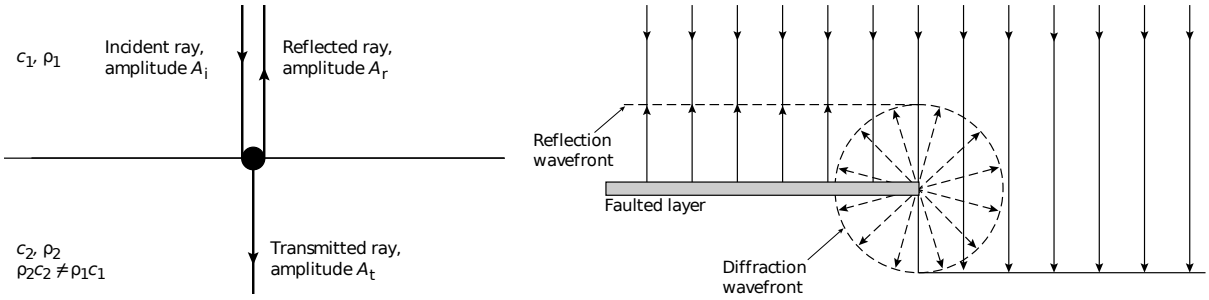

(a) Reflection and transmission. **(b)** Diffraction.

Fig. 2.5: Reflection and diffraction. Adapted from [9].

The aforementioned properties of waves in non-homogeneous media can result in complex and unpredictable wave behaviour, particularly when the characteristics of the environment are unknown. Due to refraction, waves are unlikely to travel in a straight line and will generate reflections on interfaces, as well as diffraction due to their interaction with structures comparable in size to the wavelength. These can be interpreted as new sources of emission. All these properties can be exploited by non-invasive surveying methods.

Chapter 3

ARRAY PROCESSING

Array processing refers to the area of signal processing with useful applications in radar, sonar, geophysics, among others, in which spatial properties of wave propagation are considered by using more than one sensor at separate spatial points [6]. An *array* in this context corresponds to a group of sensors located at distinct locations throughout a determined space. These arrays are usually designed with sensors located equidistantly and taking into consideration the frequency range of the signals to be measured, but any geometry of arrays can be used for array processing.

An intuitive understanding of array processing comes when thinking of the human auditory system (or any animal with a pair of ears for that matter). By having two ears, one is capable of estimating with fair precision from which direction an acoustic wave is coming. This can be done by considering factors such as the *time difference of arrival* of signals at each ear, as well as the frequency-dependent directivity that each ear has due to its physical structure [21].

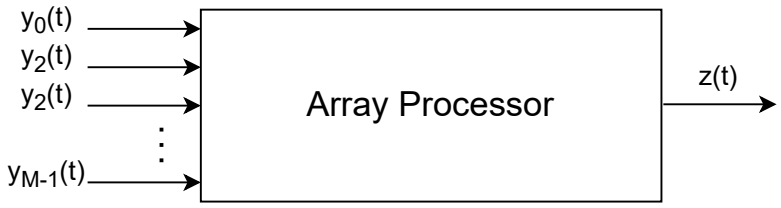

Fig. 3.1: An array processor takes the measurements from each of the M sensors of the array and combines them to generate an output. Adapted from [6].

Two main questions may arise once analysing a set of measurements captured by an array of sensors: **what** is being measured, and **where** is it coming from. An array processor (Fig. 3.1) is then a system that combines the measurements at each input to generate an output in an effort to answer both of these questions, so as to [6]

- **enhance** the signal-to-noise ratio beyond that of a single sensor's output, reduce echoes and reverberations.
- **characterise** the field of waveforms being measured by estimating the *directions of arrival*, in case of planar waves coming from a far-field location; *points of emission*, in case of spherical waves coming from a near-field location; and *number* of sources, in case of being a countable, finite number of sources.
- **track** the source locations as they move in space.

Enhancement

The sole fact of using more than one sensor to measure propagating waves in space can help reduce noise (increase signal-to-noise ratio), assuming a simple model in which the measurement at each sensor $y_m(t)$ consists of a signal $s(t)$, which is identical across all sensors, and spatio-temporally uncorrelated zero-mean noise $v_m(t)$. This could be the case for a plane wave impinging perpendicularly on a linear array of sensors (i.e., all sensors located on the same spatial line).

$$y_m(t) = s(t) + v_m(t) \tag{3.0.1}$$

If we consider an array processor in which the output $z(t)$ is obtained by simply averaging the inputs $y_m(t)$, the signal tends to reinforce while the noise tends to cancel. This is because, by computing the average, we are essentially estimating the noiseless signal $s(t)$ by assuming zero-mean additive noise $v_m(t)$, as represented by Eq. (3.0.2).

$$z(t) = \frac{1}{M}\sum_{m=0}^{M-1} y_m(t) = s(t) + \frac{1}{M}\sum_{m=0}^{M-1} v_m(t) \tag{3.0.2}$$

An array processor can work as a *spatial filter* or *beamformer*. This is analogous to temporal filtering, but instead of filtering by frequency bands, signals impinging on the array in a narrow cone of directions are let pass, while those impinging from other directions are attenuated. This concept, which is explained further in the next section, allows for signal enhancement by reducing echoes and reverberations [22], which are generally assumed to impinge on the array from other directions.

Characterisation

The most important aspect of this work is the characterisation of the locations of the acoustic emission sources in the near field by means of spatial filtering or beamforming. This allows for an acoustic image to be generated by examining the average power of each source at each point in space, and it is referred to as *imaging*.

Let us consider the following generalisation of the model proposed in Eq. (3.0.1) [23]:

$$\begin{bmatrix} y_0(t) \\ y_1(t) \\ \vdots \\ y_{M-1}(t) \end{bmatrix} = \begin{bmatrix} & & & \\ \boldsymbol{a}(\theta_0) & \boldsymbol{a}(\theta_1) & \cdots & \boldsymbol{a}(\theta_{D-1}) \\ & & & \end{bmatrix} \begin{bmatrix} s_0(t) \\ s_1(t) \\ \vdots \\ s_{D-1}(t) \end{bmatrix} + \begin{bmatrix} v_0(t) \\ v_1(t) \\ \vdots \\ v_{M-1}(t) \end{bmatrix} \tag{3.0.3}$$

Vectors $\boldsymbol{a}(\theta_i)$ are called *steering vectors* or *directional mode vectors* and depend on the geometry of the array, the properties of the sensors, the location of the sources, and the properties of wave propagation in space. These vectors basically summarise the changes that signals undergo as they propagate in space until they reach the sensors, assuming that an accurate model of the environment is known, for instance, by introducing time delays and amplitude attenuations.

This model assumes that the measurements at the M sensors are composed of a finite number of emission sources D, transformed accordingly by each steering vector, plus spatio-temporally uncorrelated zero-mean noise $v_m(t)$. The variables θ can represent both directions of arrival in the far-field case and emission locations in the near-field case. Intuitively, one can think of retrieving each signal $s_d(t)$ by means of *inverting* the steering matrix and multiplying it by the sensor measurements $y_m(t)$, which corresponds to the basis of the fundamental *delay-and-sum* beamformer. The steering vectors are then directly related to the passband of directions of arrival of the spatial filter.

Different signal models may be assumed, and its choice depends on the extent of knowledge about the physical properties of the environment [6].

Tracking

By identifying the position of a source at different time instants, combined with a model of the object's dynamics to be tracked and predictive filters such as the Kalman filter, it is possible to track emission sources as they move [24, 25].

Signal and noise assumptions

As introduced in Eq. (3.0.3), we assume that the observations made at each sensor are a linear combination of signals and noise. Here, the zero-mean Gaussian noise is statistically independent of the signals, both temporally and spatially, and is assumed to be *isotropic*, meaning it propagates equally from all directions relative to the array, and has a well-defined power spectrum.

In contrast, the signals are assumed to have a finite, usually countable, range of possible directions of arrival on the array. Note that the signal does not necessarily need to be deterministic, as it can be a temporally uncorrelated but spatially correlated realisation of a stochastic process impinging on the array from a particular direction. Moreover, the signal is not necessarily the primary emission source for a given problem, since inhomogeneities in the medium can induce multiple directions of arrival due to reflections, refractions, and dispersion, as discussed in Section 2.4. Any of these multipaths arriving at the array can be labelled as a signal [6].

3.1 Array properties

The quality of the measurements captured by an array significantly depends on its spatial properties. When designing arrays, it is important to consider the specific range of wavenumbers (spatial frequencies) they are intended to measure. This involves determining the suitable spatial extension and separation between sensors while taking factors such as terrain and cost limitations into account. When using a pre-existing array for array processing, it is necessary to consider its spatial properties in order to correctly interpret the results produced by array processing algorithms.

3.1.1 Continuous finite apertures and spatial resolution

In array processing, the aperture refers to the spatial window through which the *world* is observed. This "window" can have one, two, or three dimensions and is analogous to a temporal window used in signal processing to compute, for instance, a short-time Fourier transform. Intuitively, following this analogy, one might assume that a larger window would yield better spectrum resolution. This holds true as well for spatial spectra, where the temporal analogous to frequency is the wavenumber.

An example of a continuous finite aperture can be found in parabolic antennas. With a large parabolic dish, more radiation can be collected and focused coherently onto a central transducer. This increased area of signal collection can help improve the signal-to-noise ratio and provide a more accurate estimation of the direction of propagation for an incoming wavefront. Drawing an analogy with temporal windows, the focusing in a parabolic antenna is akin to temporal integration.

More formally, the *aperture function* $w(\vec{x})$ is defined as the function that, when multiplied with

the spatiotemporal field $f(\vec{x},t)$, yields the sensor's output $z(\vec{x},t)$.

$$z(\vec{x},t) = w(\vec{x})f(\vec{x},t) \tag{3.1.1}$$

It is important to note that this definition is continuous in both time and space. In an array of sensors, the position $\vec{x}$ of each sensor is predetermined by the array's geometry, and the array can be thought of as a single sensor with a *discrete aperture*.

The space-time Fourier transform of $z(\vec{x},t)$ is given by [6]

$$Z(\vec{k},\omega) = \int_{-\infty}^{\infty} W(\vec{k}-\vec{l})F(\vec{l},\omega)d\vec{l} = (W * F)(\vec{k},\omega) \tag{3.1.2}$$

where $Z(\vec{k},\omega)$ is a **convolution** over wavenumber $\vec{k}$ between the Fourier transform of the field $F(\vec{l},\omega)$ and the *aperture smoothing function*

$$W(\vec{k}) = \int_{-\infty}^{\infty} w(\vec{x})e^{-j\vec{k}\cdot\vec{x}}d\vec{x}. \tag{3.1.3}$$

The convolution means that the wavefield's spectrum is *smoothed* by the kernel $W(\vec{k})$ once it is observed through an aperture $w(\vec{x})$.

To better illustrate the effects of the aperture smoothing function, let's consider the simplest case of a linear aperture, which is more directly comparable to a time window since it has only one dimension. For instance, let

$$w(\vec{x}) = w(x,y,z) = \begin{cases} 1, & |x| \leq D/2, \quad y = z = 0 \\ 0, & \text{otherwise} \end{cases} \tag{3.1.4}$$

then, the aperture smoothing function is given by

$$W(\vec{k}) = W(k_x) = D\,\mathrm{sinc}\left(k_x D/2\right). \tag{3.1.5}$$

Notice how, by increasing the length of the aperture D, the corresponding smoothing function decreases in width as per the argument of the sinc function in Eq (3.1.5). Theoretically, if the aperture is infinitely long, then $W(\vec{k}) = \delta(\vec{k})$, and the convolution with the Fourier transform of the field results in just the field itself. In other words, there is no spatial spectrum smoothing. Fig. 3.2 shows a linear aperture of length D with its respective aperture smoothing function $W(\vec{k})$.

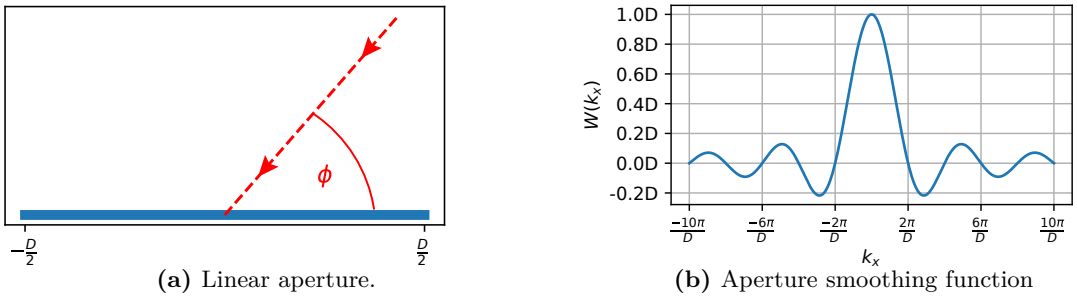

(a) Linear aperture. **(b)** Aperture smoothing function

Fig. 3.2: A linear aperture has an aperture smoothing function with the shape of a sinc function. The longer the aperture, the narrower the peak of $W(k_x)$. Adapted from [6].

Resolution

To understand the meaning of k_x in Fig. 3.2, imagine that if a wavefront impinges perpendicularly on the aperture (i.e. $\phi = \pi/2$), then the field is *constant* along the aperture. This implies a *spatial frequency* of zero. When a wavefront with wavenumber $\vec{k_0}$ arrives at an angle other than $\phi = \pi/2$, it introduces a delay for each value of x in the aperture, given by $e^{-j|\vec{k_0}|x\cos\phi}$. [1] The Fourier transform of a complex exponential is a displacement in the spectrum. For plane waves arriving from different directions, then $F(\vec{k}, \omega)$ consists of several $\delta(\vec{k})$, one for each direction of arrival. The convolution of the aperture smoothing function with each of these deltas of Dirac maps a copy of $W(\vec{k})$ at each position.

The linear aperture example shows that a longer aperture yields a narrower aperture smoothing function. In general, an aperture $w(\vec{x})$ with a large spatial extent has a narrow aperture smoothing function $W(\vec{k})$, which leads to minimal spectral smoothing [6]. When two wavefronts arrive at close angles to each other, a narrower aperture smoothing function is desirable to differentiate both angles of arrival. In this context, resolution is the extent to which two plane waves can be separated. One classical definition of resolution, the Rayleigh criterion [6], states that two incoherent plane waves, propagating in two slightly different directions, are resolved if the main lobe peak of one aperture smoothing function copy falls to zero *before* the value at which the next copy of $W(\vec{k}) =$ reaches its maximum. Following this criterion, Fig. 3.3b and Fig.3.3c display two resolved plane waves, while Fig. 3.3a shows them as unresolved.

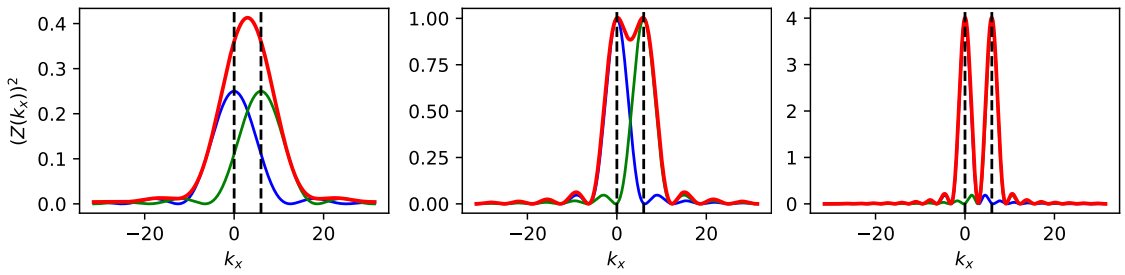

(a) $D = 0.5$m. **(b)** $D = 1$m. **(c)** $D = 2$m.

Fig. 3.3: The resolution increases as the aperture size increases. In this example, two plane waves are resolved in the second and third case according to the Rayleigh criterion.

Ambiguities

Due to the symmetries of aperture geometries, wavefronts arriving with the same wavenumber but from different directions can yield the exact same output. Taking the case of a linear aperture, the angle ϕ remains the same for all directions perpendicular to the axis along which the aperture is set. This ambiguity is then confined within a cone around the aperture, known as the *cone of ambiguity* [6]. In three-dimensional space, an aperture spread on a plane also exhibits ambiguities: it cannot distinguish between waves arriving from both sides of the plane. In theory, only apertures spread along all three dimensions have no ambiguities in determining the directions of arrival. The extent of spread on each axis determines the resolution to resolve these ambiguities.

[1] Note that the mapped angle of arrival ϕ depends on the wavenumber of the impinging wavefront $\vec{k_0}$.

3.1.2 Spatial sampling and aliasing

Apertures have been defined for a continuum of points in space, and the concept can serve as a generalisation of discrete arrays of omnidirectional sensors. When discrete spatial sampling is considered for apertures, it is expected that certain requirements have to be met to avoid *aliasing*, following the analogies from temporal sampling in digital signal processing theory [26, 27].

For an infinite continuous linear aperture, let $s_c(x) = z(x, t_0) = f(x, t_0)$, then the Fourier transform and inverse transform are given by [6]:

$$S_c(k) = \int_{-\infty}^{\infty} s_c(x) e^{-jkx} dx \qquad s_c(x) = \frac{1}{2\pi} \int_{-\infty}^{\infty} S_c(k) e^{jkx} dk. \tag{3.1.6}$$

By sampling along the aperture in regular intervals d, the Fourier transform yields a periodic spectrum. Using $\breve{k} = kd$ to denote the spatial frequency or wavenumber for discrete signals, the Fourier transform of a discrete variable m and its inverse can be written as

$$S(\breve{k}) = \sum_{m=-\infty}^{\infty} s(m) e^{-j\breve{k}m} \qquad s(m) = \frac{1}{2\pi} \int_{-\pi}^{\pi} S(\breve{k}) e^{j\breve{k}m} d\breve{k}. \tag{3.1.7}$$

With some manipulation of Eqs. (3.1.6) and (3.1.7), the spectrum of a infinite signal sampled at regular intervals can be written in terms of the continuous spectrum as

$$S(\breve{k}) = \frac{1}{d} \sum_{p=-\infty}^{\infty} S_c\left(\frac{\breve{k} - 2\pi p}{d}\right) = S(kd) = \frac{1}{d} \sum_{p=-\infty}^{\infty} S_c\left(k - \frac{2\pi p}{d}\right). \tag{3.1.8}$$

It can be observed from this equation, that if the continuous signal $s_c(x)$ has frequency components outside the range $|k| \leq \pi/d$, then the copies of the continuous spectrum overlap. This phenomenon

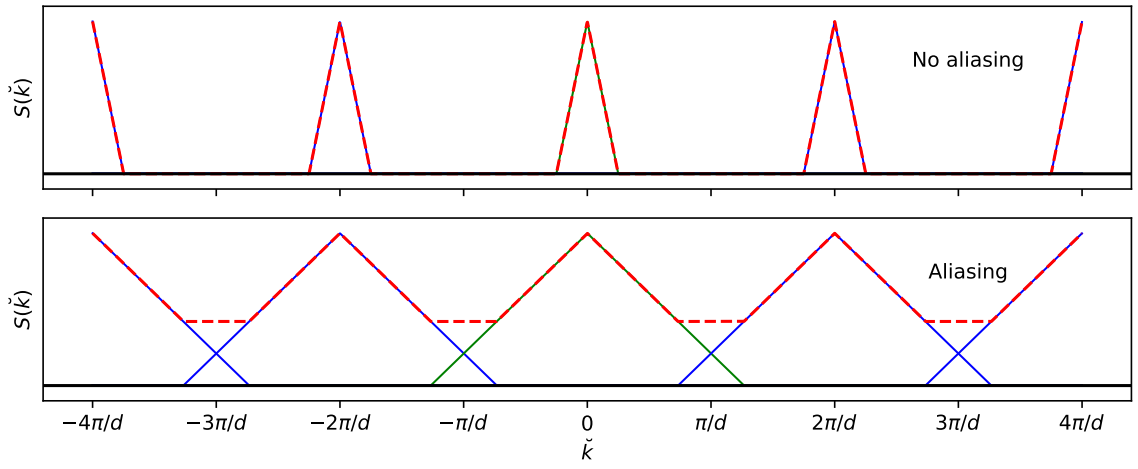

Fig. 3.4: Spatial aliasing occurs in a Uniform Linear Array (ULA) when the continuous signal $s_c(x)$ has spatial frequency components outside $|k| \leq \pi/d$. The copies of the spectrum $S_c(k)$ are overlapped and summed, which can lead to erroneous estimations of directions of arrival. Adapted from [6].

is known as **aliasing**, and is analogous to the results obtained for temporal sampling [26, 27]. This is illustrated in Fig. 3.4 for an arbitrary spatial spectrum.

$$S(kd) = \frac{1}{d} S_c(k) \qquad \text{for } |k| \leq \pi/d \iff d \leq \lambda/2 \tag{3.1.9}$$

This result can be extended to multidimensional signals when sampling is done on regular grids. However, seismic data, which is of interest in this work, is often irregularly or insufficiently sampled [28]. The data used for array processing in this thesis is not sampled in a regular grid due to limitations such as irregularities of the terrain [29], and therefore, a more general treatment is required.

3.1.3 Irregular arrays

The concept of aliasing has been explained with a uniform linear array (ULA), where sampling is done periodically. More generally, consider M sensors that can be placed anywhere in three-dimensional space. The aperture function $w(\vec{x})$ can then be written as a set of M Dirac delta functions, where $\vec{x}_m$ is the position of the m-th vector in the array.

$$w(\vec{x}) = \sum_{m=0}^{M-1} w_m \delta\left(\vec{x} - \vec{x}_m\right) \tag{3.1.10}$$

Following Eq. (3.1.2), the spatial frequency spectrum $Z(\vec{k}, \omega)$ of the array's output is given by the convolution of the Fourier transform of the field and the aperture smoothing function

$$W(\vec{k}) = \sum_{m=0}^{M-1} w_m e^{-j\vec{k}\cdot\vec{x}_m}. \tag{3.1.11}$$

For the uniform linear array, it is assumed that the aperture smoothing function is periodic, because a regular periodic sampling pattern (a Dirac comb function) yields a periodic sequence of impulses in the spectrum. However, non-periodic sensor placement makes the analysis of spatial aliasing not as straightforward as defining a maximum separation between sensors for a given wavenumber. Spatial aliasing effectively occurs when the aperture smoothing function side peaks have amplitudes comparable to that of the main peak, thus approximating the scenario of regular sampling [6]. The next section defines a useful tool for array design when sensors are not placed regularly in a grid.

3.1.4 Correlation sampling and the co-array

Random fields

To first understand one of the main applications of correlation sampling, this section provides an overview of random fields, as well as some statistical definitions. Let $f(\vec{x}, t)$ denote a random field, which is a spatiotemporal stochastic process. For any given $\vec{x} = \vec{x_0}$ and $\vec{t} = \vec{t_0}$, $f(\vec{x_0}, t_0) = f_0$ represents a random variable characterised by a probability density function $p_{f_0}(\cdot)$ [6]. The expected value of this random variable is given by

$$\mathbb{E}[f_0] = \mathbb{E}[f(\vec{x_0}, t_0)] = \int \alpha p_{f_0}(\alpha) d\alpha, \tag{3.1.12}$$

and the correlation function of the random field $f(\vec{x}, t)$ is given by

$$R_f\left(\vec{x}_0, \vec{x}_1, t_0, t_1\right) = \mathbb{E}\left[f_0 f_1\right] = \mathbb{E}[f(\vec{x_0}, t_0) f^*(\vec{x_1}, t_1)] = \iint \alpha\beta p_{f_0 . f_1}(\alpha, \beta) d\alpha d\beta. \tag{3.1.13}$$

Definition 3.1.1. *(Stationary random fields). A random field is stationary when its statistics do not vary with changes of position or time.*

For a stationary random field, the correlation function can be rewritten in terms of the differences $\vec{\chi} = \vec{x_1} - \vec{x_0}$ and $\tau = t_1 - t_0$, which are referred as *lags*, as follows:

$$R_f(\vec{\chi}, \tau) = \mathcal{E}[f(\vec{x_0}, t_0) f(\vec{x_1} + \vec{x_0} - \vec{x_0}, t_1 + t_0 - t_0)] = \mathcal{E}\left[f\left(\vec{x}_0, t_0\right) f\left(\vec{x}_0 + \vec{\chi}, t_0 + \tau\right)\right]. \tag{3.1.14}$$

The power spectral density function $S_f(\vec{k}, \omega)$ of a random field is defined only for stationary processes and is equal to the Fourier transform of the field's correlation function $R_f(\vec{\chi}, \tau)$ [6].

Co-array for continuous apertures

Suppose we want to estimate the correlation function $R_f(\vec{\chi}, \tau)$ of a stationary random wavefield using a continuous finite aperture. As stated in Eq. (3.1.1), the field is observed through the aperture function $w(\vec{x})$.

$$z(\vec{x}, t) = w(\vec{x}) f(\vec{x}, t) \tag{3.1.15}$$

The spatiotemporal correlation function of $z(\vec{x}, t)$ is equal to

$$\begin{aligned} R_z\left(\vec{x}_1, \vec{x}_2; \tau\right) &= \mathbb{E}\left[z\left(\vec{x}_1, t\right) z^*\left(\vec{x}_2, t + \tau\right)\right] \\ &= \mathbb{E}\left[w(\vec{x_1}) f(\vec{x_1}, t) f^*(\vec{x_2}, t + \tau) w^*(\vec{x_1} + \vec{\chi})\right] \\ &= w\left(\vec{x}_1\right) w^*\left(\vec{x}_1 + \vec{\chi}\right) \mathbb{E}\left[f(\vec{x_1}, t) f^*(\vec{x_1} + \vec{\chi}, t + \tau)\right] \\ &= w\left(\vec{x}_1\right) w^*\left(\vec{x}_1 + \vec{\chi}\right) R_f(\vec{\chi}, \tau). \end{aligned} \tag{3.1.16}$$

Since $R_z\left(\vec{x}_1, \vec{x}_2; \tau\right)$ is not only a function of $\vec{\chi} = \vec{x_2} - \vec{x_1}$ spatially, $z(\vec{x}, t)$ is not stationary in space. This becomes evident when we consider $w(\vec{x})$ as a finite window, as the statistics vary with changes in position outside the window. However, we can integrate $R_z\left(\vec{x}_1, \vec{x}_2; \tau\right)$ over the aperture with respect to $\vec{x_1}$ to obtain a stationary estimate of the field's correlation function:

$$\begin{aligned} \hat{R}_f(\vec{\chi}, \tau) = \int_A R_z\left(\vec{x}_1, \vec{x}_1 + \vec{\chi}; \tau\right) d\vec{x}_1 &= \int_A w\left(\vec{x}_1\right) w^*\left(\vec{x}_1 + \vec{\chi}\right) R_f(\vec{\chi}, \tau) d\vec{x}_1 \\ &= R_f(\vec{\chi}, \tau) \int_A w\left(\vec{x}_1\right) w^*\left(\vec{x}_1 + \vec{\chi}\right) d\vec{x}_1 \\ &= c(\vec{\chi}) R_f(\vec{\chi}, \tau), \end{aligned} \tag{3.1.17}$$

where the co-array function $c(\vec{\chi})$ is defined as the autocorrelation of the aperture function $w(\vec{x})$

$$c(\vec{\chi}) \triangleq \int_A w\left(\vec{x}\right) w^*\left(\vec{x} + \vec{\chi}\right) d\vec{x}. \tag{3.1.18}$$

The estimate of the field's correlation function, $\hat{R}_f(\vec{\chi}, \tau)$, is essentially the original field's correlation function, $R_f(\vec{\chi}, \tau)$, sampled within the window defined by the co-array. This result implies that the power spectrum estimate, $\hat{S_f}(\vec{k}, \omega)$, is smoothed by the Fourier transform of $c(\vec{\chi})$, which corresponds to the squared magnitude of the aperture smoothing function, $|W(\vec{k})|^2$ [6].

Co-array for discrete apertures

Suppose we now have a discrete aperture described by impulse functions for each sensor in space, as shown in Eq. (3.1.10). By rewriting Eq. (3.1.15) with predefined locations of the mth sensor, we obtain:

$$y_m(t) = w_m f(\vec{x_m}, t). \tag{3.1.19}$$

The correlation between the measurements obtained by two sensors m_1 and m_2, assuming a spatially and temporally stationary wavefield, is:

$$\begin{aligned} R_y^{m_1 m_2}(\tau) &= \mathbb{E}\left[y_{m_1}(t) y_{m_2}^*(t+\tau)\right] \\ &= w_{m_1} w_{m_2}^* \mathbb{E}\left[f(\vec{x}_{m_1}, t) f^*(\vec{x}_{m_2}, t+\tau)\right] \\ &= w_{m_1} w_{m_2}^* R_f(\vec{x}_{m_1}, t) f^*(\vec{x}_{m_2}, \tau) \\ &= w_{m_1} w_{m_2}^* R_f(\vec{\chi}, \tau). \end{aligned} \tag{3.1.20}$$

Analogously to the case of the continuous aperture, an estimate of the field's correlation function can be obtained by integrating (or in this case, summing) the correlations between the measurements across the entire aperture.

$$\begin{aligned} \sum_{(m_1,m_2)\in A} R_y^{m_1 m_2}(\tau) &= \sum_{(m_1,m_2)\in A} \mathbb{E}\left[y_{m_1}(t) y_{m_2}^*(t+\tau)\right] \\ &= R_f(\vec{\chi}, \tau) \sum_{(m_1,m_2)\in A} w_{m_1} w_{m_2}^* \\ &= c(\vec{\chi}) R_f(\vec{\chi}, \tau) \end{aligned} \tag{3.1.21}$$

The discrete co-array function $c(\vec{\chi})$ is defined for the set of indices of sensors (m_1, m_2) in the discrete aperture A where $\vec{x}m_2 - \vec{x}m_1 = \vec{\chi}$. A more formal definition of the set of lag vectors $\vec{\chi}$ for which the co-array is defined is as follows [30]:

$$c_{\vec{\chi}} = \left\{\vec{\chi} \mid \vec{\chi} = \vec{x}_{m_2} - \vec{x}_{m_1}, \text{ for } \vec{x}_{m_1}, \vec{x}_{m_2} \in A\right\}, \tag{3.1.22}$$

where A represents the set of points that constitute the aperture. The operation described in Eq. (3.1.22) is also referred to as the "morphological auto-correlation" of A or the *dilation* of the set A by itself in the context of mathematical morphology [31].

This co-array set is commonly known as the *difference co-array* to distinguish it from its counterpart, the *sum co-array*, which is defined for the sum of positions of sensors instead of the difference. The sum co-array is also referred to as the *morphological auto-convolution* of A. The difference co-array comprises all *vector spacings* between points in the aperture and possesses the property of being symmetric with respect to the origin. Additionally, it is not sensitive to the definition of the origin in the aperture [30].

The discrete co-array function $c(\vec{\chi})$ is equal to the inverse Fourier transform of $|W(\vec{k})|^2$, which represents the squared magnitude of the aperture smoothing function, just like in the continuous case. The power spectrum $S_f(\vec{k}, \omega)$ is smoothed by the kernel $|W(\vec{k})|^2$. In the discrete case, it is crucial to ensure that the sample spacing in the co-array domain is small enough to prevent spatial power spectrum aliasing. For regular arrays, the minimum co-array sample spacing is determined by the minimum spacing between sensors in the aperture, which should be at most half the minimum wavelength of the signal to measure, as stated by the spatial Nyquist theorem in Eq. (3.1.9). However, for irregular arrays, spatial aliasing analysis is not as straightforward since the minimum co-array sampling spacing also depends on the specific geometry of the array.

Let us consider the case in which the weights for all sensors are unitary, meaning $w_m = 1\ \forall m \in M$. The co-array of an array can be visualised as shown in Fig. 3.5, where the size of each point in the co-array is proportional to the *redundancy* at each lag $\vec{\chi}$. This redundancy indicates that there are multiple pairs of positions $\vec{x}_{m_1}$ and $\vec{x}_{m_2}$ that result in the same lag $\vec{\chi}$. In fact, $c(\vec{\chi} = 0) = M$ always, as the only pair of positions that yields a zero lag is when $\vec{x}_{m_1} = \vec{x}_{m_2}$. In general, this implies that the maximum number of distinct lags in the co-array is given by $M^2 - M + 1$.

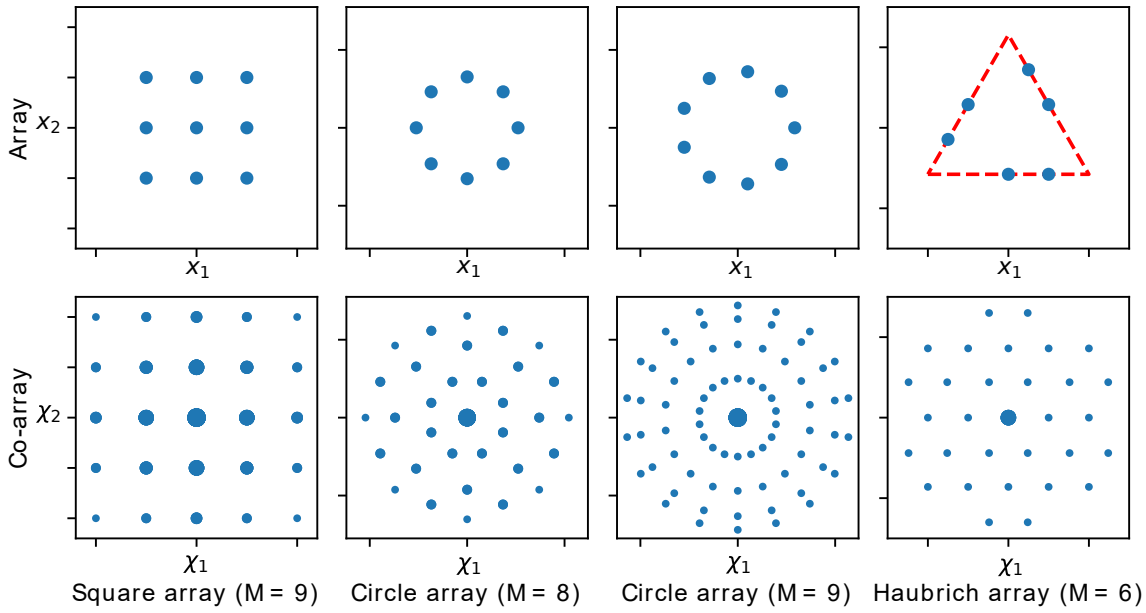

Fig. 3.5: The co-arrays (bottom) of various array configurations (top) are depicted, where x_1, x_2 represent the first two components of the space vector $\vec{x}$, and χ_1, χ_2 represent the first two components of the lag vector $\vec{\chi}$. In the co-array plots, the size of the points corresponds to the redundancies, representing the number of pairs of sensor positions that result in the same lag. The circle array with $M = 9$ sensors and the Haubrich array exhibit no redundancies, except at the origin.

Fig. 3.5 shows various array configurations along with their respective co-arrays in the lag $\vec{\chi}$ domain. It can be observed that for a regular Cartesian square array (on the left), the minimum separation between lags is the same as the minimum distance between sensors, and many lags exhibit redundancy. This redundancy indicates the number of sensor pairs that contribute to spatial averaging at a specific lag $\vec{\chi}$. In contrast, let us consider an array of sensors arranged in a circumference, with all sensors evenly spaced. By increasing the number of sensors from $M = 8$ to $M = 9$ while maintaining a constant separation between sensors (resulting in a slightly larger circumference), the minimum separation between lags in the co-array significantly decreases. Lastly, the so-called Haubrich array is shown as an example where the number of sensors is minimised to achieve a regular co-array sampling, with no redundancies except at the origin. It is this minimum spacing that generally determines the array's spatial aliasing characteristics. A trade-off is thus made between spatial aliasing characteristics and spatial averaging, which can impact the array's robustness to spatial noise [6, 30].

A direct application of the co-array is found in the design of *sparse* arrays, which aim to reduce the total number of sensors, denoted as M, while maintaining a spread sampling in the co-array. By strategically placing sensors in a sparse configuration, the aperture can be expanded, resulting in increased resolution. To design sparse arrays, a common approach involves first considering a non-redundant co-array and then determining an array arrangement that achieves this co-array. Typically, these sparse arrays possess a virtual underlying regular grid, which may not necessarily be Cartesian with mutually perpendicular base vectors. An example of such an array is the Haubrich array [32], which minimises the number of sensors while still yielding a non-redundant co-array for all lags except the origin (see Fig. 3.5).

3.1.5 Summary and implications

This section has provided an overview of considerations to bear in mind when designing an array or interpreting the measurements obtained by a pre-designed array.

It has been demonstrated that, with a linear continuous aperture, the ability to distinguish between slightly different directions of arrival, known as resolution, improves as the aperture extends in space. The use of a continuous aperture has been employed to illustrate this property and highlight that simply adding more sensors to a discrete array may not necessarily enhance resolution if the aperture is not extended in space.

If the spatial extent of the aperture remains constant, the number of sensors typically determines the magnitude of the side-lobes in the aperture smoothing function. This, in turn, determines the array's ability to reject waves propagating from other directions. The specific values of the sensor weights, denoted as w_m, can be designed to *apodise* the aperture smoothing function. This approach is akin to applying a Hann window (or any kind of apodisation window) in digital signal processing to reduce side-lobes in the spectrum.

When utilising measurements from a discrete array, it is crucial to consider aliasing. For regular Cartesian arrays, aliasing can be avoided by ensuring that the distance between sensors is no greater than half the minimum wavelength of the propagating acoustic field. This principle is analogous to the Nyquist theorem for temporal sampling. However, for irregular arrays, aliasing must be analysed in the context of the co-array, as the aliasing characteristics are determined by the minimum spacing between co-array samples. It is worth noting that for regular arrays, this minimum distance in the co-array domain matches that in the array domain.

Particular emphasis has been placed on irregular arrays and their co-arrays, as array processing algorithms are implemented using measurements from Distributed Acoustic Sensing in this thesis. These measurements are obtained from an optical fibre dispersed irregularly across an irregular terrain.

3.2 Spatial filtering and beamforming

At the beginning of this chapter, a general introduction was given on how an array processor can work as a spatial filter by filtering signals impinging on the array from determined directions or locations. Enhancement is achieved by filtering out signals or noise coming from other directions that interfere with the signal of interest. Characterisation of a field is done by scanning the energy coming from all directions relative to the array, thereby estimating the spatial spectrum. This estimation is known as the *array steered response*.

Beamforming is the name given to a wide variety of array processing algorithms that focus the array on a particular direction. The term *beamforming* has its origins in array transmitting rather than receiving energy, as the array *forms* a *beam* of energy in a particular direction. Now the term is used interchangeably for receiving arrays as well, where the beam refers to the main lobe of the directivity pattern in a spatial filter [6]. One of the advantages of using arrays for spatial filtering is that the focusing made by a beamformer in array processing is done via signal processing instead of mechanically, as would be the case with focusing a single directional sensor.

3.2.1 Delay-and-sum beamforming

The simplest beamforming algorithm is known as delay-and-sum. Its main idea is straightforward from its name: to delay the measurements from each sensor by appropriate amounts and add them.

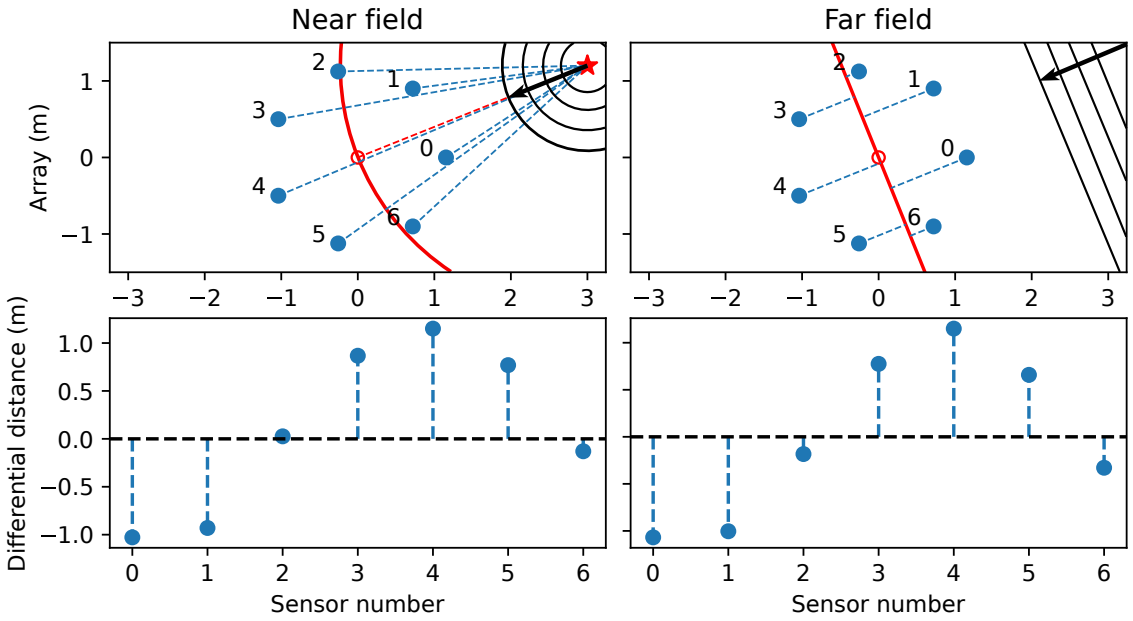

Fig. 3.6: The concept of differential distances relative to an origin point is illustrated for both near and far field scenarios. The delays of wavefronts arrival is proportional to this distance, assuming knowledge of the speed of propagation of the medium. In the near field, it is possible to estimate the absolute position of a source, whereas in the far field, it is only possible to estimate directions of arrival.

The amount of delay applied to each sensor depends on the geometry of the array, the speed of wave propagation in the medium, and whether the focusing point is in the far field or near field. The output $z(t)$ of the delay-and-sum beamformer is obtained by applying a delay Δ_m and an amplitude weight w_m to the output $y_m(t)$ of each sensor, and then summing the resulting signals [6], and can be expressed as:

$$z(t) = \sum_{m=0}^{M-1} w_m y_m(t - \Delta_m) \tag{3.2.1}$$

The amplitude weighting is also referred to as the array's *shading* or *taper*. It can alter the shape of the main lobe and reduce side-lobe levels, similar to the application of a Hamming window or similar techniques in signal processing, as discussed for continuous and discrete apertures. The amplitude weighting can also account for amplitude losses caused by propagation, as explained in Chapter 2.

For near-field focusing, if the speed of propagation of the medium is precisely known and the medium is homogeneous, the delay applied to each sensor output $y_m(t)$ is determined to compensate for the delays at which a spherical wavefront arrives at each sensor. Specifically, Fig. 3.6 illustrates a circular array consisting of $M = 7$ sensors. The arrival delays of the spherical wavefront at each sensor are proportional to the difference between their distance to the focusing point (represented by the red star) and the distance between the focusing point and an arbitrarily chosen origin, which, in this case, is located at the centre of the array (depicted by the red circumference). This differential distance is shown at the bottom left of Fig. 3.6. To align the wavefronts originating from a specific focusing point, the delay added to each sensor must be inversely proportional to this differential distance, scaled by the medium's propagation speed. As a result, the signal propagating from

the focusing point is added constructively, while noise and signals from other locations are added destructively.

In the far-field scenario, focusing is performed towards infinity by assuming plane wavefronts. Since it is not feasible to calculate the distance from each sensor to infinity, it is convenient to define a plane that passes through the arbitrarily chosen origin, with its normal vector pointing in the direction of focusing. The differential distance, which is proportional to the arrival delays at each sensor, can then be determined as the signed distance from each sensor to this plane, as depicted in Fig. 3.6. It should be noted that in the far-field scenario, only the directions of arrival can be estimated. However, in the near-field case, due to the spherical properties of the propagating waves, it is also possible to estimate the range to the source, thereby determining the absolute location in space.

3.2.2 Steered response power

Eq. (3.0.3) introduces a model that represents the measurements obtained at each sensor in an array. This model consists of altering the signals in the spatial field with the so-called steering vectors, along with additive noise. Steering vectors are presented as elements that modify the signals in space through phase shifts and scalings, which depend on the geometry of the array. Due to differences in the distance that the signal must travel to reach each sensor, the time delays introduced by these vectors are calculated by scaling the distance differences with a propagation speed. The scaling reflects the attenuation of the waves over those distances. This attenuation can be attributed to either the spherical nature of the waves or the intrinsic attenuations of the medium.

In this section, it is also anticipated that to estimate the signals $s_d(t)$, an inversion of the effects of the steering vectors can be applied to the measured signals $y_m(t)$ at each sensor. The aim is to reverse the temporal delays and potential attenuations caused by the propagation of the signals in space. However, since the values of θ_d, which represent arrival angles for the far field and points in space for the near field for a specific signal d, are not known beforehand, a scanning across a continuum of θ values has to be made. For each scanned θ, a delay Δ_m and a component of the weight w_m to counteract attenuation losses, if present in the model, are added to each sensor m. Thus, by applying Eq. (3.2.1), a signal $z(t)$ is obtained for each θ. To recover a specific signal $s_d(t)$, the array must be focused at $\theta = \theta_d$.

To determine which directions of arrival or points in space θ contain useful signal information, the steered response power is defined as follows:

$$P_{BF}(\theta) = \int \big(z(t)\big)^2 dt = \int \left(\sum_{m=0}^{M-1} w_m y_m(t - \Delta_m) \right)^2 dt. \tag{3.2.2}$$

Here, the focus is on estimating the energy of each $z(t)$ obtained by focusing the array on each θ. This allows for the estimation of the spatial spectrum in a manner similar to how a spectrum analyser scans a range of temporal frequencies by calculating the energy within a temporal window through integration.

The definition in Eq. (3.2.2) assumes that each sensor captures time continuously, which is not realistic. In practice, to calculate the steered response power using delay-and-sum in the time domain, we use

$$P_{BF}(\theta) = \sum_{k=0}^{K-1} \big(z[k]\big)^2 = \sum_{k=0}^{K-1} \left(\sum_{m=0}^{M-1} w_m y_m[k - \Delta_m] \right)^2. \tag{3.2.3}$$

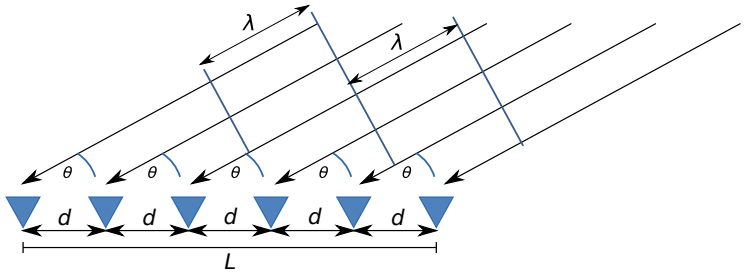

Fig. 3.7: A uniform linear array (ULA) with $M = 6$ sensors, an aperture L, a distance between sensors d, and an impinging wavefront of wavelength λ at an angle θ.

In literature [6, 22, 23], the steered response power is often described for narrow-band signals represented as complex phasors. A delay in a phasor translates into a phase shift, reversible by taking the phasor's conjugate, making the transformation applied by the steering vectors a simple multiplication. For instance, in a uniform linear array (ULA) intended for scanning the far field, illustrated in Fig. 3.7, the steering vectors are defined as

$$\boldsymbol{a}(\theta) = \begin{bmatrix} 1 & e^{-j2\pi \frac{d}{\lambda} \cos\theta} & \dots & e^{-j(M-1)2\pi \frac{d}{\lambda} \cos\theta} \end{bmatrix}^T, \tag{3.2.4}$$

where d is the separation between sensors, λ is the wavelength, and θ is the angle of arrival. The steered response power is then defined as

$$P_{BF}(\theta) = \boldsymbol{a}^H(\theta)\boldsymbol{R_y}\boldsymbol{a}(\theta) = \boldsymbol{a}^H(\theta)\boldsymbol{y}\boldsymbol{y}^H\boldsymbol{a}(\theta) = \left|\left|\boldsymbol{a}^H(\theta)\boldsymbol{y}\right|\right|^2 = \left|\left|\boldsymbol{z}\right|\right|^2 = \sum_{k=0}^{K-1} \left(z[k]\right)^2, \tag{3.2.5}$$

which is equivalent to the general time-domain definition in Eq. (3.2.3). Note that the steering vector $\boldsymbol{a}(\theta)$ cannot always be defined in a straightforward manner. This is why the general method for arbitrary arrays is introduced in Fig. 3.6 to map the differential distances.

Scanning the steered response power enables the estimation of angles of arrival or points in space θ_d by identifying the arguments θ where peaks in $P_{BF}(\theta)$ are detected.

3.2.3 Variations of the steering response power using a ULA

To exemplify the concepts described and connect them to the properties of arrays presented in Section 3.1, delay-and-sum beamforming is applied to a simulated uniform linear array (ULA), with variations in each of its parameters. The simulations are conducted with a single incident signal at a single frequency, unless stated otherwise.

Fig. 3.8 demonstrates how the resolution of the main lobe in the estimation of the spatial spectrum through the steered response power increases as the length of the ULA increases. In all cases, the condition $d \leq \lambda/2$ of the spatial Nyquist theorem is met, ensuring no aliasing. By keeping the aperture L and propagation speed constant, Fig. 3.8 can also illustrate the variation in the width of the main lobe as the frequency of the propagated signal changes. With a fixed aperture and a higher frequency, a higher resolution for resolving incident wave fronts is achieved.

Now, if the aperture L is kept constant, and the number of sensors M varies while maintaining a uniform distribution of the sensors within the ULA, the effect on the steered response is observed in the level of the side lobes. As more sensors are used, the level of the side lobes decreases. This is

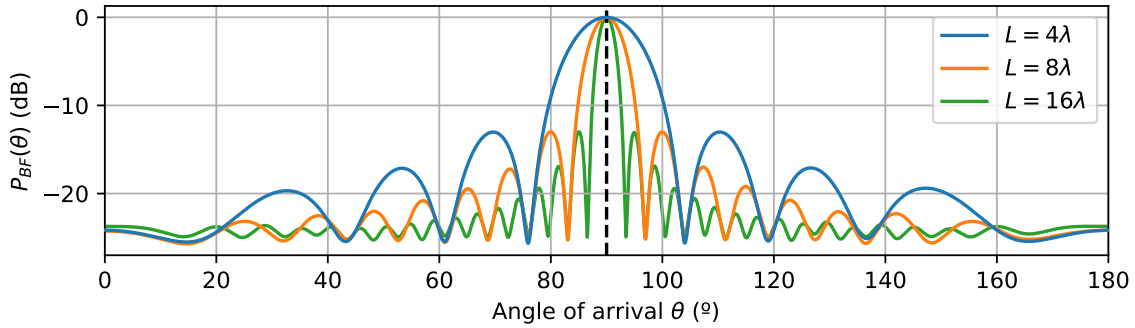

Fig. 3.8: ULA simulation: number of sensors M constant with a variable aperture (length L). Main lobe width decreases as length increases.

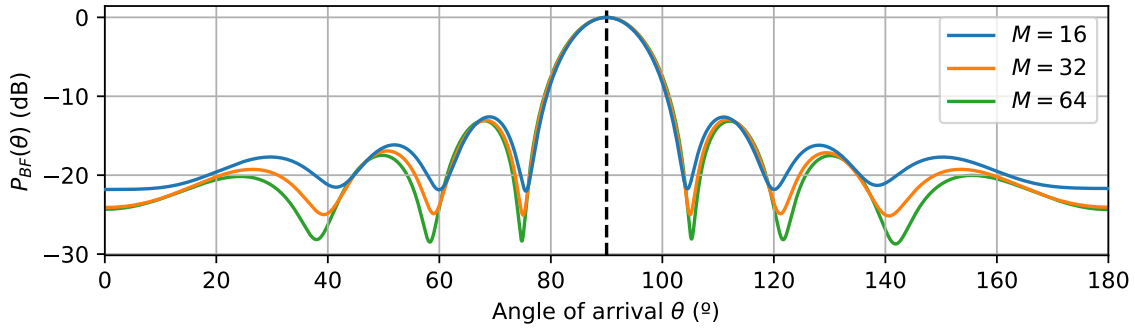

Fig. 3.9: ULA simulation: number of sensors M variable with a constant aperture (length L). Side-lobe levels decrease as the number of sensors M increases.

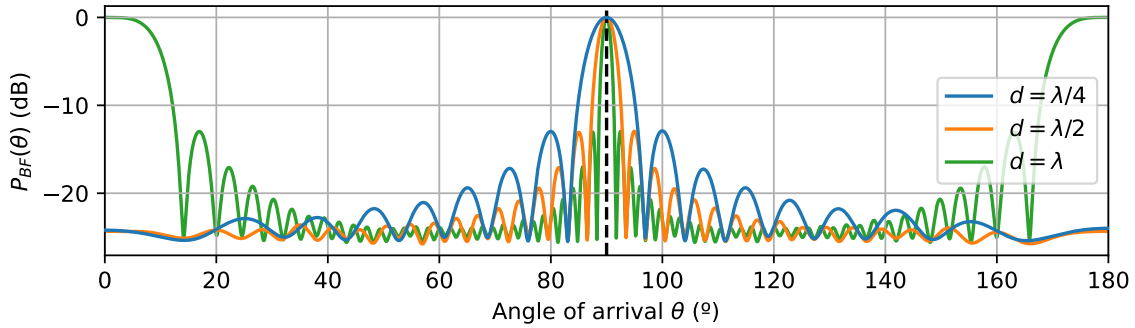

Fig. 3.10: ULA simulation: Increasing the distance d between sensors in a uniform array over the Nyquist limit $\lambda/2$ generates spatial aliasing in the estimated spatial spectrum. The number of sensors M is kept constant, while the length L varies as d changes.

illustrated in Fig. 3.9. Note that the resolution is not affected by increasing the number of sensors, thus corroborating the theory of continuous apertures presented in Section 3.1.1.

The impact of varying the aperture L is depicted in Fig. 3.8, with sensor separation of $d \leq \lambda/2$.

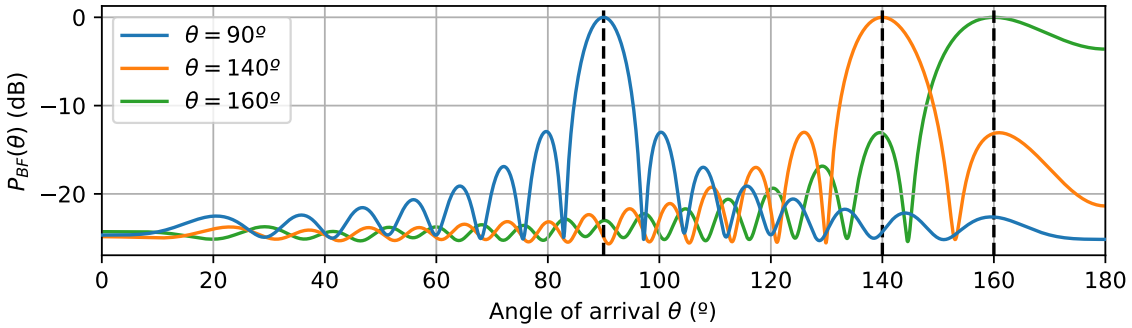

Fig. 3.11: ULA simulation: Resolution on θ decreases for angles where $|\cos\theta| \rightarrow 1$.

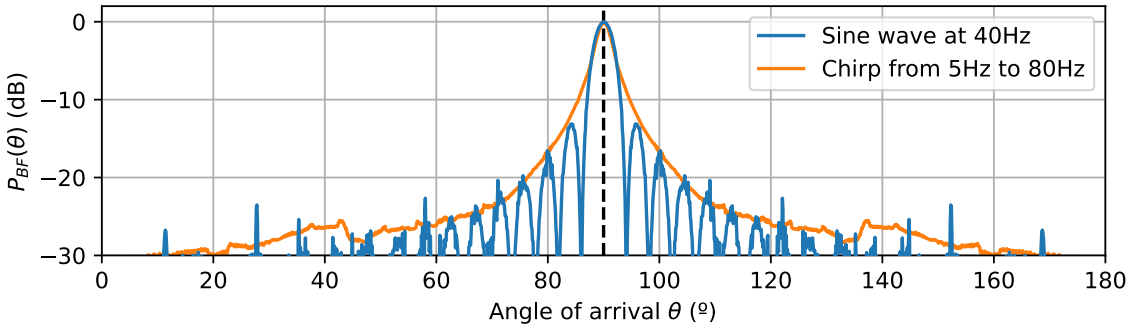

Fig. 3.12: ULA simulation: Comparison of the effects of narrow-band and wide-band signals on the steered response.

Continuing to increase the aperture while keeping the number of sensors M constant and uniformly distributed enhances the resolution of the main lobe. However, surpassing the Nyquist limit leads to spatial aliasing, as described in Section 3.1.2, which creates ambiguities in estimating the direction of propagation of a source. This is illustrated in Fig. 3.10 for a ULA. By keeping the number of sensors M constant and increasing the aperture L while maintaining a uniform separation between sensors d, when the aperture exceeds the Nyquist limit, a new direction of arrival is estimated at $\theta = 0°$, even though no wavefront is actually impinging from this angle. It is important to note that the ambiguity resulting from spatial aliasing differs from the intrinsic ambiguity due to the spatial extension of an array. While a ULA can estimate a one-dimensional angle of arrival for sources in the far-field, it cannot distinguish among the multiple potential sources within the cone of possibilities around it.

In the figures presented in this section, the angle of arrival θ is plotted on the horizontal axis, instead of the wavenumber k_x as in Section 3.1. There, it is explained that for linear apertures, a mapping from the wavenumber $\vec{k}$ to the delay introduced at each point x of the linear aperture is given by $e^{-j|\vec{k}|x\cos\theta}$. This mapping is discretised in Eq. (3.2.4) for a ULA. The mapping is proportional to $\cos\theta$, intuitively meaning that near angles where $|\cos\theta|$ is close to one, the resolution in θ decreases. This is because the same variation in θ results in a much smaller difference in delays due to the intrinsic shape of the cosine curve, whereas at angles close to 90°, the mapping tends to be linear. Fig. 3.11 illustrates this decrease in resolution as the angle of arrival θ approaches 0° or 180°. Note

that the angle θ is measured from the ULA in the same way that ϕ is defined in Fig. 3.2a for a linear continuous aperture. Thus, $\theta = 90°$ means that the planar wavefront impinges upon the array in such a way as to reach each sensor at the same instant.

Finally, Fig. 3.12 presents an example of applying time-domain delay-and-sum to obtain the steered response when a wide-band signal is measured. This example compares a sine wave at 40Hz (narrow-band signal) with a chirp spanning frequencies from 5Hz to 80Hz (wide-band signal) over 20 seconds. In the case of the chirped signal, the spectrum no longer exhibits periodic zeros, and its steered response serves as an approximate envelope to that of the sine wave, with a frequency equivalent to the approximate central frequency of the chirp. For this comparison, the power levels of both signals were adjusted to make the plots comparable, with a maximum power of 0dB.

3.2.4 Acoustic imaging

Acoustic imaging refers to the formation and processing of images generated from raw signals acquired by a set of acoustic transducers [33]. Similar to traditional optical imaging, a scene is *illuminated* by the emission of an acoustic signal, and with an array of sensors, the reflected signals' energy from each spatial location can be measured by focusing an array of acoustic sensors at it.

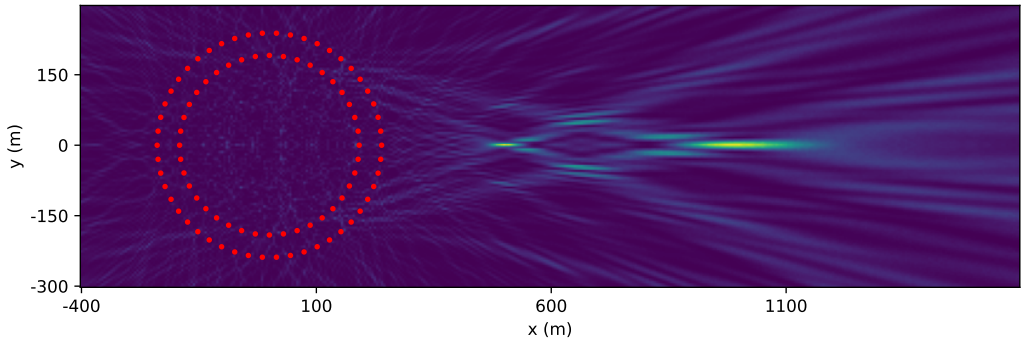

(a) Narrow-band sources at 40Hz

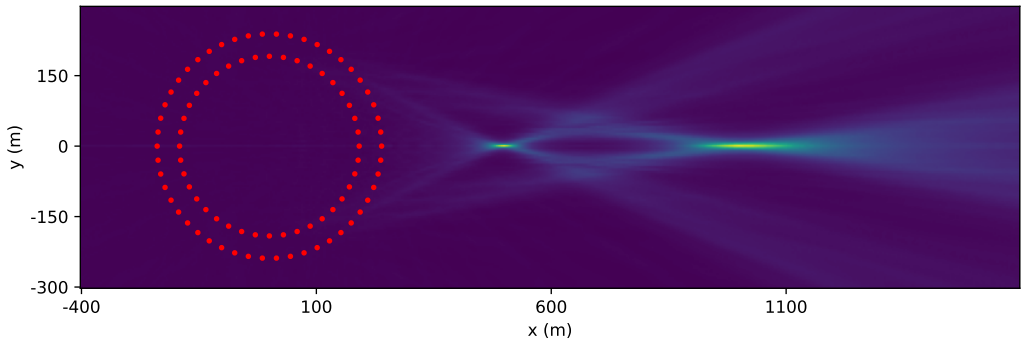

(b) Wide-band chirp, 5-80Hz, over a 20-second window

Fig. 3.13: Comparison of range resolution in near-field imaging with narrow-band and wide-band omnidirectional sources, both located at $(x, y) = (500, 0)$ and $(x, y) = (1000, 0)$, with a constant propagation speed of 336m/s. The steered response power P_{BF} is plotted as a function of the coordinates (x, y) on a linear scale, where yellow indicates the highest P_{BF} measured.

As already pointed out with the ULA examples, in order to obtain a high-resolution image, the aperture of the array of sensors should be sufficiently large in comparison to the wavelengths of the signals of interest. It is important not to confuse the actual obtainable resolution given by the aperture of the array with the sampling grid used to focus the array at each position θ. For near-field imaging, range resolution [6, 33] decreases as the focusing is done further away from the centroid of the array. This is due to, as approaching the far field, wavefronts originating from there approximate plane waves when impinging on the array.

For the circular array depicted with red dots in Fig. 3.13, two simulated omnidirectional sources are placed at $(x, y) = (500, 0)$ and $(x, y) = (1000, 0)$, with a constant propagation speed of 336m/s. The steered response power P_{BF} is plotted as a function of the coordinates (x, y) on a linear scale, where yellow indicates the highest P_{BF} measured. The loss in range resolution can be observed for both narrow-band sources at 40Hz and chirped sources ranging from 5Hz to 80Hz within a 20-second window. Note how, in a manner similar to that shown in Fig. 3.12, periodic side lobes are no longer present with wide-band signals in Fig. 3.13b, using the same number of sensors M, whereas side lobes are observed in Fig. 3.13a.

For far-field imaging, since the range cannot be resolved because the wavefronts impinging on the array are effectively plane waves, an additional axis becomes available for plotting the image. This extra axis, which is the radial axis in a polar plot, can be used, for example, to map an elevation angle in addition to the azimuth angle, thereby providing a three-dimensional estimation of the directions of arrival of the impinging waves. To achieve this, an array that is spread out in a two-dimensional plane is necessary [33]. Alternatively, the additional axis could be used to plot a grid of propagation speeds, enabling their estimation when they are not known beforehand by selecting the propagation speeds where the highest steered response power is estimated [2].

For instance, Fig. 3.14 displays a simulation of narrow-band far-field sources at 10Hz with different speeds of propagation in the radial axis and angles of arrival in the angular axis, using the same circular array as in the near-field imaging example shown in Fig. 3.13. Three sources at 0º, 40º

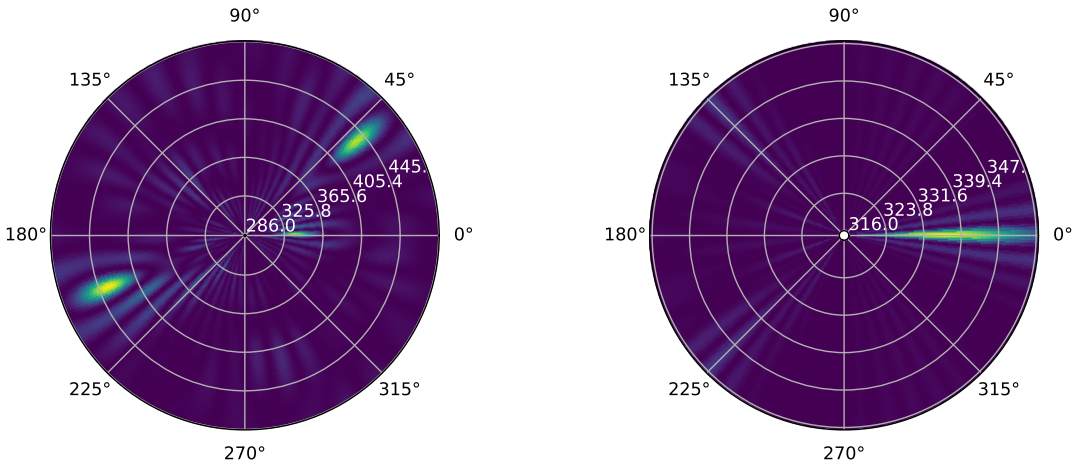

(a) Sources at 0º, 40º and 200º, with propagation speeds of 336m/s, 446m/s and 446m/s respectively

(b) Source at 0º with a propagation speed of 336m/s. Zoomed version of 3.14a

Fig. 3.14: Far-field imaging example using a circular array of sensors, measuring signals at distinct directions of arrival and with different propagation speeds.

and 200º, with propagation speeds of 336m/s, 446m/s and 446m/s respectively, are simulated and can be successfully estimated in Fig. 3.14a as sections of the plot with high steered response power. Fig. 3.14b presents a zoomed-in version focusing on speeds of propagation around 336m/s showing that there is not just one but a range of propagation speeds that yield a high steered response power, indicating the resolution of propagation speed estimations.

3.2.5 Overview of alternative beamforming techniques

This section has provided a general overview of delay-and-sum beamforming, particularly in the time domain. Simulations have shown that the theory behind discrete apertures is supported by using the steered response to estimate the spatial spectra. Although only delay-and-sum beamforming has been discussed in this section without much emphasis on weighting beyond its ability to compensate for spatial attenuations if present in the spatial mode, several other beamforming approaches exist [34]. A direct variation on delay-and-sum is the minimum-variance adaptive algorithm. Under assumptions such as white noise and countable narrow-band signals [35], this method aims to artificially improve the resolution of the array by adaptively choosing the weights in Eq. (3.2.1). With similar goals and assumptions, the Multiple Signal Classification (MUSIC) method is commonly used to estimate the directions of arrivals of sources in the far field[23]. For real-time imaging, some methods have been proposed to efficiently compute the steered response [36, 37, 38]. Another example is the delay-multiply-and-sum algorithm, which aims to increase the contrast in the steered response without adding additional sensors, albeit at the cost of increased computation time [39, 40, 41].

Delay-and-sum is chosen for this work as the initial approach for applying beamforming to near-field distributed acoustic sensing measurements. It is the most straightforward method, requiring fewer assumptions, and thus it is useful for isolating problems associated with fibre optic sensing.

Chapter 4

DISTRIBUTED ACOUSTIC SENSING

Distributed Acoustic Sensing (DAS) uses Rayleigh scattering, a physical phenomenon that occurs as light propagates through an optical fibre. This technique allows the optical fibre to function as a distributed sensor for measuring strain and temperature variations along its length. It involves sending coherent light from an interrogator into the fibre and then measuring the phase changes in the light reflected back due to Rayleigh scattering. These changes, which are proportional to variations in temperature or strain, are located along the fibre based on time-of-flight of the propagating light as they are detected by the interrogator. In this way, an optical fibre already installed in a structure or across a terrain can monitor acoustic vibrations at different positions along its length caused by earthquakes or any other acoustic source inducing mechanical vibrations. Distributed Acoustic Sensing is not the only method for using optical fibres as distributed sensors. Other examples include Brillouin and Raman distributed sensors, and Fibre Bragg Gratings, which can be used as point or quasi-distributed sensors [42]. Moreover, even within the DAS technology itself, there are multiple methods to capture and process the measurements. This section focuses on time-domain-based DAS methods, as this is the approach used to capture the DAS data for this thesis, using a commercial DAS interrogator [29, 43, 44].

4.1 Elastic and inelastic scattering

Due to inhomogeneities in a medium, propagating waves scatter owing to several factors as explained in Section 2.4. Particularly, electromagnetic waves (light, whether visible or not) in an optical fibre interact with the imperfections of the medium to form two types of scattering, namely **elastic** and **inelastic** scattering. The difference between these classifications lies in whether the scattered photons of light have exchanged energy with the medium. When there is an exchange of energy, the scattering is said to be inelastic; and when there is none, it is called elastic.

$$E = \frac{hc}{\lambda} \tag{4.1.1}$$

Following Eq. (4.1.1), where h is Planck's constant, c is the propagation speed, and λ is the wavelength [45], the energy of a photon is inversely proportional to its wavelength. This implies that, if due to inelastic scattering, energy is given away to the medium, the frequency of scattered light decreases, and the wavelength increases, resulting in what is known as **Stokes** components of the scattering. Similarly, if energy is acquired from the medium in the scattering process, the

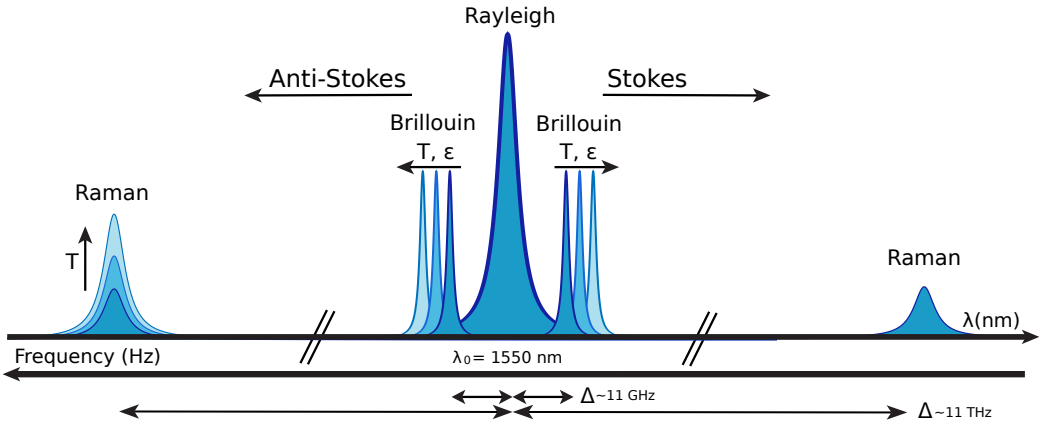

Fig. 4.1: Elastic and inelastic scattering in an optical fibre.

frequency increases and the wavelength decreases, which is known as **anti-Stokes** process. On the other hand, in elastic scattering, there is no exchange of energy with the medium and the wavelength remains the same.

Elastic scatterings are classified as **Rayleigh** and **Mie**, while inelastic scatterings are classified as **Raman** and **Brillouin**. Raman, Brillouin, and Rayleigh scattering in optical fibres can be used for distributed sensing, which means that the back-scattered light received by an interrogator can be utilised to map changes in the measurements of each type of scattering into strain or temperature changes within the fibre (see Fig. 4.1). Distributed Acoustic Sensing, which is associated with Rayleigh scattering, is explained further in subsequent sections.

Rayleigh scattering

The answer to the question, "Why is the sky blue during the daytime and orange at dawn and sunset?" can be explained by understanding the concept of *Rayleigh scattering* [46]. Generally, for electromagnetic radiation where the wavelength is much greater (at least ten times greater) than the particles or molecules in the medium, Rayleigh scattering is the process through which relatively small amounts of energy are redirected in other directions by *elastic* interactions. This means that there is no exchange of energy with the medium, and thus the dispersed radiation retains the same wavelength. The intensity of Rayleigh scattering is proportional to the inverse fourth power of the wavelength of the incident light, a principle known as Rayleigh's law [47]. This means that the blue part of the visible spectrum is more dispersed than the red part. During the daytime, when the white light from the sun impinges perpendicularly on the atmosphere, blue light is dispersed comparatively more than red light, with a large portion of it being dispersed into the same atmosphere, thus giving the sky a bluer hue, while the sun itself appears to shift to an orange/yellowish tone. At sunset, as the radiation from the sun impinges almost parallel to the Earth and travels a longer path through the atmosphere, more blue light is scattered away into outer space, resulting in the red tint of the sunset.

In the context of optical fibres, Rayleigh scattering is caused by microscopic random inhomogeneities within the glass of an optical fibre, such as density and compositional variations, impurities, and other irregularities produced in the fabrication process. These inhomogeneities are typically frozen into the glass during the cooling process as the fibre is made, causing fluctuations in the refractive index that act as small scatterers or mirrors. If the number N of scatterers is known, a

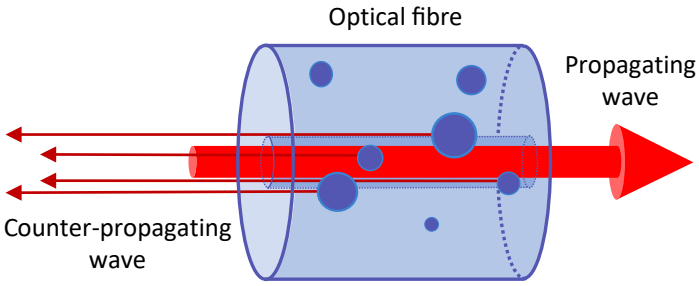

Fig. 4.2: Schematic of Rayleigh back-scattering in an optical fibre. Adapted from [48].

model on the intensity of scattered light I is given by [49]:

$$I = I_0 \frac{8\pi^4 N\alpha^2}{\lambda^4 R^2}(1 + \cos^2\theta), \tag{4.1.2}$$

where α is the polarisability of the molecules of the material, R is the distance from the scatterers and θ is the scattered angle. Note the dependency on $1/\lambda^4$ as explained for Rayleigh scattering in the atmosphere. Light propagating forward is then scattered in all directions as it travels through the optical fibre, and a portion of it is back-scattered into the cone of acceptance of the fibre, which allows it to propagate back (see Fig. 4.2). In silica, the material from which most optical fibres are made, about 5% of the scattered light intensity propagates orthogonally polarised to the incident light, while 95% remains in the original polarisation [49].

In telecommunications, Rayleigh scattering is an undesired, unavoidable property of optical fibres, since it contributes to the total attenuation of the fibre, with a loss in power in the range 0.7-0.9 dB km^{-1} μm^{-4}. This means that at a wavelength of 1 μm, for every metre of fibre the light travels through, about 0.016% of the incident light is lost due to Rayleigh scattering. However, Rayleigh scattering offers significant utility for optical time-domain reflectometry (OTDR) to inspect the fibre in a non-invasive manner, and, more importantly for this thesis, to use the optical fibre as a distributed sensor [1, 4, 49, 50].

Mie scattering

For particle sizes in the propagating medium larger than the light's wavelength, Mie scattering occurs, which is another type of elastic scattering. Compared with Rayleigh scattering, the intensity of Mie scattering is far less dependent on wavelength. This explains the red tint of the sky during a wildfire due to the presence of ash in the atmosphere, or the white or grey colour of clouds due to water droplets much larger than the wavelength of visible light [51, 47, 4].

In the context of optical fibres, Mie scattering is fortunately negligible, as modern fibre production processes have been perfected such that Mie-scale impurities and surface roughness between the core and the cladding are no longer present, at least in silica-based fibres [4].

Raman scattering

In optical fibres, Raman scattering is a type of inelastic scattering where the exchange of energy is due to the interaction of light with molecular vibrations in so-called Raman-active molecules. The energy is exchanged between the incident photon of propagating light and the vibrational states of the molecule. These molecular vibrations are known as *optical phonons* [52, 4].

Brillouin scattering

In contrast to Raman scattering, where the exchange of energy occurs with molecular vibrations called *optical phonons*, Brillouin scattering, which is also inelastic, involves interactions with *acoustic phonons*, hyper-sonic vibrations within the *atomic* lattice. These *acoustic phonons* arise from thermally driven material-density fluctuations that travel at the speed of sound in the fibre. When their acoustic wavelength matches the wavelength of propagating light in the fibre, an exchange of energy can occur between the *photon* and the *acoustic phonon* [4, 53].

4.2 Optical Time-Domain Reflectometry (OTDR)

Originally used for the characterisation of optical fibres in telecommunications, such as measuring the attenuation profile and detecting defects along the fibre [54], OTDR involves sending a probe pulse of incoherent light (varying frequency and phase) with a temporal width of τ_p through one end of the fibre, then measuring the back-scattered light that is sent to a receiver via an optical circulator[1], as illustrated in Fig. 4.3.

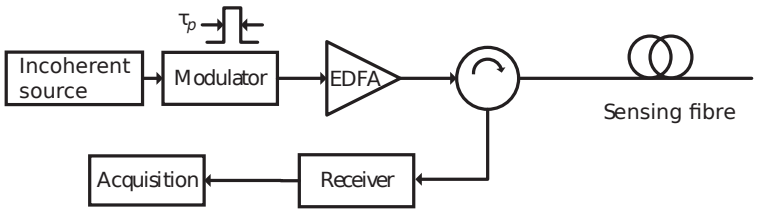

Fig. 4.3: Schematic diagram of a direct-detection intensity-measuring coherent OTDR. Adapted from [4].

As the probe pulse travels through the fibre, it undergoes attenuation due to absorption, scattering, and bending. Of interest at the receiving end is capturing the Rayleigh back-scattered light, which is a portion of all the Rayleigh scattered light within the cone of acceptance of the fibre, as explained in the previous section. This back-scattered light also loses power on the way back, which must be considered for the OTDR trace analysis. To map the spatial locations in the fibre where the reflections occur to the timestamps measured in the receiver, the group propagation speed v_g of light in the fibre must be known. The mapping can be made by simply considering the double path the light has to travel to get back, as $d = v_g t/2$. An example of an OTDR trace for fibre characterisation is shown in Fig. 4.4. The attenuation of the fibre is typically plotted on a logarithmic scale so it can be estimated by the slope.

Following the mapping from time to distance in the OTDR trace, several probe pulses are sent to obtain an averaged estimation of the power loss. Naturally, the probe pulses must not interfere with themselves. To achieve this, the time between sending each probe pulse must be $\Delta t \geq 2L/v_g$, where L is the entire length of the fibre. Finally, the spatial resolution obtained from the mapping depends on the temporal width of the probe pulse τ_p. Two spatial events are resolved when their reflections over the probe pulse do not overlap; considering the two-round trip of the light. Thus, the spatial resolution can be defined as $\Delta d = v_g \tau_p/2$. In an optical fibre, for an effective refractive index $n_g = 1.47$, the group propagation speed can be calculated as c/n_g, where c is the speed of light in a vacuum, which means that an approximate spatial resolution of $\Delta d \approx 10$m for a probe pulse width of $\tau_p = 100$ns [48].

[1] An optical circulator routes light from one port to the next, based on the direction of propagation.

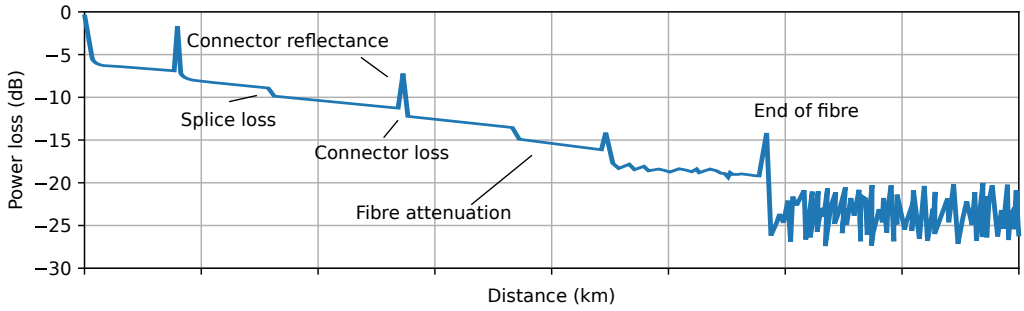

Fig. 4.4: Typical OTDR trace used for fibre characterisation.

4.3 Φ-OTDR and intensity-based DAS

So far, OTDR has been introduced as a method for characterising a fibre by using incoherent light as a probe and taking the average of intensities measured at the receiver after sending several probe pulses. When using narrow-band coherent light, the Rayleigh reflections are, by definition, of the same frequency but have an unpredictable phase that depends on the also unpredictable tiny imperfections of the fibre when it is fabricated. Then, on the way back, the electric fields back-scattered from each resolution cell will have constructive and destructive interferences that are translated into random variations in the power intensity at the receiver end. These variations, although unpredictable, are stable for each position in the fibre, as shown in Fig. 4.5a, where, by using the same probe several times, the Φ-OTDR trace is practically the same, with slight differences mostly attributed to noise.

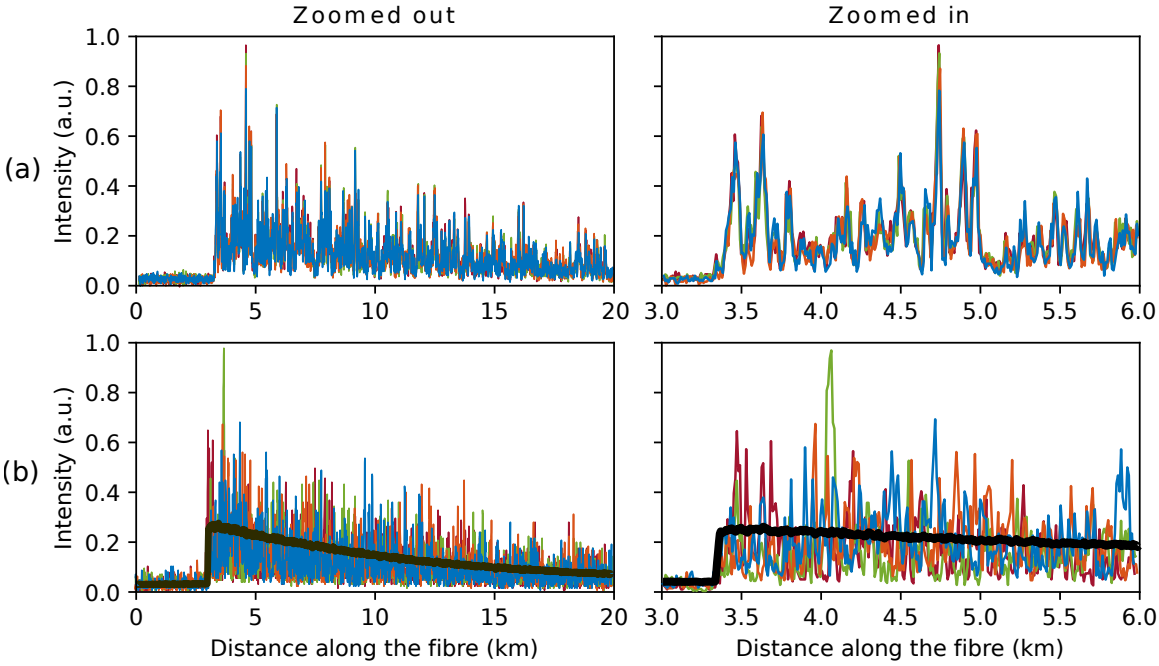

Fig. 4.5: (a) Back-scattered traces for the **same frequency**. (b) Back-scattered traces for **different frequencies**. The black trace is the average intensity OTDR trace. Adapted from [55].

On the other hand, when using an incoherent probe pulse, which contains a wide range of frequencies in its spectrum, as used in conventional OTDR, all these frequency-dependent phase changes are averaged, which allows us to see the exponential attenuation on the fibre in Fig. 4.5b.

When the probe pulse is coherent, and the power is measured at the receiver, the approach is referred to as "phase-OTDR", "phase-sensitive OTDR", or "Φ-OTDR" even though phase is not being measured. Although this may seem counter-intuitive and confusing, as explained before, the unpredictable but stable variations in back-scattered power are due to phase discrepancies, and this is the main reason why it is called this way. This should not be confused with dΦ-DAS, which is explained in the following section.

Now, the question arises as to how the intensity from a Φ-OTDR can be used for distributed vibration sensing. When a section of the fibre is disturbed either by strain or temperature changes, its refractive index will change, and with it, the intensity of the Rayleigh back-scattered light. This variation can be measured and compared with a reference Φ-OTDR trace to detect where the disturbance is caused. In Fig. 4.5a, this could be seen as one of the traces diverging significantly from the average in one section of the trace. However, this method has a major disadvantage for distributed vibration sensing: **the amplitude of the vibration is not proportional to the variation of the optical intensity, nor is the transfer function linear** [50, 4]. To illustrate this, Fig. 4.6 shows the results of an experiment [4] where strain is applied uniformly to a 40-metre section of an optical fibre, located between 40 and 80 metres from the interrogator, to stretch it periodically at a frequency of 105Hz. Along the horizontal axis, intervals of 40ms are displayed side by side for 15 different probe wavelengths (referred to here as optical carrier frequencies). Due to the 105 Hz strain vibration, no more than four periods should be observed in each 40ms interval. The back-scattered amplitude of two channels within the 40-metre section, at 50 m and 70 m, is plotted in blue (top) and orange (bottom), respectively. It can be noted that the transfer function is different for each optical frequency offset (relative to a nominal laser wavelength) and location, being

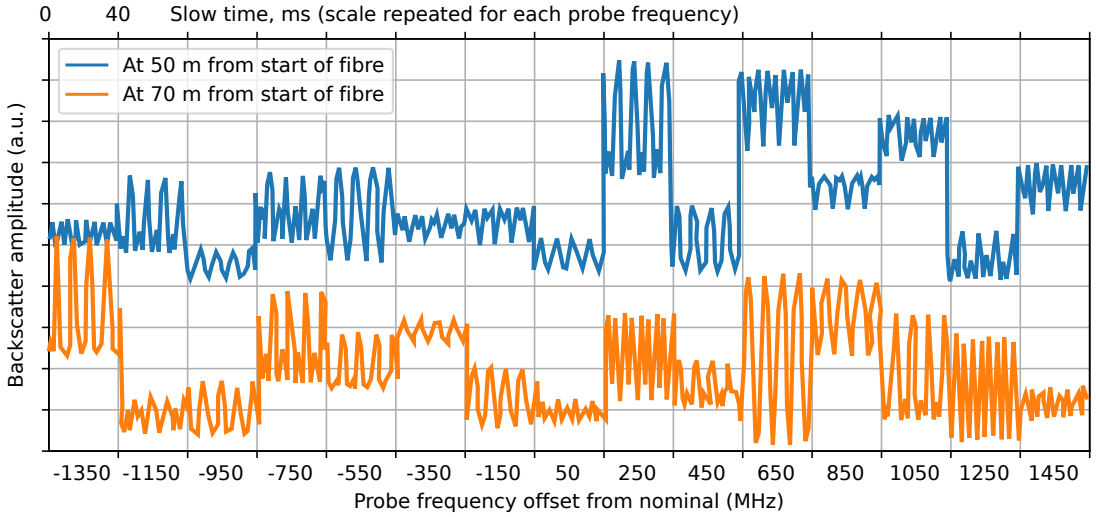

Fig. 4.6: Distributed strain is applied uniformly to a fibre between 40 and 80 metres at 105 Hz using a piezoelectric transducer. The measurements for each probe optical frequency are plotted side by side for 40ms intervals, referred to as *slow times* to distinguish them from the *fast times*, which relate to the distance mapping within the fibre for each probe pulse. Intensity extracted vibration transfer function changes with various optical frequencies and locations. Adapted from [4].

subject to drifts and usually non-linear. This variability in the transfer function can be observed at probe frequency offsets that show a double-frequency oscillation, such as at 250 MHz and 1450 MHz. Additionally, even though the strain is applied uniformly (with the same intensity) along the fibre segment, the gain of the transfer function varies even when using the same probe frequency. For example, at 650 MHz, the orange (bottom) curve has a greater amplitude.

The conclusions from the example in Fig. 4.6 indicate that intensity-based DAS is not reliable for precision measurements of strain variations, as the transfer function is highly unpredictable and subject to changes with ambient conditions, thus not being time-invariant. However, it is still useful for applications where detecting and classifying disturbance events is required. Even though precise measurements of vibration cannot be obtained, other general features from the signals can be extracted for their classification [56, 4]. Sensors based on this non-linear response of the Rayleigh intensity light are named Distributed Vibration Sensors (DVS) and are useful for detecting perturbations but not for retrieving their waveform. On the other hand, DAS allows the precise measurement of perturbations due to the linear response of the Rayleigh optical phase to temperature and strain.

4.4 Phase based DAS (dΦ-DAS)

Just as the intensity of the back-scattered light is determined by the summation of the electric fields re-radiated by the scatterers within the section of the fibre occupied by the probe pulse (within a resolution cell), so too is its phase. The interference between sinusoidal waves with different phases and amplitudes indeed results in another sinusoidal wave with a different phase and/or amplitude. It was concluded in the previous section that intensity-based Φ-OTDR is ill-suited for precision vibration measurements due to the non-linearity, unpredictability, and variability of the transfer function between strain and changes in back-scattered power. However, the variations in phase have a linear relationship with variations in strain [57].

Generally speaking, in a single-mode fibre (SMF) the optical phase ϕ has a linear relation with the distance travelled in a section L_0 given by [58, 59]:

$$\phi = (2\pi n/\lambda_0)\, L_0 = \beta L_0 \tag{4.4.1}$$

where λ is the wavelength in the vacuum, n is the core's refractive index and β is the propagation coefficient in the fibre. When an external vibration is applied to an optical fibre, strain is generated, resulting in changes to the fibre length, the refractive index of the fibre core, and the core diameter. These changes occur due to the longitudinal strain itself ΔL_0, the photo-elastic effect[2] Δn, and the Poisson effect[3] ΔD, respectively, such that [58, 59, 55]:

$$\Delta\phi = \beta\Delta L_0 + L_0\Delta\beta = \beta\Delta L_0 + L_0(\partial\beta/\partial n)\Delta n + L_0(\partial\beta/\partial D)\Delta D \tag{4.4.2}$$

where D is the core diameter, and $\Delta\phi$ is the phase change caused by ΔL and $\Delta\beta$, the changes in fibre length and in the propagation coefficient in the fibre respectively.

A resolution cell in an optical fibre is determined by the width of the probe pulses, as explained in Section 4.2. Within it, the combination of all the random scatterers functions as a mirror that reflects light with a specific change in phase. Since strain causes displacement in the fibre, generating unpredictable phases between resolution cells, the differential phases are measured between closely

[2] Change in the refractive index caused by strain.

[3] A longitudinal strain in a material is accompanied by a lateral strain. As the length increases, the lateral dimensions decrease. This is known as the Poisson effect.

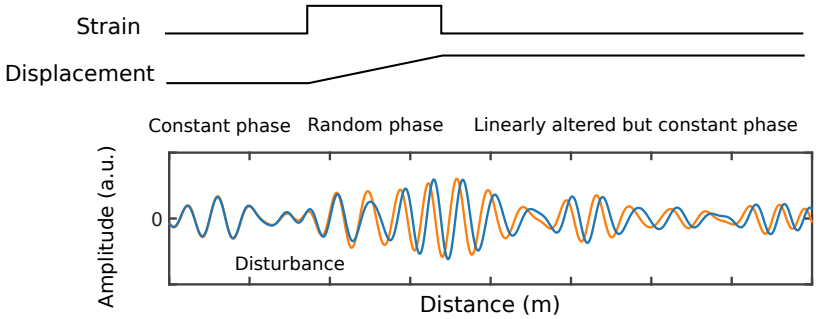

Fig. 4.7: Qualitative schematic showing strain on the fibre, the resulting displacement and the effect on the phase of the back-scattered signal. Adapted from [4, 60].

spaced but non-adjacent resolution cells, typically in an interval known as **gauge length** or **differentiating interval**. Fig. 4.7 presents a schematic that qualitatively illustrates the relationship between fibre displacement and phase change. Within the section of fibre where the displacement occurs, the phase varies unpredictably with respect to the displacement. However, in the sections of the fibre before and after where the strain is applied, the phase remains constant and can be measured reliably. This gauge length defines the true spatial resolution in a $d\Phi$-DAS system, namely the ability to resolve or distinguish two separate and independent vibrations located at different points along the fibre. Fig. 4.8 illustrates this, where the DAS channels represent the discrete spatial points along the fibre, mapped in fast-time at each interrogation of the fibre.

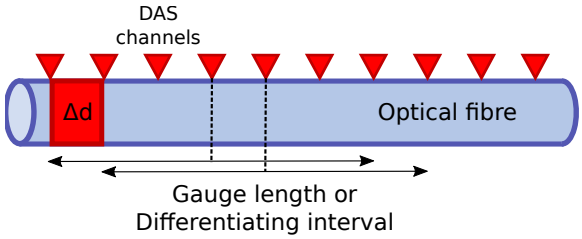

Fig. 4.8: Schematic showing the differential interval or gauge length. The phase is compared between two close, but not necessarily adjacent, resolution cells. Adapted from [61].

The phase differences measured between differentiating intervals are ambiguous in the sense that only phases in the interval $[-\pi, \pi]$ can be measured. This measured phase is referred to as *wrapped* phase, and in order to correctly map the phase variations to variations in strain, a phase *unwrapping* algorithm must be applied to the wrapped measurements [62]. This method is reliable provided that the signal is sampled sufficiently frequently, relative to the bandwidth, to ensure that the changes between subsequent samples are never more than π [4].

Fig. 4.9 shows a straightforward example where a sinusoidal vibration is applied to an optical fibre approximately 210 metres from the interrogator. The unwrapped phase is obtained by applying the phase unwrapping algorithm to the raw phase measurements. On the right, differentiating the unwrapped phase over one gauge length restores the localisation of the disturbance.

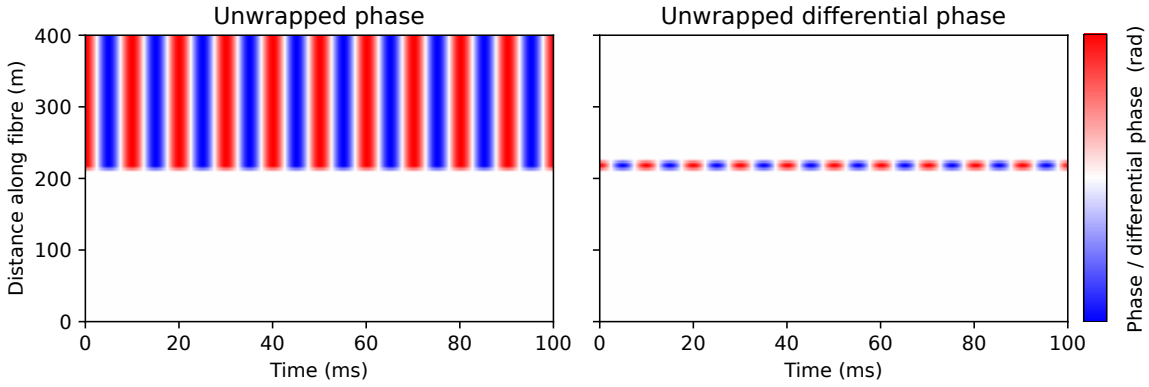

Fig. 4.9: Phase displayed as a function of slow time (x-axis) and fast time/distance along the fibre (y-axis). On the left, the phase variation, and on the right, the same data after applying a spatial differentiation operation. Adapted from [4].

4.5 Summary and array processing limitations

Distributed Acoustic Sensing operates by sending coherent laser pulses through an optical fibre. A portion of the light is reflected back due to irregularities in the fibre through a process known as Rayleigh scattering. The interrogator processes the phases of the back-scattered light, which are unwrapped and differentiated in so-called *differentiating intervals* or *gauge lengths*. Elastic deformations in the fibre caused by strain lead to phase shifts in the reflected laser pulses, which can be linearly mapped to strain variations along the fibre.

The application of array processing to DAS measurements is not straightforward, as they exhibit specific limitations that must be addressed, which are usually not present in ideal point sensors used in array processing theory. Here, some main considerations are outlined.

Directional sensitivity to acoustic waves: Phase variations in DAS measurements are mainly sensitive to longitudinal length variations caused by strain. As a consequence, the directivity sensitivity pattern of a straight optical fibre to acoustic waves is modelled as $\cos^2\theta$, as shown in Fig. 4.10, with a maximum when the wave impinges on the fibre longitudinally [63, 64, 65, 66, 67, 2, 3].

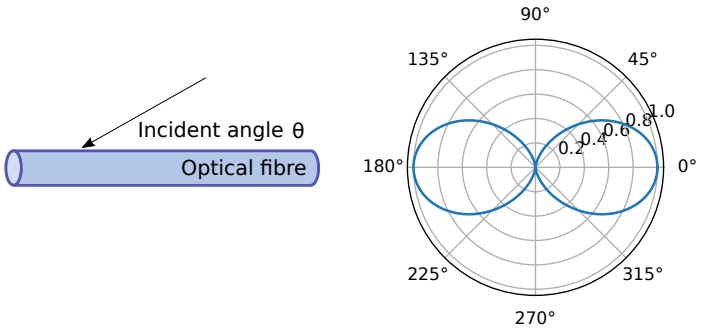

Fig. 4.10: Optical fibre's directional sensitivity to (acoustic) P-waves, modelled as $\cos^2(\theta)$.

Poor fibre coupling: The effectiveness of a DAS sensor in measuring vibrations is affected by the quality of the fibre's adherence to the environment through which the acoustic waves propagate. Poor coupling between the fibre and its surrounding medium in certain sections can result in some channels detecting inconsistent vibrations due to varying gains, leading to different signal-to-noise ratios [68].

Uneven longitudinal response: Even with ideal coupling and high directional sensitivity, the phase extraction process of back-scattered light can cause an uneven longitudinal response. Low-intensity back-scattered light at unpredictable sections of the fibre, caused by fading, results in unreliable phase extraction due to a low signal-to-noise ratio, affecting the reliability of strain estimations.

Non-uniform spatial distribution of the fibre: As a consequence of the acoustic directivity inherent in optical fibres, conventional array configurations such as uniform linear or planar arrays are not directly applicable. As exemplified in Section 3.2.3, a Uniform Linear Array achieves its highest resolution for waves impinging perpendicularly (at an incident angle of $\theta = 90°$). However, when using a straight fibre as an array, the directional sensitivity is minimal at this angle. When designing DAS arrays, it is ideal to position with as many orientations relative to the directions of wave propagation as possible.

Chapter 5

ANALYSIS OF *DAS* MEASUREMENTS

To apply array processing techniques in real Distributed Acoustic Sensing measurements, the public dataset *PoroTomo natural laboratory horizontal and vertical distributed acoustic sensing data* [29, 69, 8] is employed, following the work presented in [5], to provide a basis for comparison: In March 2016, multiple arrays of sensors were deployed at Brady Hot Springs, Nevada, USA, including optical fibres for both Distributed Acoustic Sensing (DAS) and Distributed Temperature Sensing (DTS), and 246 three-component seismographs[1], three pressure sensors in observation wells, geodetic measurements at three GPS stations, and seven satellite images using Synthetic Aperture Radar (SAR). The purpose of these deployments was to conduct seismology, geodesy, and hydrology studies on the soil around an elliptical area of 4 km by 1.5 km, by using the combined measurements of all deployed sensors. This work will only use the measurements from the horizontally deployed optical fibre in a 1500 by 500 metre area at 0.5 metres in depth for independent DAS array processing analysis. As a means to generate seismic vibrations in a controlled setting, a *vibroseis* truck is used to inject a chirped wide-band vibration ranging from 5 Hz to 80 Hz spanning 20 seconds into the earth, at 200 different locations within the deployment area. This vibroseis truck is capable of generating both P-waves and S-waves, by applying the vibration either longitudinally or transversely, respectively. Only the P-wave subset of data is used for this work.

The measurements were taken at four distinct stages, during which the hydrological conditions were intentionally manipulated by modifying the rates of pumping in the injection at nearby production wells. Only the first stage of data is used, where the production wells were operating at a *normal* rate. Regarding the horizontally deployed optical fibre, it consisted of an 8.7 km long fibre with a spatial sampling of 1 m between channels, a gauge length of 10 metres for the actual spatial resolution, and a sampling frequency of 1 kHz. Following the work in [5] and for comparability, an 8630 metres subsection of the fibre is used, that is sub-sampled according to the gauge length, resulting in effectively 863 DAS channels, whose locations are well known. From the 200 locations of source vibrations, a subset of 55 arbitrary locations is chosen, with their respective locations with respect to the fibre shown in Fig. 5.1.

During the four-year span of the study, an earthquake occurred 150 km south-west of the Brady Hot Springs, near Hawthorne, with a local magnitude of 4.3 on the Richter scale, and was also recorded by the DAS array. These measurements are used in this work for beamforming in the far-field.

[1] A three-component seismograph is capable of measuring directions of ground motion in three orthogonal space coordinates.

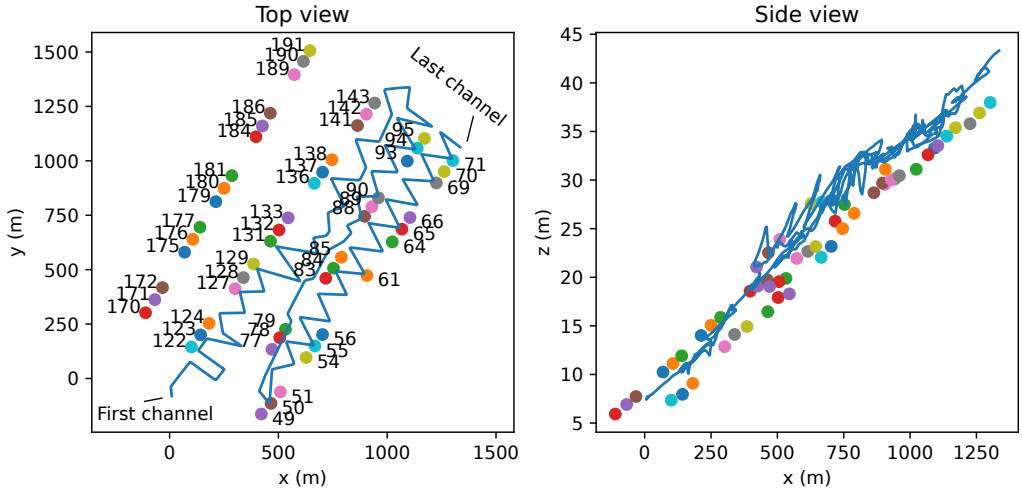

Fig. 5.1: Seismic vibration sources are applied at 200 locations, of which 55 are chosen for analysis. The horizontally deployed optical fibre used for DAS is shown in light blue.

5.1 Data preprocessing

Before applying any array processing algorithm, some preprocessing is performed on the raw measurements obtained from [8]. This includes temporal frequency filtering and amplitude normalisation, followed by the application of a channel sorting method for DAS measurements on single seismic sources, as proposed in [5].

5.1.1 Filtering and amplitude normalisation

A straightforward approach for preprocessing data before applying array processing algorithms involves simply applying a pass-band filter to the signals. In beamforming, this method is specifically referred to as *filter-and-sum* beamforming [6]. Generally, for seismic waves, their frequency range is well known to be below 100Hz; and in this particular case study, the source frequency ranges from 5Hz to 80Hz. A zero-phase, fourth-order digital Butterworth filter within the range [10, 80]Hz is applied to the signals, starting from 10Hz instead of 5Hz, as after inspection, the presence of low-frequency noise in all signals is noticed, likely due to nearby production wells.

Filtering techniques specifically tuned for DAS data, such as the Adaptive Frequency Filter (AFK) approach proposed in [70], assume that the fibre is linearly placed, rendering them unsuitable for this dataset. A self-supervised deep learning approach is proposed in [71] for DAS denoising, which is named jDAS by its authors, also assumes a linear placement of the fibre. Even after segmenting the fibre into linear sections and applying the filter independently to each, the array processing techniques discussed in subsequent sections performed better with the pass-band filter. Particularly, the jDAS approach receives as inputs independent time windows of 2000 samples into its U-Net[2], resulting in undesirable artefacts that negatively impact the phase-correlation-based channel sorting explained in the next section.

[2]A U-Net is a neural network architecture, used among other things for image denoising. It includes an encoder to capture features and a decoder to reconstruct the output. Its *U-shaped* architecture is the origin of its name. [72]

After filtering, amplitude normalisation is applied by dividing all channels by their respective standard deviations, s:

$$s = \sqrt{\frac{\sum_{i=0}^{N-1} (x_i - \overline{x})^2}{N-1}}, \tag{5.1.1}$$

where x_i represents the time sample values, $\overline{x}$ is their mean, and N is the total number of time samples. This is done to equalise the impact of each channel in delay-and-sum beamforming due to the unknown propagation properties of the environment. Also, variability in channel gains arises from directional directivity, potential poor fibre coupling, and intrinsic difficulties in reliably extracting phase information due to fading, leading to unreliable strain estimations in some sections. It is not straightforward to attribute variations in amplitude to these factors independently, so a simple normalisation solution is convenient and is also used in other works for DAS processing [2, 5, 7]. Note that the normalisation can be considered as weighting when applying delay-and-sum beamforming.

Figures 5.2a and 5.2b show the DAS measurements for the experiment at position 190 of the

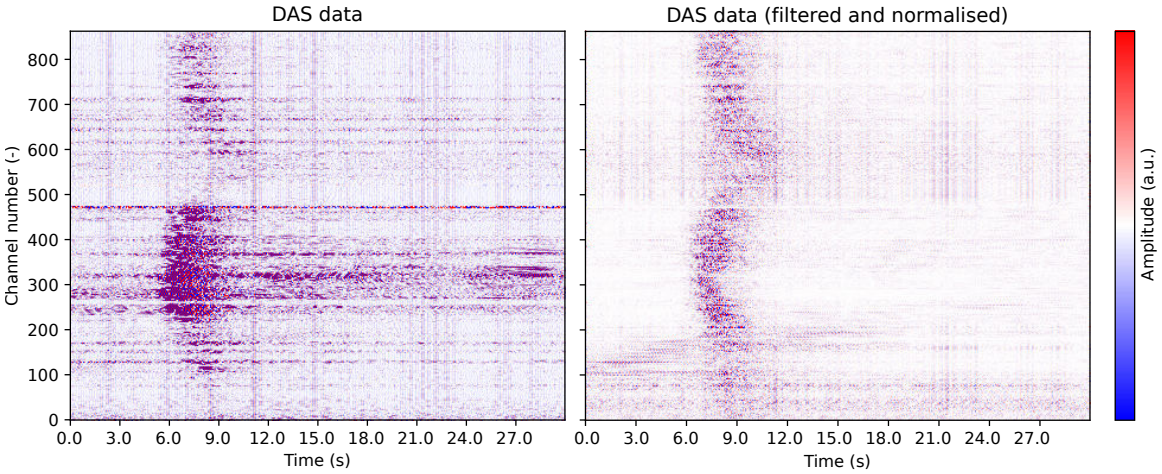

(a) Data are displayed as an image, using a diverging seismic colour bar for the amplitude.

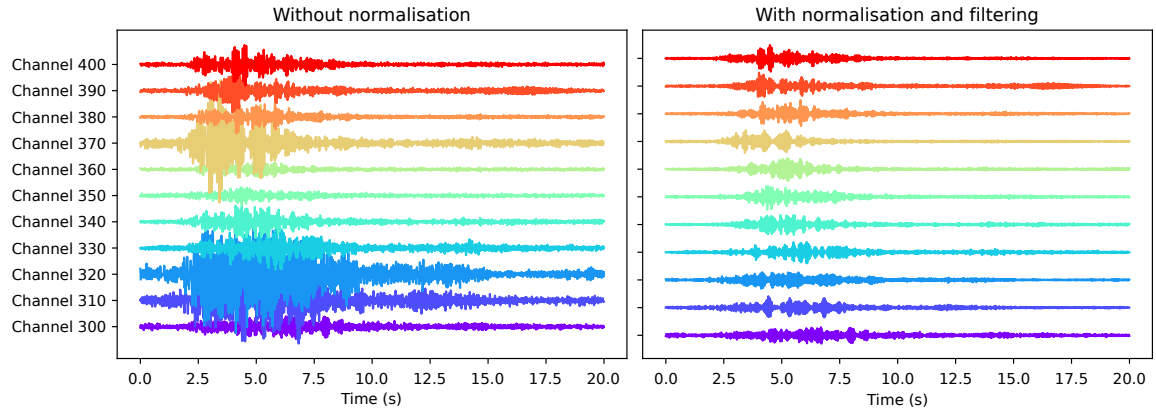

(b) Channels from 300 to 400, displayed in increments of 10.

Fig. 5.2: Measurements from experiment 190 (vibroseis truck position) are displayed before and after filtering and normalisation.

vibroseis truck[3], before and after the filtering and normalisation processes. Between channels 220 and 470, it can be seen that a significant portion of the signals' low-frequency noise has been filtered out. Particularly, this is observed as the lack of high-intensity measurements from the ninth second onwards in the filtered data, possibly due to interferences caused by the pumping of nearby production wells, as reported in [29], which is more prevalent near this section of channels. Outside of this range, where the initial signal amplitude is low, the noise that is not filtered out is relatively amplified.

5.1.2 Channel sorting

In [5], a method for sorting DAS channels for array processing applications is proposed, wherein a so-called reliability score β_i is computed for each channel by considering the phase-cross-correlation among all channels. This channel-sorting approach is proposed because of the limitations of optical fibre sensing, such as directivity, poor coupling and intrinsically unreliable phase extraction due to fading in some sections during the sensing fibre's interrogation. Some channels may produce unreliable measurements, and their use can detrimentally affect array processing results. This method has the particularity of being blind to the spatial properties of propagating waves: it considers each channel independently of its location for the ranking computation. Throughout this chapter, the channel sorting approach will be tested in triangulation and beamforming techniques for seismic source location estimations, along with slight variations in the definitions of the reliability score β_i depending on the application.

Phase cross-correlation function (PCCF)

Let $x_a(t)$ be the analytical signal of a **real-valued** signal $x(t)$, defined as [73]:

$$x_a(t) \triangleq \mathcal{F}^{-1}\{X(f)\cdot 2\mu(f)\} = x(t) * \left(\delta(t) + \frac{j}{\pi t}\right) = x(t) + j\left(\frac{1}{\pi t} * x(t)\right) = x(t) + j\mathcal{H}\{x(t)\}, \quad (5.1.2)$$

where $\mathcal{H}\{x(t)\} \triangleq \hat{x}(t)$ is the Hilbert transform of $x(t)$, $\mu(t)$ is the Heaviside step function, $\mathcal{F}^{-1}\{\cdot\}$ is the inverse Fourier transform operator, and $X(f)$ is the Fourier transform of $x(t)$.

The phase cross-correlation is referred to as such because it uses the phase $e^{jb(t)}$ of the analytic signal $x_a(t) = x(t) + j\hat{x}(t) = a(t)\cdot e^{jb(t)}$ for the calculation. For a pair of discrete real-valued signals $x_1(t)$ and $x_2(t)$, the PCCF is then defined as follows:

$$\mathrm{PCCF}[n] = \Re\left\{\frac{1}{N}\left(e^{jb_1[n]} \star e^{jb_2[n]}\right)\right\} = \Re\left\{\frac{1}{N}\sum_{m=0}^{N-1} e^{-jb_1[m]}e^{b_2[m+n]}\right\}, \quad (5.1.3)$$

where $(f \star g)[n] \triangleq \sum_{m=0}^{N-1}\overline{f[m]}g[m+n]$ is the cross-correlation function, N is the number of time samples, $e^{jb_1[n]}$ and $e^{jb_2[n]}$ are the respective phases of the analytical signals of $x_1(t)$ and $x_2(t)$. The magnitude of the analytical signal is often associated with the amplitude of the envelope of the real-valued signal. In the definition of the PCCF, a cross-correlation is performed between two analytical signals normalised by their respective magnitudes, $a(t)$. This essentially means that the instantaneous phases of the signals are correlated, whilst ignoring variations in the envelope that may result from constructive or destructive interferences as waves propagate through space.

The PCCF can be efficiently computed using the Fast Fourier Transform (FFT), for example with Python's SciPy correlate function, and SciPy Hilbert function for obtaining the analytical signal.

[3]When referring to experiments followed by a number, these refer to the vibroseis positions when generating each seismic vibration in Fig. 5.1.

Global reliability score β_i and local similarity κ_{ij}

The PCCF is used to compute a local indicator, κ_{ij}, which serves to quantify the similarity between two channels i and j. This indicator is calculated by taking the ratio of the maximum absolute value of the PCCF to the root mean square (RMS) of an arbitrary window W surrounding it:

$$\kappa_{ij} = \frac{\max\left(|\mathrm{PCCF}_{ij}|\right)}{\mathrm{RMS}(W)}, \qquad \mathrm{RMS}(W) = \sqrt{\frac{1}{2L}\sum_{W}\mathrm{PCCF}_{ij}^2(W)}. \tag{5.1.4}$$

In this equation, W denotes the window of length $2L$, excluding the value of the maximum absolute of the PCCF (the central value of the window). Following the work described in [5], the length L is defined as twice the sampling frequency. In this instance, $L = 2000$ samples, which is equivalent to two seconds, given a sampling frequency of $fs = 1000$ Hz.

The global reliability score β_i for each channel i is calculated by first computing κ_{ij} for all channels i (resulting in a symmetric matrix of size $M \times M$, where M is the number of DAS channels). Subsequently, the global reliability vector β, which includes all β_i for all channels i, is calculated as the RMS value of κ_{ij} over j for each channel i, and for $i \neq j$, as follows:

$$\beta_i = \sqrt{\frac{1}{M-1}\sum_{j=0}^{M-1}\kappa_{ij}^2}. \tag{5.1.5}$$

Fig. 5.3a shows an example of κ_{ij} for $i = 752$. The RMS value is depicted as a horizontal red line, which corresponds to $\beta_{752} = 6.47$. The vertical red line indicates the channel i to which the κ vector corresponds. The reliability scores β_i for all $M = 863$ channels are plotted in Fig. 5.3b. The channel sorting method simply involves selecting the m channels with the highest β_i or κ_{ij} values relative to a reference channel j, and using them accordingly for different array processing applications, as will be explained in the following sections.

As mentioned, the $M \times M$ κ matrix is symmetrical. To take advantage of this property, only one half of the matrix, including the diagonal, is computed in the implementation of this work, thereby reducing the computational time by nearly half. However, the intrinsic quadratic time complexity,

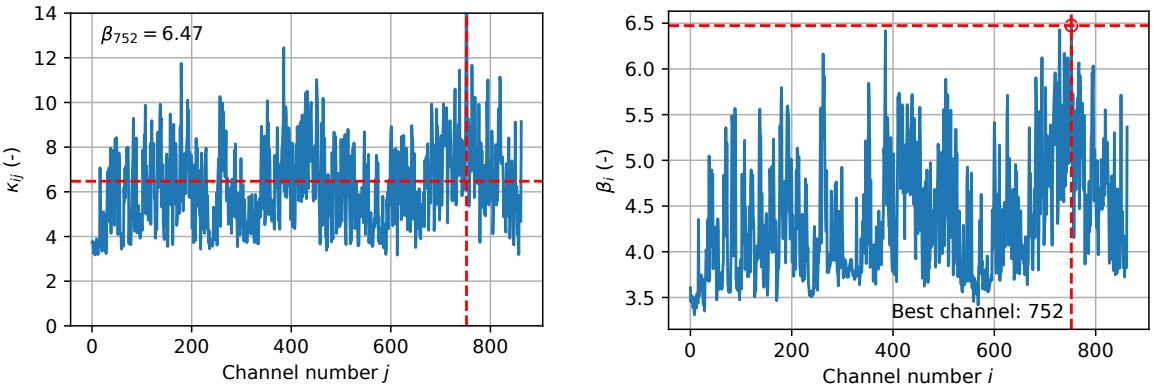

(a) Local similitude κ_{ij} for $i = 752$. **(b)** Global reliability β_i.

Fig. 5.3: Values κ_{ij} and β_i used for channel sorting, computed for experiment 190. The absolute value of the PCCF is used for this example.

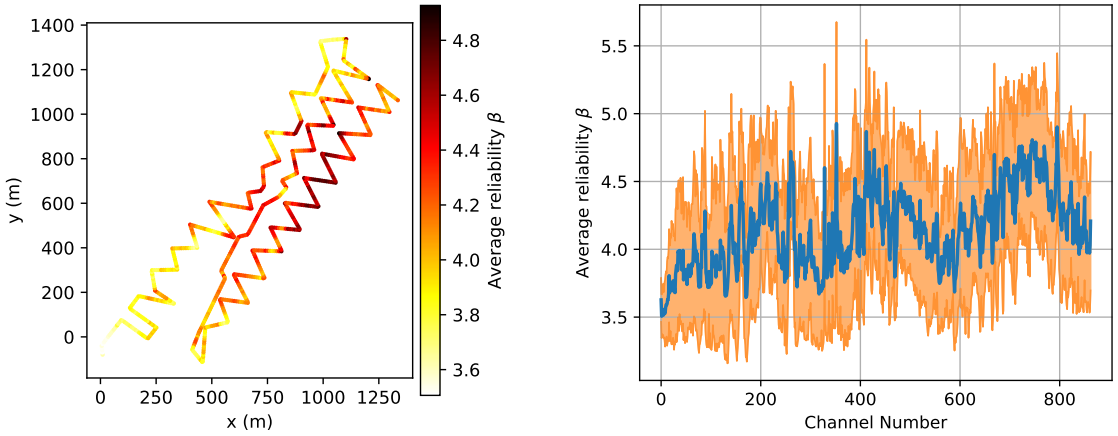

(a) Average β displayed in space.

(b) Average and standard deviation of β.

Fig. 5.4: The average and standard deviation of the β vectors are computed across all 55 experiments. (a) The average is displayed spatially along the fibre. (b) The average is plotted in blue, with the orange area representing the range obtained by adding and subtracting the standard deviation from the average.

represented as $O(M^2)$, remains a disadvantage of this method. This is another reason why processing all 8630 original channels, sampled every metre, was not feasible.

As previously mentioned, the channel sorting method was proposed to blindly discard channels that could detrimentally affect array processing performance. A channel might exhibit low SNR measurements because, in a particular experiment, the vibration source is located in such a way that the fibre's directivity towards it is low. If this were the only reason for low SNR, then each channel should have, on average across differently located sources, around the same reliability score β_i. Fig. 5.4 demonstrates that some sections of the fibre consistently show lower reliability scores on average across all experiments, which could be attributed to poor coupling to the ground. However, this analysis is not conclusive, as the spatial distribution of vibration sources could introduce a bias.

5.2 Triangulation

Although the primary focus of this thesis is the evaluation of delay-and-sum beamforming applied to near-field DAS measurements, this section will expand upon the triangulation method for single source location proposed in [5], mainly by discussing the implications for the channel sorting method in this application.

5.2.1 Time difference of arrival (TDOA)

The hyperbolic triangulation method applied in [5] requires the computation of the times differences of arrival (TDOA) with respect to a reference channel. The reference channel is selected as the channel i with the highest global reliability β_i, as it is assumed that the actual source signal is unavailable for comparison. The TDOAs are computed as:

$$\mathrm{TDOA}_j = \arg\max\left(|\mathrm{PCCF}_{ij}|\right) \tag{5.2.1}$$

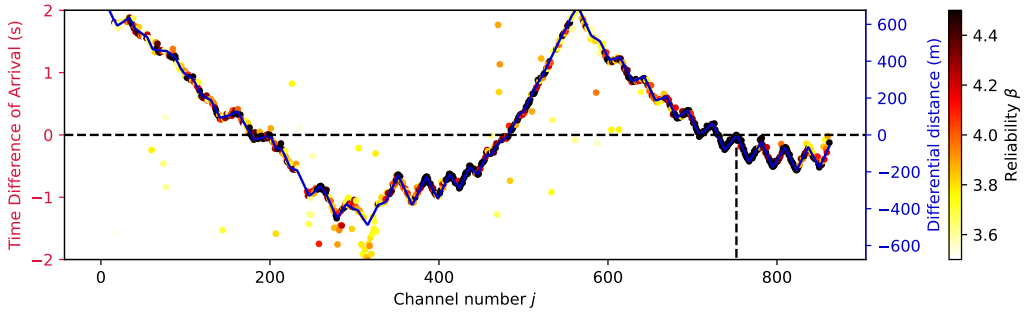

(a) TDOAs on the left vertical axis and differential distances on the right axis. Both TDOA and differential distances are zero for the reference channel 752.

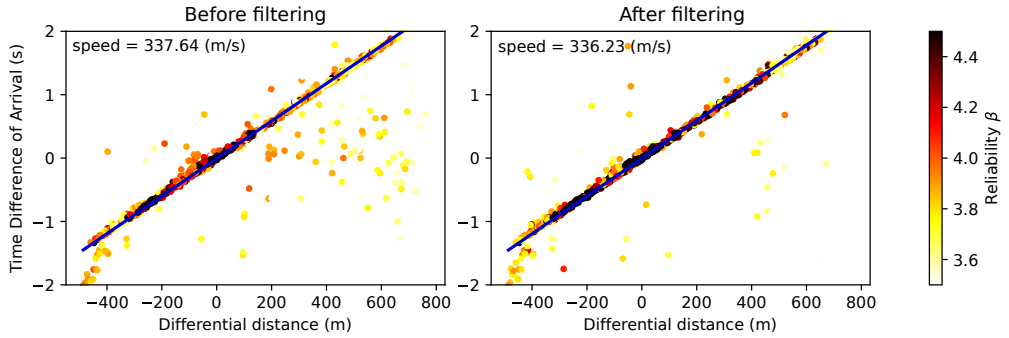

(b) TDOAs on the vertical axis and differential distances on the horizontal axis. The inverse slope of the blue fitting line, obtained by RANSAC, represents the propagation speed.

Fig. 5.5: Time differences of arrival are shown scattered along the differential distance to the actual source location for experiment 190. The reliability β for each channel is displayed using a colourmap.

for the reference channel $i = r$. That is, the argument where the absolute value of the phase-cross-correlation function reaches its maximum. Fig. 5.5a displays the time differences of arrival as a function of the channel number j, for the highest reliability channel $i = r = 752$ in the experiment 190. For comparison, the right-hand side vertical axis plots the differential distance relative to the actual source location. This distance is computed by subtracting the distance from the reference channel i to the source from the distance of every other channel j to the source, as illustrated in Fig. 3.6 in Section 3.2. To scale the differential distances in metres to TDOAs in seconds, a propagation speed of 336 m/s is assumed, estimated by linear fitting using Random Sample Consensus (RANSAC)[74] to exclude outliers. Fig. 5.5b compares the fitting of the TDOAs before and after applying Butterworth pass-band filtering to the data. The number of outliers decreases post-filtering, and the speed estimation remains consistent due to the RANSAC algorithm selecting subsets of data without outliers for optimal fitting. In general, it is observed that channels with the highest reliability β exhibit TDOAs within a linear trend, although this is not always the case, as seen from channels 500 to 600, which show low reliability yet accurate fitting, alongside some outliers with high reliability but inaccurate TDOA estimations. Specifically, when sorting the TDOAs using κ_{rj}, the 600 best channels exhibit a standard deviation of 59 ms when filtered, and 357 ms when unfiltered. When using all 863 channels, a standard deviation of 796 ms is observed for filtered data and 710 ms for raw data. It is the decrease in dispersion with fewer channels that is important, as the goal of the channel sorting method is to employ fewer overall channels while

discarding unreliable ones. However, this example is just one of the best among the 55 experiments, and is chosen just for illustration.

5.2.2 Normalised cost function and mode methods

Once all TDOAs are computed for the reference signal $i = r$, they are sorted using the quantity κ_{rj} defined in Eq. (5.1.4), instead of the global reliability β, since for this application we are particularly interested in the similarity to the reference. The hyperbolic triangulation method fundamentally involves finding the values (x, y, z, v) where the blue curves in Fig. 5.5 are best fitted in norm $L1$ to the scattered TDOAs. Based on this description, the cost function to minimise is defined as:

$$J(x, y, z, v) = \sum_{j=0}^{m-1} \left| (d_j(x, y, z) - d_r(x, y, z)) - v \cdot \mathrm{TDOA}_{rj} \right|, \tag{5.2.2}$$

where the m most reliable channels according to the local similarity between channels κ_{rj} are used to align the differential distance $(d_j(x, y, z) - d_r(x, y, z))$ to the TDOAs_{rj} scaled by the propagation speed v. The norm $L1$ (absolute value) is used on the addends to reduce the impact of outliers. The inverse of this cost function is plotted in Fig. 5.6 for experiments 56 and 180. It can be observed that the use of more channels does not necessarily provide better results. For experiment 56 in Fig. 5.6a, approximately 4% of the total available channels, 34 channels, give a reasonably good estimation when the cost function $J(x, y, z, v)$ is minimised (its inverse is maximised). Another distinction between these two experiments is the *resolution* achieved. For source location 180 in Fig. 5.6b, further away from the centroid of the array, drawing from near-field beamforming theory, there is a noticeable decrease in range resolution compared to source location 56. This *resolution* is also influenced by the degree of dispersion of TDOAs relative to the actual source location scaled by the actual propagation speed: a greater dispersion will result in a low cost function $J(x, y, z, v)$ value across a broader range of arguments. In conclusion, the hypothesis of the channel sorting method

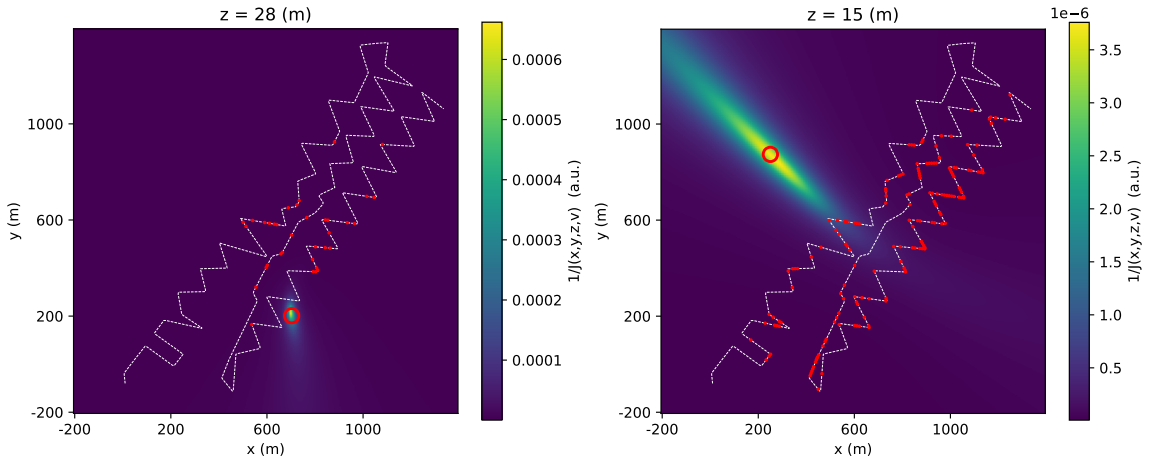

(a) Experiment 56 with 34 most reliable channels. An estimation error of 3.2m is achieved.

(b) Experiment 180 with 165 most reliable channels. An estimation error of 9.0m is achieved.

Fig. 5.6: The inverse of $J(x, y, z, v)$ for $v = 338$m/s and $v = 347$m/s is plotted for Experiments 180 and 56, respectively. The red dots indicate the most reliable channels used for the minimisation of the cost function in each case, and the red circle indicates the actual (x, y) location of the acoustic source.

for the triangulation application is that selecting fewer but more reliable TDOA estimations would be more advantageous than choosing a higher number of channels with decreasing TDOA estimation reliability. This is demonstrated later in this section with an analysis of all 55 employed vibroseis experiment sources.

The minimisation of the cost function is done using the Sequential Least Squares Programming algorithm (SLSQP) [75], which requires only an initial guess and does not require a predefined range of search for the arguments. The initial spatial coordinates (x, y, z) are taken from the reference channel, and an arbitrary value of $v = 335$ m/s is used for the initial guess of the propagation speed. The cost function is constrained to a constant z plane, assuming that the source's coordinate along this axis is known. This constraint is applied to reduce computation time, and due to the fibre's limited extension in the z dimension compared to its horizontal extension (see Fig. 5.1), the array's intrinsic resolution in this coordinate is low, resulting in high variability in the identified minima.

The results of the minimisation process for combinations of channels from $m = 4$ to $m = M = 863$ are shown in Fig. 5.7 for experiment 180. Here, the ground truth coordinates are displayed with a red dashed horizontal line, while the blue points indicate the estimations for each number of channels used, m. This particular experiment appears to yield reasonably accurate measurements for more than half of the channels. The accuracy of the estimations begins to decline from $m = 500$ channels onwards, meaning that the sorting method successfully kept the worst channels to the final positions.

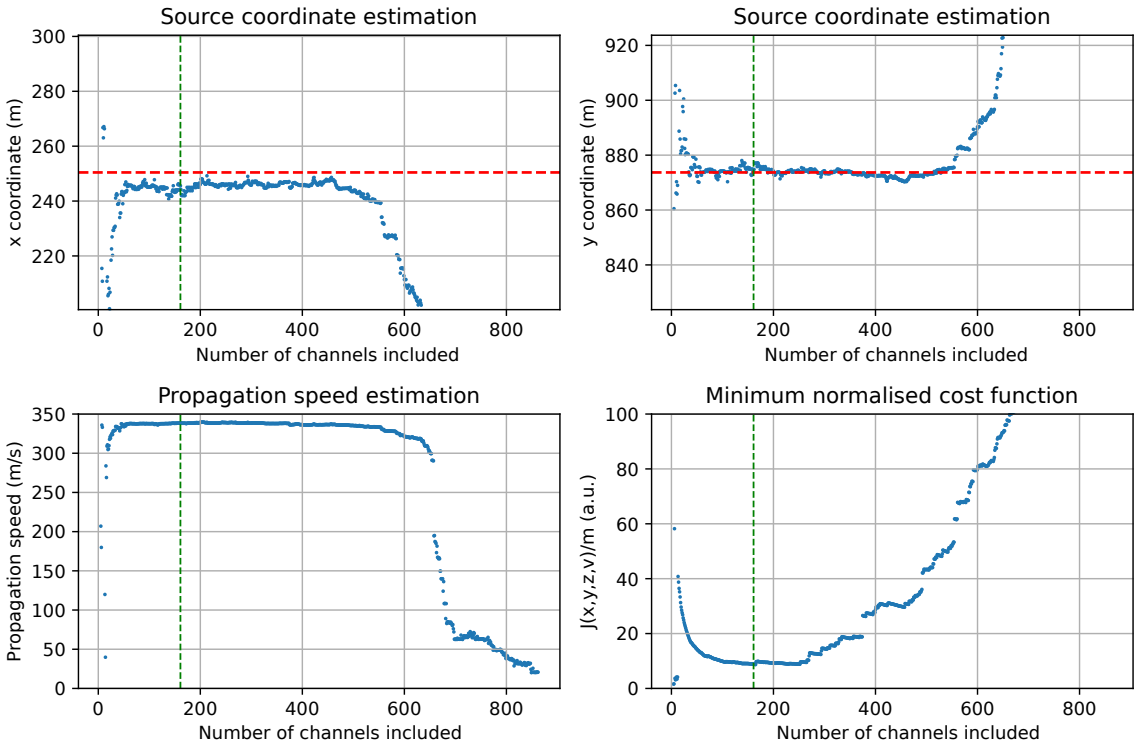

Fig. 5.7: Minimum arguments of the cost function for each channel combination m are plotted in blue, based on κ_{rj}. The minima of the normalised cost function $J(x, y, z, v)/m$ is shown in the fourth subplot. Red dashed lines indicate ground truth, and green dashed lines mark the stopping condition for the normalised cost function method at $m = 165$ for experiment 180.

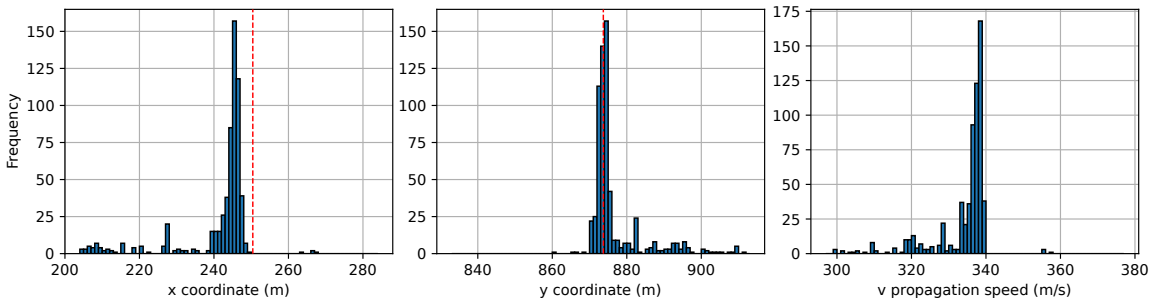

Fig. 5.8: Minimum arguments of $J(x, y, z, v)$ for each channel combination m are arranged in histograms with bins of size 1 m and 1 m/s. The red dashed vertical line represents the ground truth. In [5], the final estimate is defined as the most repeated bin for each argument.

At each step m, the minimisation of $J(x, y, z, v)$ requires increasingly more computation time, as a new term is added to Eq. (5.2.2) each time. This increase in computation time, which is $O(m)$ for each individual combination of channels m, results in a computational complexity of $O(m^2)$ when computing all combinations in ascending order of channels used[4]. For this reason, and because similar estimates are obtained up until 500 channels, even if the estimation is not worsened, it would be computationally more efficient to establish a stop condition that, without knowledge of the actual source location, determines an optimum number of combinations of channels, m, to obtain the final estimate. This stop condition is defined in this Thesis when the normalised cost function $J(x, y, z, v)/m$ reaches its minimum after an arbitrary number of channels, $m = 34$, which empirically provided robust results for the 55 experiments in the available dataset.

In [5], the optimal estimate is calculated by arranging the minimum arguments presented in Fig. 5.7 into a histogram and selecting the most repeated bin, namely the mode of the data, as the final estimate. As illustrated in Fig. 5.8, the minimum arguments for each combination of channels m are organised into histograms with bins of 1 m and 1 m/s for spatial coordinates (x, y) and propagation speed v, respectively. One disadvantage of this method is having to compute all channel combinations m beforehand, which, as mentioned earlier, is computationally demanding.

Also, when replicating this method across all 55 experiments, since each argument is determined independently through its respective coordinate mode, the propagation speed estimation sometimes results in completely wrong estimates, particularly when the majority of channels in certain experiments provide inaccurate TDOA estimations. In these cases, the minimisation of $J(x, y, z, v)$ tends to diverge earlier compared to experiment 180 in Fig. 5.7, and the propagation speed estimates converge to nearly zero values, which, as they are the most repeated values, are yielded as the final estimate of the mode method. This is better exemplified in the next section with a statistical analysis for all experiments.

5.2.3 General results and comparisons

The errors in the estimations of the actual source locations for both the mode method and the normalised cost function method are depicted in Fig. 5.9 as histograms, together with the respective propagation speed histograms and the distribution of errors for each vibroseis experiment in the space along the fibre. Here, it can be observed that the errors obtained by both methods follow a similar

[4]This can be corroborated by considering the individual computing times at each step as each one of the addends of an arithmetic series.

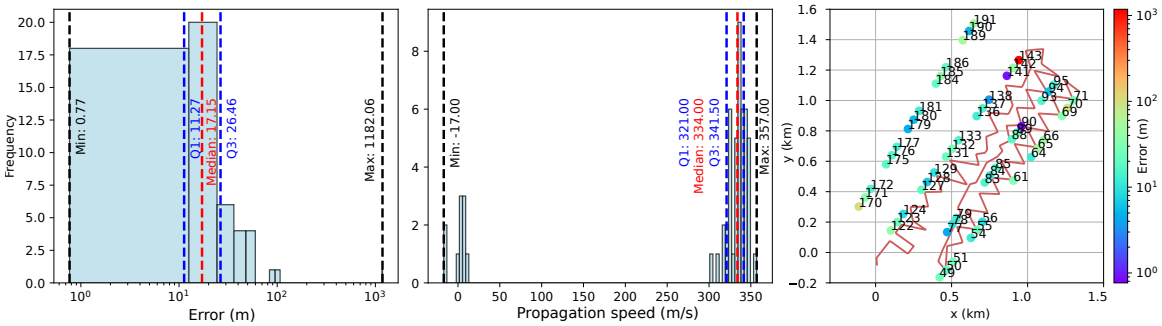

(a) Mode method results.

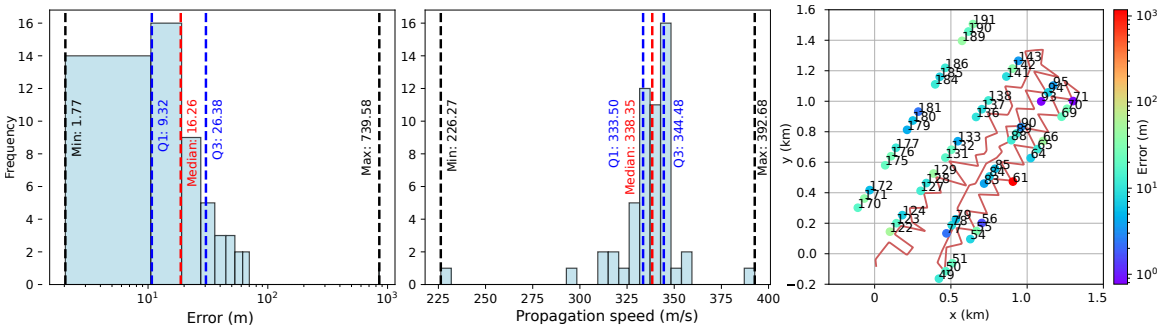

(b) Normalised cost function method results.

Fig. 5.9: Comparison between results from the mode method from [5] and the normalised cost function method. On the left, a histogram of error distribution for all 55 experiments is plotted, where the error is calculated as the Euclidean distance to the actual sources. In the middle, the propagation speed estimations for each method are plotted with different x-axis scales due to the presence of extreme outliers in the mode method. On the right, the distribution of errors for each experiment is displayed using a colourmap.

distribution and have comparable statistics. However, the proposed method in this thesis offers improved performance, as the normalised cost function does not require minimising $J(x, y, z, v)$ for all combinations of sorted channels, resulting in a faster execution time[5]. Fig. 5.9a shows the presence of a large amount of outliers obtained when using the mode method to estimate the propagation speed, a result of the independent manner in which each argument estimate is computed. It is important to note that this issue does not affect the estimates of the spatial coordinates (x, y) and only arises in 10 out of the 55 experiments. On the other hand, in Fig. 5.9b, since the propagation speeds are linked to the spatial coordinates by the minimisation of the normalised cost function for a given number of channels m, there are no extreme outliers near zero.

Notably, in the right-hand side plots of Fig. 5.9, although the overall distribution of errors is similar, two experiments stand out: Experiment 61 yields accurate results with the mode method but is an extreme outlier with the normalised cost function method. Conversely, Experiment 143 performs well with the normalised cost function method but is an outlier with the mode method. In Fig. 5.10, the TDOAs for these experiments are plotted alongside the differential distances to the actual sources. It can be observed that Experiment 143 has only a few TDOAs accurately estimated,

[5]In fact, later in this section, Fig. 5.11a shows that a median of $m = 37$ channels is used, and a quarter of the experiments achieve the minimum value of the normalised cost function at the arbitrarily selected starting point of $m = 34$ channels.

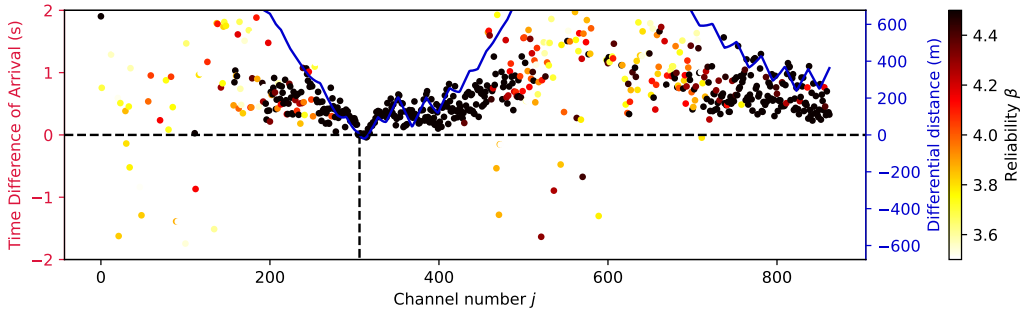

(a) Experiment 143.

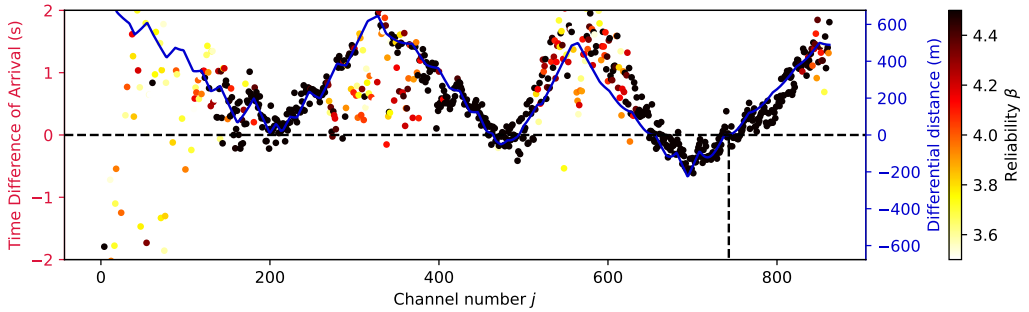

(b) Experiment 61.

Fig. 5.10: Time differences of arrival are shown scattered along the differential distance to the actual source locations for experiments 143 and 61, which are examples of extreme outliers and good estimations for the mode method and the normalised cost function methods, respectively. The reliability β for each channel is displayed using a colourmap.

mainly those near the reference channel. The remaining channels, despite their high reliability β, show scattered TDOA values with no clear trend. This dispersion explains why the normalised cost function method, which utilises fewer channels, performs better in this scenario.

In contrast, the TDOAs in experiment 61 display a clearer trend, although they still deviate from it, when compared, for instance, to experiment 190 in Fig. 5.5a. This deviation around the differential distance scaled by the propagation speed suggest that a higher number of channels should lead to a better estimation when applying triangulation. This is indeed the case, as the mode method, which uses all combined sorted combinations m does not yield an outlier for this experiment.

In order to illustrate that, generally, a low number of sorted channels is sufficient to obtain good estimates, Fig 5.11 compares the number of sorted channels m used in the normalised cost function method with those that yield the actual minimum error relative to the vibroseis locations. That is, for each source location, all source estimations from the respective combinations of sorted channels m are evaluated. The error from each estimation is compared non-blindly with the vibroseis locations, and the m values with the minimum errors are selected and plotted in the histogram in Fig 5.11b. On the other hand, Fig 5.11a shows the selection of sorted channels m using the proposed blind method, by minimising the normalised cost function. Although the statistics of both histograms differ, they both show that the majority of experiments cluster around a low number of sorted channels m, concluding that even by knowing the actual vibroseis source locations, a low m is generally sufficient for the best estimation.

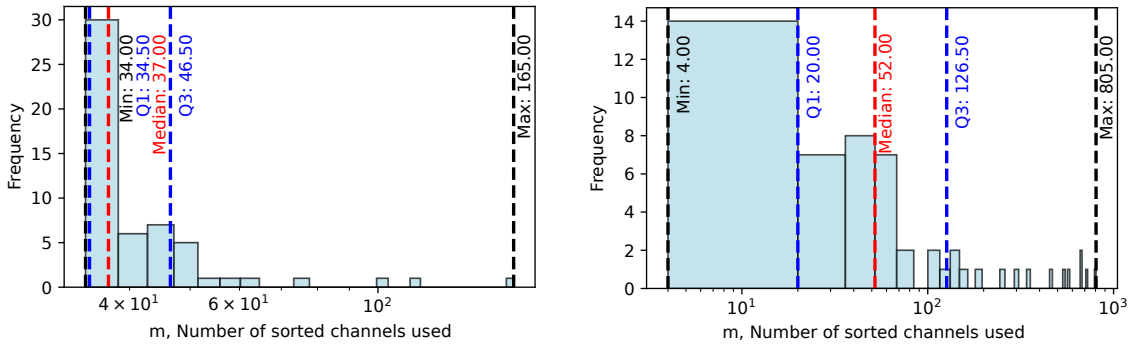

(a) Using normalised cost function method. **(b)** Using actual source locations as reference.

Fig. 5.11: Comparison of the number of sorted channels m used in the normalised cost function method with those yielding the minimum error to the actual source locations.

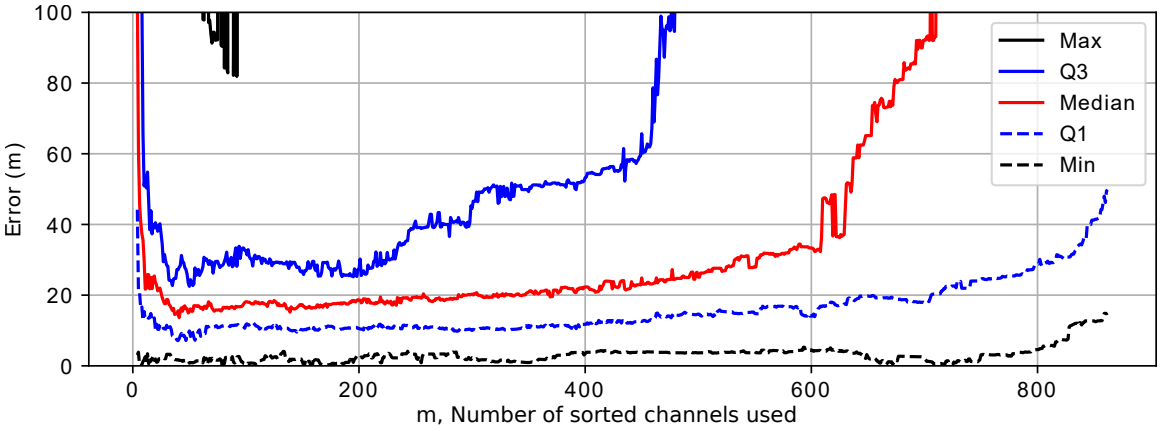

Fig. 5.12: Error statistics obtained for each combination of sorted channels m. A general trend is observed where the error statistics increases as m increases.

Furthermore, in Fig. 5.12, the maximum, third quartile (Q3), median, first quartile (Q1), and minimum errors are plotted against an increasing number of sorted channels used. It can be observed that these statistics increase as m increases, and around $m = 70$ channels, the minimal maximum outliers are approximately 80 metres, suggesting an optimal overall source estimation performance around this quantity of sorted channels m.

5.3 Acoustic imaging based on near-field beamforming

As an alternative to the triangulation method exposed in the previous section for single acoustic source location estimation, the application of delay-and-sum beamforming is evaluated here for acoustic imaging purposes using the same dataset. This method has the potential for estimating multiple simultaneous acoustic sources.

5.3.1 General considerations and assumptions

Some general considerations must be kept in mind when applying beamforming algorithms to distributed acoustic sensing data. In Chapter 3, Eq. (3.1.1) states that each sensor in an array forming an aperture samples the spatial field $f(\vec{x}, t)$, essentially obtaining a three-dimensional vector that thoroughly describes the particle displacement/velocity at a point in space. Three-component seismographs, for instance, are capable of measuring the directions of ground motions in three orthogonal spatial coordinates. Optical fibre-based sensors, however, measure the strain/strain rate of compression/extension, which is mostly noticeable longitudinally in the direction along the fibre for P-waves. This results in a directivity modelled by the squared cosine of the impinging angle of arrival, as illustrated in Fig. 4.10.

In [2], the application of MUSIC beamforming in a far-field scenario is evaluated using distributed acoustic sensing measurements from a natural earthquake. Such a study addresses a limitation of distributed acoustic sensing, where some channels are not properly aligned. Because strain/strain rate is measured along channels corresponding to the same fibre, the measurements of nearby channels are not completely independent (in addition to the fact that channels over-sampled under the gauge length are, by definition, correlated). The fibre either compresses or decompresses, which can cause channels to be in counter-phase due to the same acoustic wavefront. Applying beamforming directly to the DAS measurements results in a poorly estimated steered power response, possibly in part due to this limitation. To address this issue, the three-component seismographs co-located along the fibre are used as a reference to align the fibre measurements in a procedure referred to as *spatial integration*.

The approach for applying beamforming in this Thesis is a slight variation of the blind reliability channel sorting method from [5], which was used in the triangulation section. Eq. (5.1.4) defined the local similarity κ_{ij} between two channels using the absolute value of the phase cross-correlation function, and the argument of its maximum as the TDOA for use in triangulation. For delay-and-sum beamforming, it is better to remove the modulus to discard (or give a lower reliability score to) those channels that happen to be in counter-phase, either due to the intrinsic limitations of strain/strain rate measurements or by spatial wave properties. Therefore, the local similarity κ_{ij} is

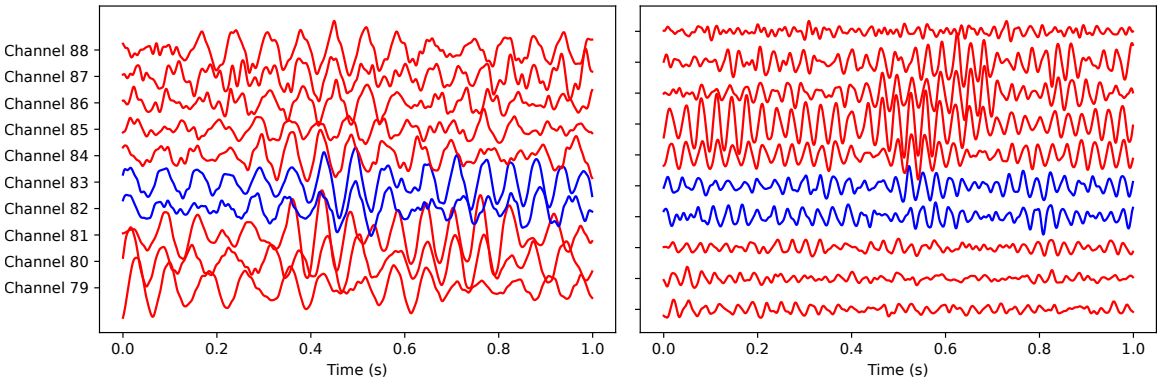

Fig. 5.13: The linear section of fibre corresponding to channels 79 to 88 for Experiment 181 is shown. Two one-second time intervals of data, taken at 2 seconds and 7 seconds after the start of the vibration, are displayed. These intervals are aligned to point toward the source, assuming its location is known. Channels 82 and 83, shown in blue, are selected using the reliability sorting method with β_i obtained from Eq. (5.3.1).

redefined in Eq. (5.3.1), where β_i is also highlighted, as it depends directly on the definition of κ_{ij}. Although its definition itself does not change, it is updated with the new κ_{ij}.

$$\kappa_{ij} = \frac{\max\left(\mathrm{PCCF}_{ij}\right)}{\mathrm{RMS}(W)} \qquad \beta_i = \sqrt{\frac{1}{M-1}\sum_{j=0}^{M-1}\kappa_{ij}^2}; \quad i \neq j. \tag{5.3.1}$$

Fig. 5.13 shows an example where, for experiment 181, the measurements from the channels corresponding to the eighth linear section of fibre are displayed. Data is delayed assuming the location of the source is known, with a constant speed of propagation of 342 m/s to scale the differential distances. Channels plotted in blue represent 2 out of the 50 best channels using the reliability values β_i obtained from Eq. (5.3.1). Two time intervals are plotted. In the first, channels 86 to 88 are observed to be in counter-phase relative to the two selected channels. Summing these channels as they are steered to the actual source would result in destructive interference, reducing the steered power response. In the second time interval, the two blue-selected channels still add in phase, exhibiting consistent behaviour, whereas the other channels show inconsistent behaviour between both time intervals. Ideally, we aim to sort the DAS measurements so that selecting the m best channels results in their summation producing more constructive than destructive interference throughout the entire time window when steering them to the acoustic source.

When employing uniform linear arrays for beamforming, the spatial Nyquist theorem must be satisfied to prevent spatial aliasing, as introduced in Section 3.1.2. The sorting method typically yields sparsely scattered channels, and considering that the fibre is not uniformly distributed in a Cartesian grid, spatial aliasing is not necessarily restricted by the ten-metre separation between channels used due to the gauge length. A straightforward method to discern whether a high steered response power for a point in space (a potential estimation of a source location) is due to aliasing is to simulate the array in a controlled environment with a known source. If sources other than the simulated one are detected, the limitation can be attributed to the array's geometric properties, rather than to the distributed acoustic sensing limitations.

One final consideration is the assumption of a homogeneous medium: no distinction is made between the different propagation speeds in the terrain. This assumption is due to the lack of precise knowledge of the terrain characteristics and is a potential source of error.

5.3.2 Impact of sorted channel selection on near-field imaging

To illustrate the improvements from discarding unreliable DAS channels for near-field beamforming, Fig. 5.14 shows the differences in performance for experiments 180 and 141, selecting the 60 most reliable channels versus using all available DAS channels. For experiment 180 (Fig 5.14a), the sixty selected channels are well spread out along the fibre, yielding a larger aperture and better spatial resolution than in experiment 141 (Fig 5.14b), where the most reliable channels are close to each other and near the source, resulting in a smaller aperture and worse spatial resolution. This is evident in the range resolution, where patterns converging towards the centroid of the array are more noticeable when steering the array further away. A noticeable difference between the two experiments is that for experiment 180, a higher peak steered response power (P_{BF}) is obtained, leading to a higher contrast in the image (see colourmap scale), implying that the estimation is more reliable.

Fig. 5.14a serves as an example where, even with the minimum spacing between selected channels exceeding the Nyquist limit for linear spatial sampling, which is $d = \lambda/2 \approx 2$m for the highest frequency of 80Hz at a propagation speed of around 340m/s, no evident aliasing is perceived in the

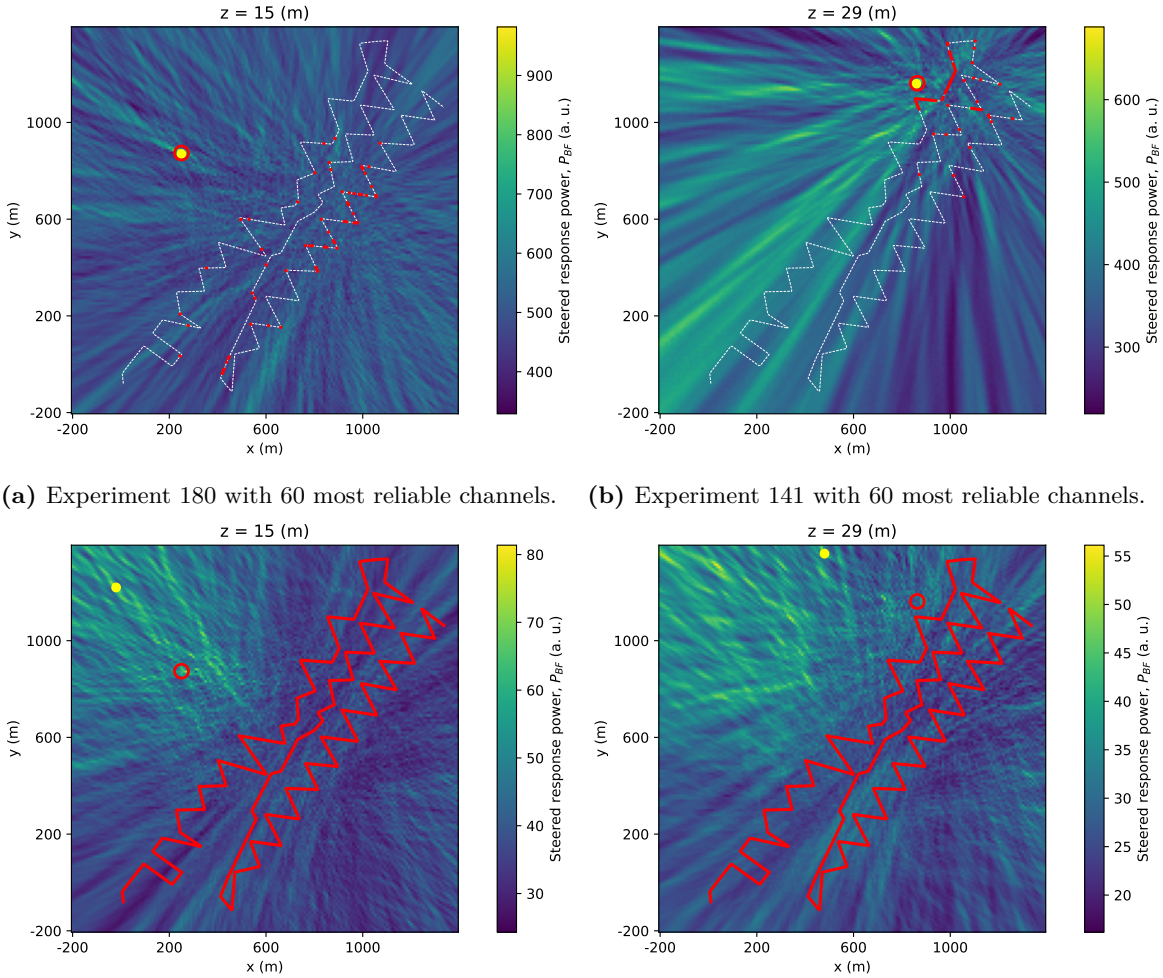

(a) Experiment 180 with 60 most reliable channels.

(b) Experiment 141 with 60 most reliable channels.

(c) Experiment 180 with all available channels.

(d) Experiment 141 with all available channels.

Fig. 5.14: Delay-and-sum beamforming applied to sources 180 and 141, with the actual sources depicted as red circumferences. The top row shows the steered response using the 60 most reliable channels, while the bottom row shows the results using all 863 available DAS channels (red dots). The yellow circles indicate the pixel where the maximum P_{BF} is found within the image.

image. There is a clear peak at two metres away from the actual documented vibroseis location. When calculating the co-array for this scenario, the minimum unique distances between elements of the co-array do not exceed 4 metres, with the minimum overall distance between its elements of 0.02 metres, and no noticeable aliasing is observed in the steered response.

The estimation errors for these examples are 2m and 4m for sources 180 and 141, respectively, when using a selection of the 60 best sorted channels, demonstrating good performance for these cases. However, when applying delay-and-sum beamforming using all available channels, it is evident in Fig. 5.14c and Fig. 5.14d that the source of vibration is not estimated correctly. The estimation errors increase significantly to 440m and 431m for sources 180 and 141, respectively, when selecting the peak steered response power with all available DAS channels. Only a general trend indicating that the source is somewhere to the north-west of the fibre can be extracted from these images.

These examples clearly illustrate where the channel sorting approach is useful for near-field imaging applied to DAS measurements, with the objective of source location estimation. In the subsequent sections, problems that arise and make the results less robust are discussed, along with a general statistical analysis for all 55 experiments. These issues must be taken into consideration when analysing imaging results from near-field beamforming.

5.3.3 Depth resolution

Imaging results in Fig. 5.14 are presented at a constant z coordinate, despite the fibre coordinates lying on terrain with variable heights. These variations are, however, negligible compared to the array's extension in the x-y plane, as illustrated by Fig. 5.1 at the beginning of the chapter. To illustrate why the choice is made not to scan at variable z depths, Fig. 5.15 shows the results of

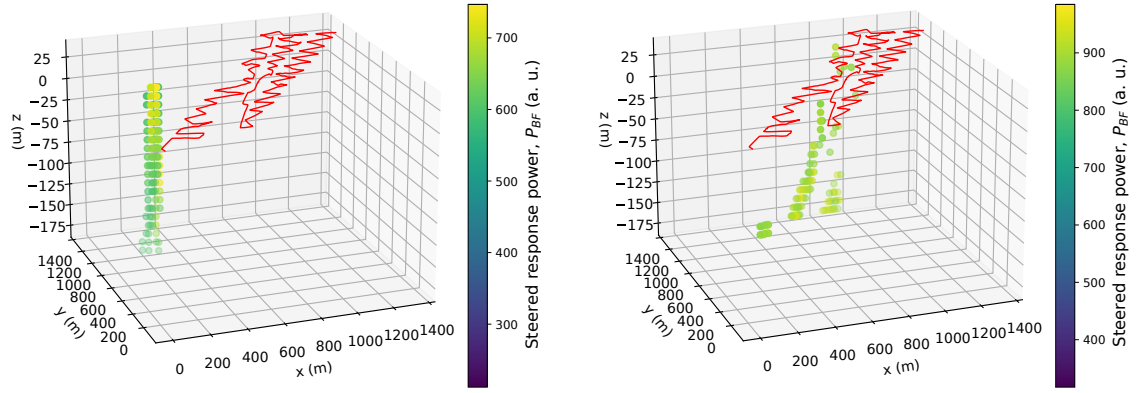

(a) Experiment 180 with 60 most reliable channels. **(b)** Experiment 141 with 60 most reliable channels.

Fig. 5.15: Imaging applied to experiments 180 and 141 on a Cartesian grid with 10-metre spacing in each coordinate. A threshold is applied to display in three dimensions only the coordinates with the highest steered response power.

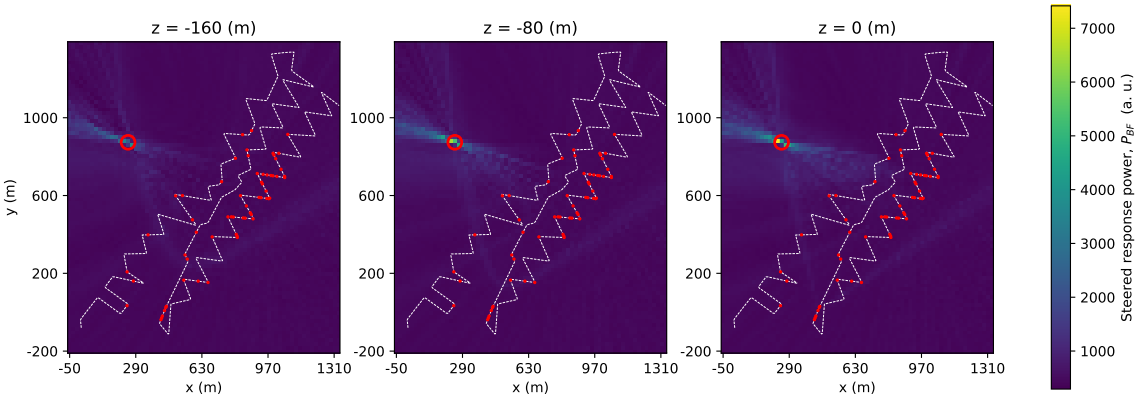

Fig. 5.16: Simulation of a chirped source at location 180, $z = 15$ m, using the 60 most reliable channels. The low depth resolution can be attributed to the limited spatial extension of the array in the z direction.

applying delay-and-sum beamforming on a Cartesian grid with 10-metre spacing in each coordinate, including z, for experiments 180 and 141. The steered response around the source in three dimensions is displayed by applying a threshold to show only the coordinates with the highest steered response power. For experiment 180 (Fig. 5.15a), it is observed that low resolution is achieved in z, with high steered response powers observed down to -150 metres at around the same position in x-y. A similar situation is seen in experiment 141 (Fig. 5.15b); however, here, coordinates with high estimated P_{BF} are not precisely distributed around a constant x-y position and scatter as depth increases, possibly due to the low resolution in x-y resulting from the limited aperture yielded by the selected channels, as discussed for Fig. 5.14b. Without considering the geometric limitations of the array, such as its low depth extension, it may appear that the high P_{BF} plotted points represent scatterers at various depths in the terrain, indicating actual sources of acoustic emission at those depths. To discard this notion and confirm that these are attributable to array resolution limitations, a source is simulated in a homogeneous environment at the same location as the vibroseis location in experiment 180. The results from this simulation are shown in Fig. 5.16, where steering the array down to -80 metres yields a high steered response power, even though the only simulated source is at $z = 15$ metres and no scatterers are present in the homogeneous simulated medium.

The intrinsic limitation due to the low depth extension of the fibre implies that it is not worthwhile to steer the array at variable depths to generate a three-dimensional image, adding computational cost without much gain in information. As depth estimations do not provide valuable information for source estimation, imaging is performed on a fixed z plane for each experiment, corresponding to the actual z coordinate of the source location. The choice of assigning the z coordinate to that of the source is to isolate estimation errors to the x-y scanning plane. However, for a complete blind approach, and given the low spread of sources in z, choosing a fixed z for scanning at the vertical centroid of the fibre would yield equivalent results.

5.3.4 Speed propagation dependence

An accurate direction of arrival or source location estimation requires precise knowledge of the speed of propagation in the medium. Conversely, accurate speed of propagation estimation requires precise knowledge of the source location [6]. This is particularly noticeable in linear arrays for far-field estimation, where a completely ambiguous continuum of possible pairs of speed and direction

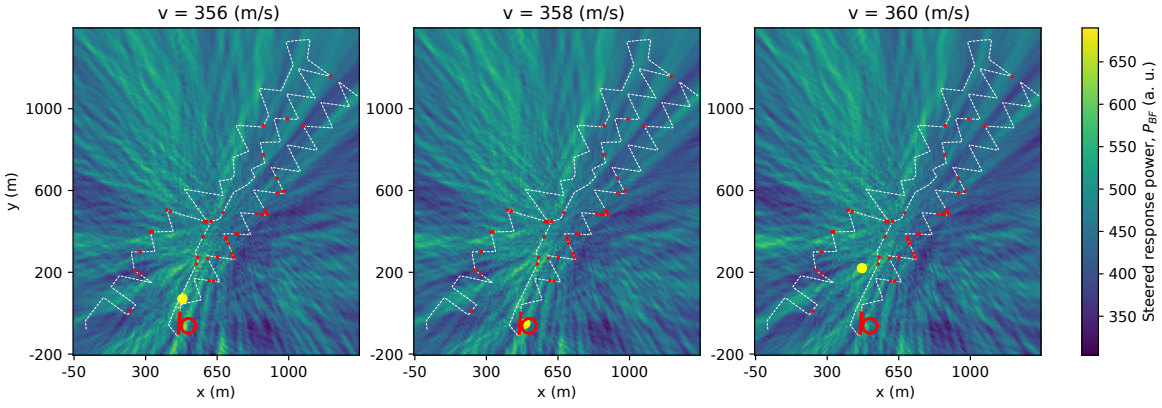

Fig. 5.17: Steered response for experiment 51 with the 50 most reliable channels, yielding an accurate source estimation for $v = 358$ m/s. Variations in the employed speed of propagation significantly alter the source estimation result.

of arrival occurs [2].

In this work, source estimation for imaging is carried out in a manner similar to the triangulation method. An unknown but homogeneous speed of propagation is assumed, and the final source estimation is the one that yields the highest steered response power within a grid of coordinates (x, y) and speeds of propagation v. Fig. 5.17 shows an example of imaging the acoustic field with different speeds of propagation for experiment 51. Even though the highest steered response power is obtained near the actual source location at a propagation speed of $v = 358$ m/s, slight variations in the speed of propagation of 2m/s cause significant changes in the source estimation. Note that although the estimated propagation speed (i.e., the speed that yields the highest steered response power) of $v = 358$ m/s differs from the median speed estimated using triangulation in Fig. 5.9, it remains within the range of propagation speeds reported for the terrain in [29]. Furthermore, as will be shown later in this section in Fig. 5.23, the estimated propagation speeds tend to cluster depending on the location of the vibroseis truck when the vibration is emitted.

5.3.5 Directional response

A brief analysis of the impact of theoretical fibre directivity is carried out by first estimating the direction of the fibre at each channel. To do this, the fibre coordinates are interpolated using cubic splines to obtain smooth, differentiable curves at each channel. The unit vectors describing the estimated direction of the fibre at several points along it are plotted in blue in Fig. 5.18.

In an effort to assess whether there is a noticeable qualitative correlation between the sorting yielded by the reliability method, Fig 5.19 shows the data for experiment 180. In this figure, 100 channels are selected using the reliability sorting method on the left, and sorted by the theoretical directivity to the known source location on the right, where the highest directivity is achieved when the gradient unit vector points directly towards the source. However, no significant relationship between both plots can be established, except that in both cases, the section of fibre where an unwanted disturbance is measured, around channels 50 and 350, is discarded. It is also important to note that P waves are not surface waves, and the fibre is not measuring the direct path to the actual source, which explains why all normalised channels show a perceivable strain rate in the 6-10 second time window, even with low theoretical directivity in a direct path to the source.

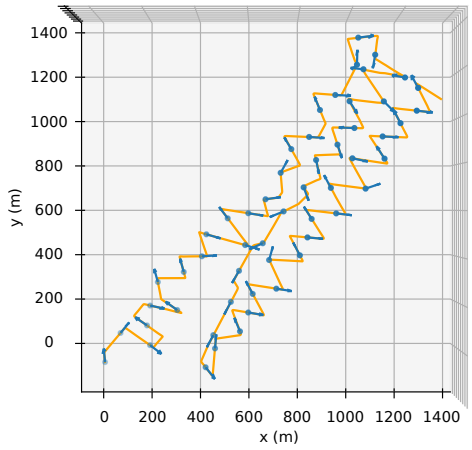

Fig. 5.18: Unitary vectors representing the orientation of the fibre are plotted in blue, along with a cubic spline interpolation of the fibre in yellow.

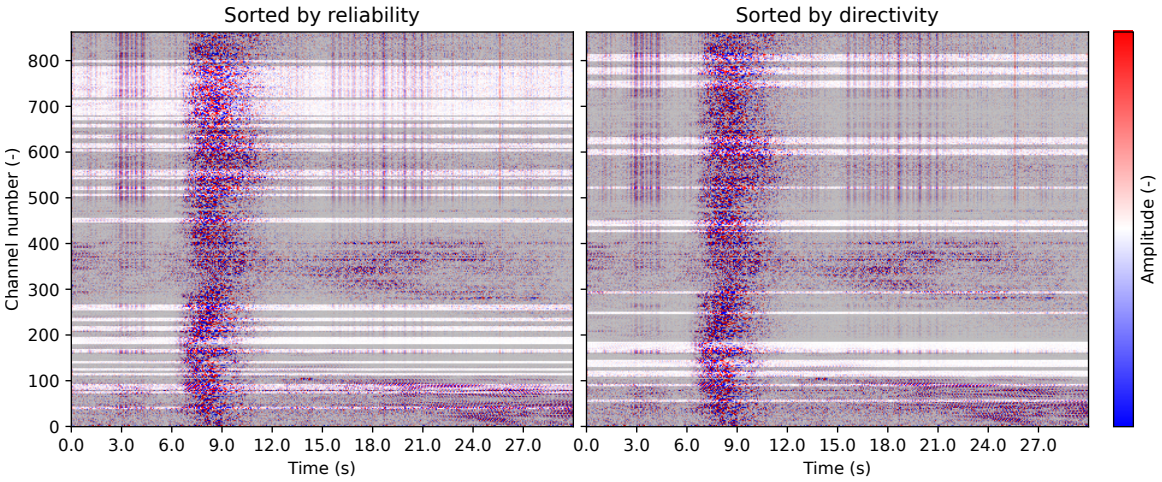

Fig. 5.19: Data captured for source 180 is masked to highlight the 100 most reliable channels (left) using the reliability sorting method, and the 100 most directive channels to the source in a direct path (right).

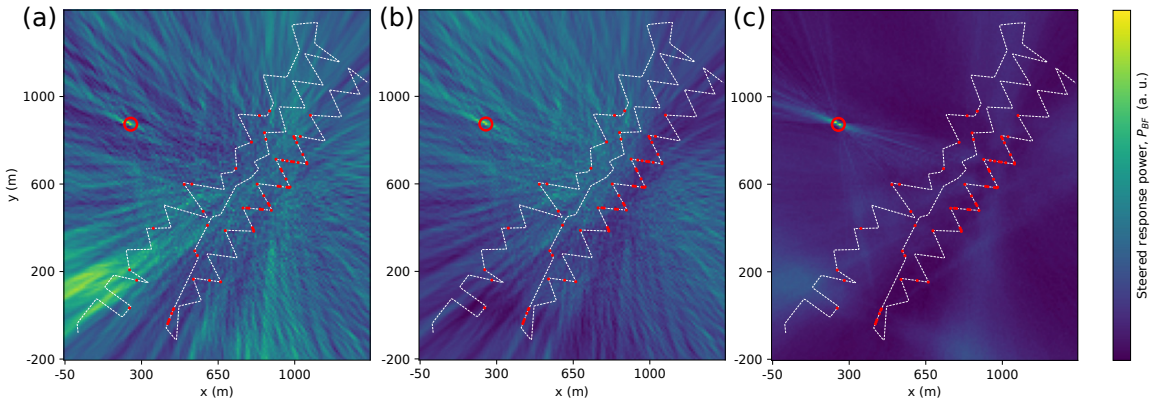

Fig. 5.20: Imaging results of experiment 180 for beamforming with adaptive weighting based on fibre orientation: (a) with normalisation, (b) without normalisation, and (c) a simulation with normalisation.

When applying delay-and-sum beamforming directly, each weight w_m is usually unitary, and a normalisation is applied to compensate for the difference in the number of channels M used (see Eq. (5.3.2)). To incorporate the estimated orientations of the fibre, Eq. (5.3.3) suggests an alternative that increases the weighting of the channels m that would theoretically have better directivity when steering the array to each of the coordinates (x, y, z) that generate the image. A normalisation is applied such that the sum of all weights is 1, consistent with the normalisation weighting of $w_m = 1/M$ for conventional beamforming [35].

$$z(t) = \sum_{m=0}^{M-1} w_m y_m(t - \Delta_m) \qquad \text{s.t.} \sum_{m=0}^{M-1} w_m = 1 \qquad \Longrightarrow \qquad w_m = \frac{1}{M} \tag{5.3.2}$$

$$z(t) = \sum_{m=0}^{M-1} \cos\theta_m y_m(t - \Delta_m) \qquad \text{s.t.} \sum_{m=0}^{M-1} \cos\theta_m = 1 \tag{5.3.3}$$

Fig. 5.20a shows the results of applying the directivity-dependent weighting approach to the measurements from source 180, with the normalisation proposed in Eq. (5.3.3). A slight increase in contrast around the source is observed, but areas without a source also yield a high steered response power. Comparing this with Fig. 5.20b, where no normalisation is applied, the same areas present low powers, indicating that the majority of the channels have low theoretical directivity towards these sections. A simulation in a homogeneous medium with additive white Gaussian noise is shown in Fig. 5.20c, which depicts the same pattern. Therefore, this approach is ill-suited for improving performance in source estimation and only provides information on sections of the image where comparatively lower directivity is achieved, indicating a less reliable steered response estimation.

5.3.6 General results

Finally, to obtain a near-field source estimation for all 55 sources, the following methodology is followed. First, a grid of 40 possible propagation speeds, ranging from 320 m/s to 359 m/s, is

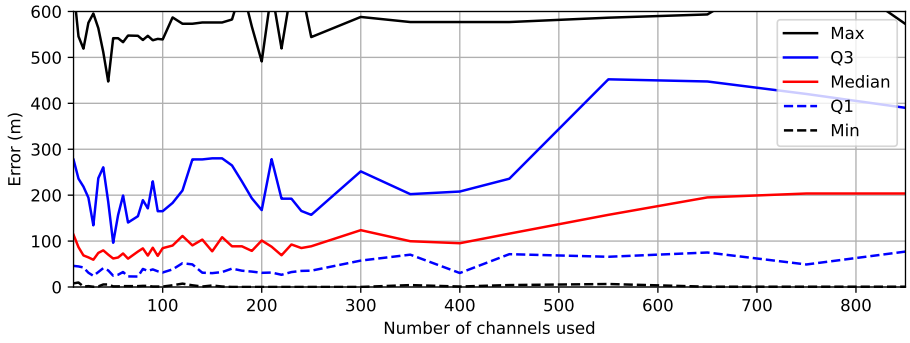

(a) Error statistics obtained for ascending use of sorted channels m.

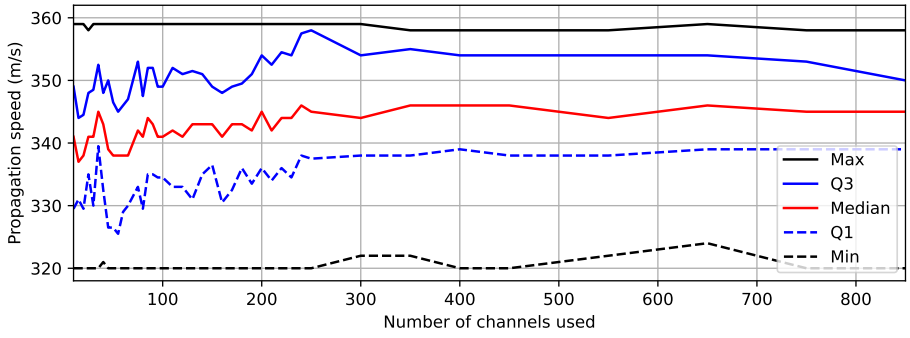

(b) Speed statistics obtained for ascending use of sorted channels m.

Fig. 5.21: Error and speed statistics for ascending use of sorted channels m using the reliability vector β as defined in Eq. (5.3.1).

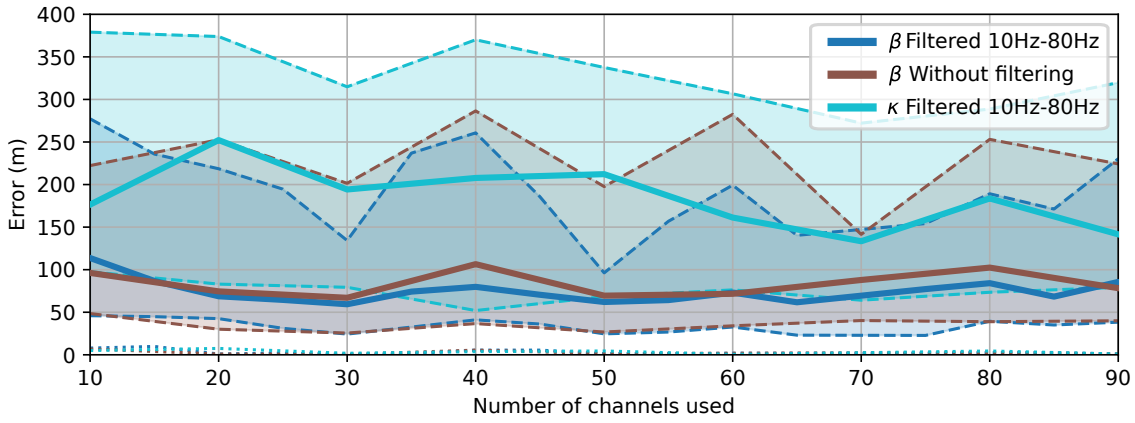

Fig. 5.22: A comparison between methods for channel sorting using the definitions from Eq. (5.3.1) is presented. The statistics for each method are plotted: continuous lines represent the medians, dashed lines show the first and third quartiles, and dotted lines indicate the minima. When sorting with κ, the reference channel is the one with the highest β value. The evaluation is performed in increasing steps of 5 channels for the dark blue case (β Filtered 10Hz-80Hz) and in increasing steps of 10 channels for the brown and turquoise cases.

evaluated using images with a 10 by 10 metre sampling grid on the $x-y$ plane, where z is at the centre height of the fibre. For each of these images, the maximum steered power is identified, and in the vicinity of this maximum, a new search is conducted on a 40 by 40 metre grid, with a 1 by 1 metre sampling. The source estimation is considered to be the one that yields the highest P_{BF} for all propagation speeds.

The error results, separated by quartiles, are shown in Fig. 5.21 as a function of the number of selected channels. It can be observed that the best overall estimations occur when using 50 channels, as indicated by the third quartile variations[6]. Beyond 50 channels, an increase in error statistics is observed as the number of channels used increases. This trend is similar to that seen when using triangulation for estimation with channels sorted by the κ similitude to a reference channel. When examining the variations in statistics from 10 to 100 channels, it is evident that the errors do not consistently increase with the number of channels. This suggests that some added channels do not improve the estimations. This could be due to the sorting method not being optimal for this application, including detrimental channels among the top 100; or new channels are added in locations where the path to the source follows terrain with a different average propagation speed, causing signals to not add constructively when delayed.

Several variations on the sorting method were tested for source estimation with the steered response. Among these, three relevant cases for up to 90 channels are shown in Fig. 5.22. These methods are: first, sorting by β from Eq. (5.3.1) using band-pass filtered data; second, evaluating error results with unfiltered data using the same sorting from the filtered case to isolate the beamforming improvements caused by filtering; and finally, sorting using κ also from Eq. (5.3.1), with the reference channel being the one with the highest β. The figure reads the same as Fig. 5.21, but the

[6]The third quartile is highlighted due to the more noticeable notch at this number of channels used. The choice of which statistic to observe when selecting the best case depends on whether we prefer an overall lower error for the highest number of experiments possible or whether we prioritise the best experiments yielding even lower errors, ignoring the worse experiments.

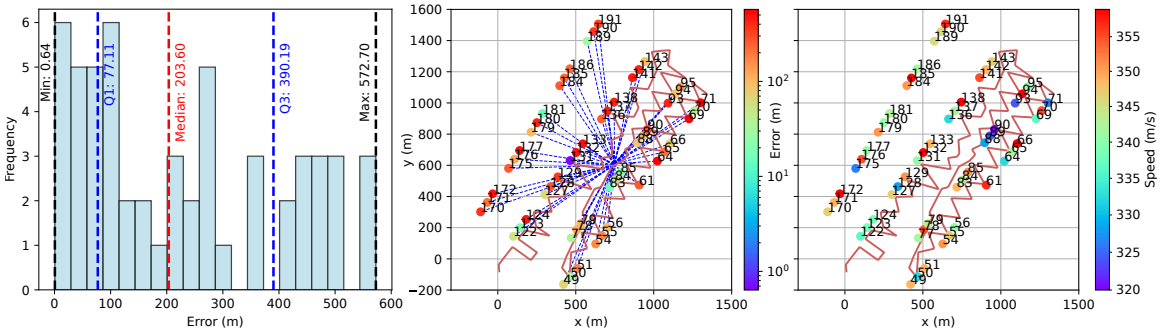

(a) Results using all channels.

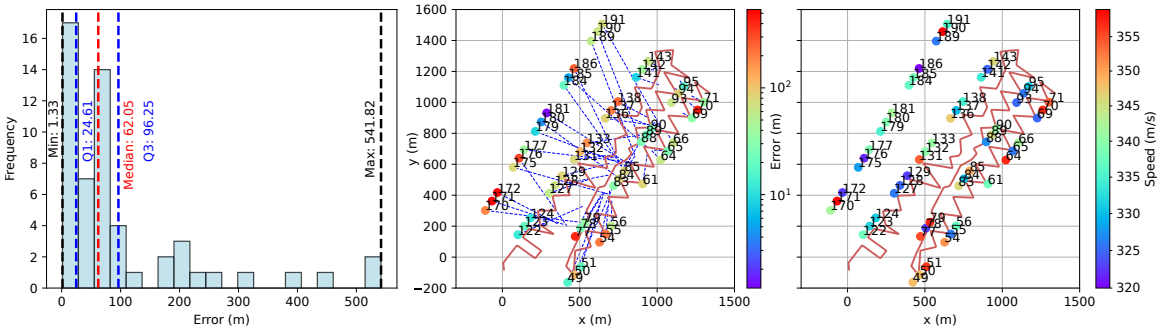

(b) Results using 50 most reliable channels based on β.

Fig. 5.23: Comparison of source estimation results using the steered power response with 50 channels and all channels. On the left, the histogram of errors to the actual sources is shown, indicating the minimum, first quartile (Q1), median, third quartile (Q3), and maximum values. In the middle, the distribution of errors for each source is displayed using a colourmap, with the dashed blue lines representing the distance to the centroid of the sub-array used. On the right, the propagation speeds obtained for each estimated source are shown.

statistics for each case are plotted with different colours. The medians are represented by continuous lines, the first and third quartiles by dashed lines, and the minima by dotted lines. Among all variations of the reliability score used for the sorting method, the best results are obtained when using β as redefined in Eq. (5.3.1) from the respective κ definition, with band-pass filtered data performing better both in the median and third quartile compared to the unfiltered case. Sorting the channels using the κ similitude between each channel and a reference, which is the sorting method used for triangulation, yields noticeably worse results, with a median error never below 100 metres. Among other sorting alternatives tested but not shown in the figure, the three methods are: using the normalised cross-correlation function instead of the phase cross-correlation function; using κ with the absolute value of the peak correlation to obtain β, even though it is conceptually inappropriate for delay-and-sum beamforming; and using κ without dividing by the RMS of the vicinity of the correlation peak. None of these methods performed better.

To discard spatial aliasing as a source of error in the results, a simulation was performed for the same combinations of channels yielded by the channel sorting method, and with the same source locations. The simulations did not show perceptible aliasing, so intrinsic geometric array limitations can be discarded as a source of error.

A comparison between the overall results when using the 50 most reliable channels and all channels is shown in Fig. 5.23. Although there are exceptions, such as sources 131 and 77, the error statistics generally demonstrate that the sorting strategy for blindly improving beamforming on DAS data is effective. The propagation speed estimations on the right are clustered for well-estimated sources, such as triplets 179, 180, 181 and 122, 123, 124. These variations confirm the local variations in the terrain properties suggested in the PoroTomo study [29].

To illustrate what the error results mean in context, Fig. 5.24 shows four examples with errors near the median using the 50 most reliable channels. For these cases, when the source is close to the fibre, as shown in Fig. 5.24a and Fig. 5.24b, the most reliable channels also tend to be the closest to the source, forming a cluster around it. This causes a loss in resolution as the aperture is not extended along all available channels. In the two examples in Fig. 5.24c and Fig. 5.24d, where the source is far from the fibre, a more scattered selection of channels is yielded, resulting in a better resolution for the image. These trends are also evident in Fig. 5.14 for two of the best cases, with errors of 2 m and 5 m for sources 180 and 141, respectively.

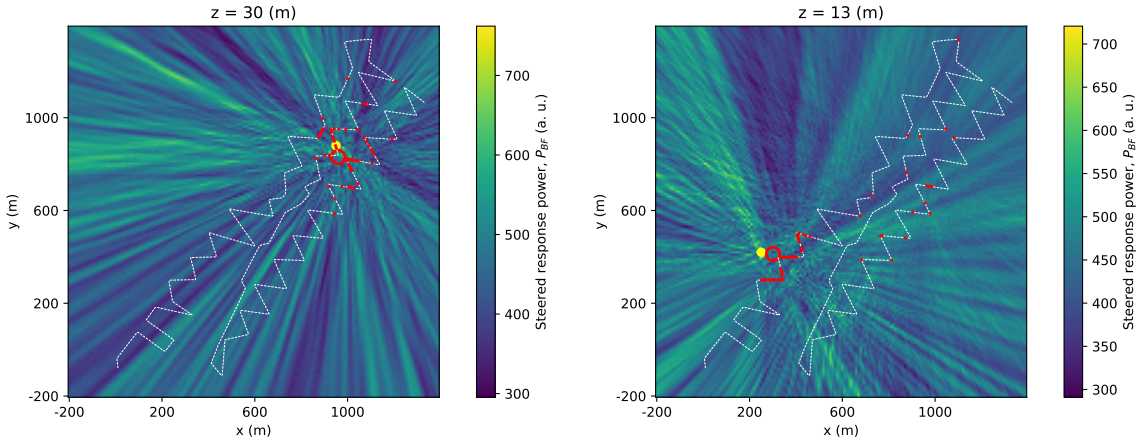

(a) Source 90, $v = 338$ m/s, error= 51 m.

(b) Source 127, $v = 326$ m/s, error= 52 m.

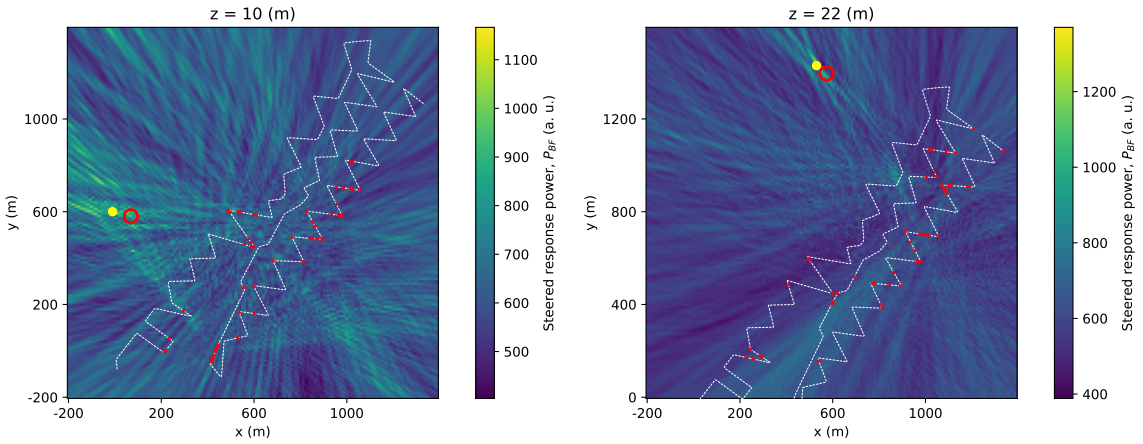

(c) Source 175, $v = 328$ m/s, error= 76 m.

(d) Source 189, $v = 326$ m/s, error= 56 m.

Fig. 5.24: Imaging examples where the error is around the median for all experiments using the 50 most reliable channels.

5.4 Acoustic imaging based on far-field beamforming

While the PoroTomo study is taking place, an earthquake occurs approximately 157 km south-west from the fibre deployment. This earthquake is measured by the DAS interrogator and allows for a far-field evaluation of the channel sorting method in a real scenario.

Given the large distance of the earthquake's epicentre from the fibre, it is possible to clearly separate the arrival of P-waves from S-waves, as depicted in Fig. 5.25, where a nine-second time window is selected for each case to separate the analysis. In this figure, data is shown both unfiltered and filtered with a band-pass filter in the range of 0.5-2Hz, assuming a general knowledge of the frequency range of seismic waves produced by earthquakes, following [2].

The analysis will consist of comparing Direction of Arrival (DOA) estimations when using variations of the reliability vector β for channel selection. These variations specifically involve changes in the inter-channel similitude κ, achieved by altering the type of cross-correlation used and considering whether the RMS of the peak correlation's vicinity is taken into account. A search for the maximum steered response power is conducted between 100m/s and 6000m/s, with intervals of 20m/s, and across all 360 degrees in azimuth, with intervals of 1 degree.

Fig. 5.26 shows the results of far-field beamforming applied between 200m/s and 6000m/s using all channels as a baseline for comparison with imaging using fewer channels. The red dashed lines indicate the direction of the earthquake relative to the fibre, obtained using an equirectangular projection of the latitude and longitude coordinates of the earthquake's epicentre. It is observed that both P and S wave analyses give an estimated direction of arrival of around 320º, with an actual direction of the earthquake at 290º. While the correct quadrant is estimated, there is still a 30º error, which we aim to improve using the reliability sorting method. Additionally, the propagation speed resolution is vague, with high steered response power obtained in a 1000m/s range, at around 1200m/s. Despite low propagation speed resolution, the S-wave beam consistently appears at lower velocities compared to the P-wave beam, which is expected since P waves travel faster than S waves.

To assess whether the sorted-channel selection method helps yield better estimations of directions

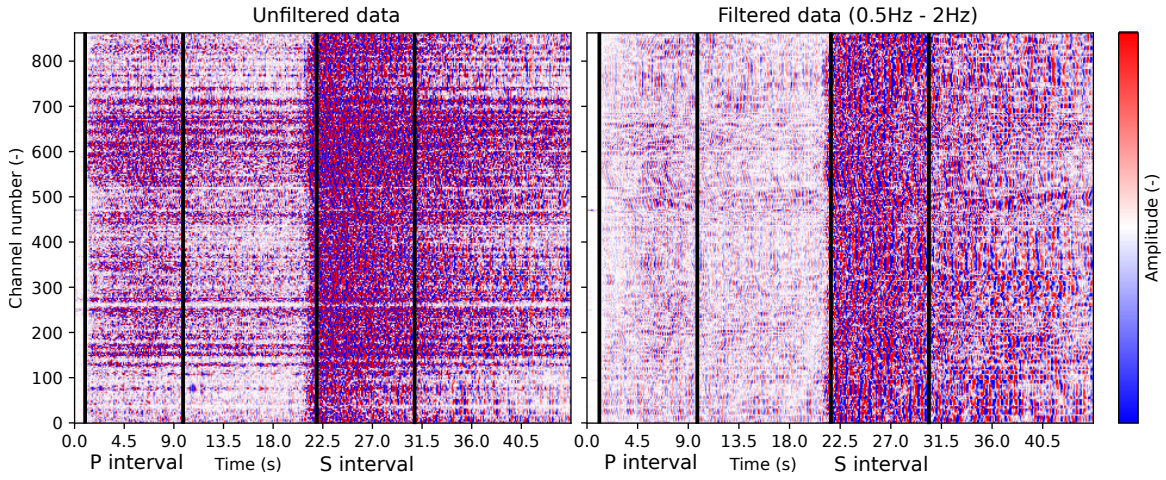

Fig. 5.25: Hawthorne earthquake captured by PoroTomo optical fibre. P-wave analysis uses 1-10 second intervals, and S-wave analysis uses 22-31 second intervals, with band-pass filtering between 0.5 and 2 Hz.

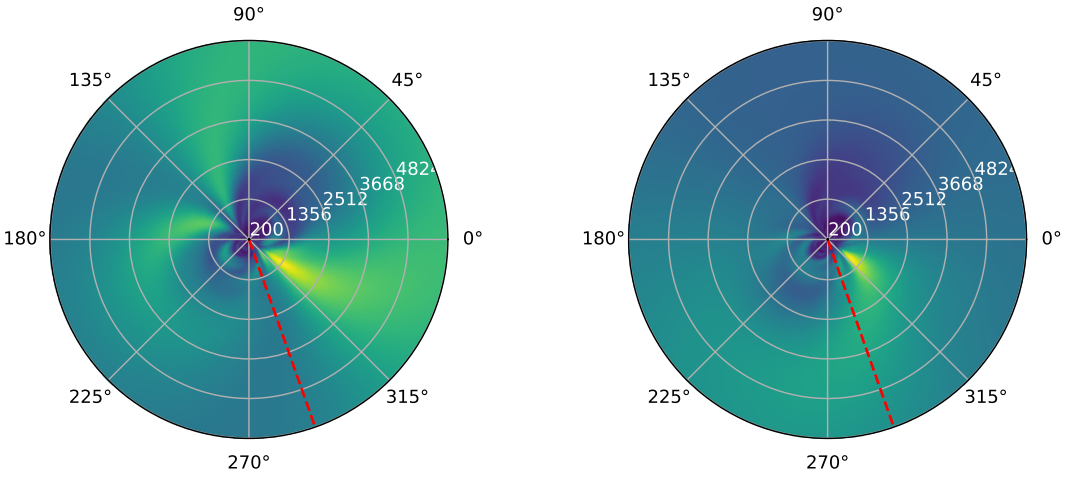

(a) P-wave steered response.

(b) S-wave steered response.

Fig. 5.26: Far-field imaging using all channels for time windows corresponding to P and S waves. The red dashed line indicates the actual direction of the earthquake relative to the fibre.

of arrival in far-field imaging based on delay-and-sum beamforming, as it did for near-field imaging, an extensive scan is conducted for sorted combinations of channels from 10 to 850 in steps of 10. This is done within a range of propagation speeds between 200 m/s and 6000 m/s, and for 360 angles of arrival at steps of 1°. The angle where the peak steered response is registered is stored, together with the respective speed of propagation and peak P_{BF} value. These results are displayed in Fig. 5.27 and Fig. 5.29, using different sorting vectors β derived from four variations of the definition of κ. These variations are $\kappa = \max(\text{NCCF})$, $\kappa = \max(\text{NCCF})/\text{RMS}(W)$, $\kappa = \max(\text{PCCF})$, and $\kappa = \max(\text{PCCF})/\text{RMS}(W)$, depicted by the colours blue, orange, green, and red respectively in the figures, where W is an arbitrary window around the correlation peak. NCCF stands for the normalised cross-correlation function (meaning the NCCF of two identical signals is unitary at $\tau = 0$), and PCCF stands for the phase cross-correlation function, as defined in Eq. (5.1.3). Additionally, Fig. 5.28 and Fig. 5.30 show the four respective images for each sorting variation at an arbitrary number of 100 selected channels, illustrating the contrast and perceptible resolutions of each case, since these aspects cannot be observed solely from the DOA estimation obtained from the peak P_{BF}.

By observing the P_{BF} peaks obtained in Fig. 5.27 and Fig. 5.29, in both the P-wave and S-wave scenarios, it is noted that the κ definitions consisting of only the peaks of each correlation yield higher P_{BF} values. The definition of κ, which involves dividing by the RMS of the vicinity, was originally proposed in [5] for the analysis of wide-band signals, specifically the 5-80Hz chirped signal generated by the vibroseis truck in the near-field scenario. This approach aims to eliminate ambiguities where multiple peaks appear in the cross-correlation function, often caused by distinct reflections. In a narrow-band scenario, periodicities in the cross-correlation functions are expected, making the division by the RMS of the vicinity unsuitable for this application. For P-waves, as shown in Fig. 5.27 (also observable in Fig. 5.28), dividing κ by the RMS of the vicinity produces similar results regardless of the type of cross-correlation function employed. In contrast, for the S-wave scenario, there is no clear trend, and neither sorting method significantly improves the direction of arrival estimation. While it may seem that the orange curves manage to identify a steered response peak near the red dashed line denoting the actual earthquake direction, Fig. 5.30b shows significant ambiguities in locating the peak, with low resolution.

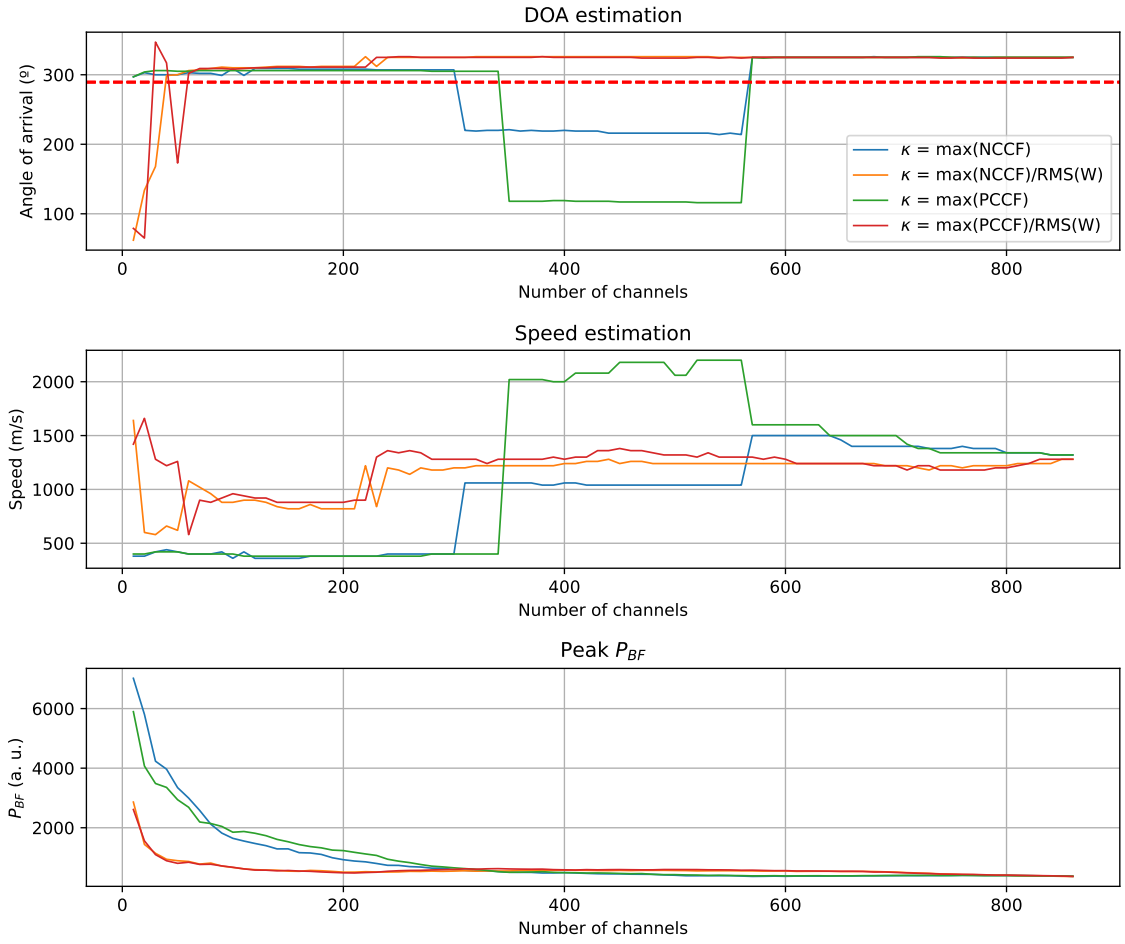

Fig. 5.27: Direction of arrival estimation results for the P-wave interval by channel sorting with β from four different κ definitions.

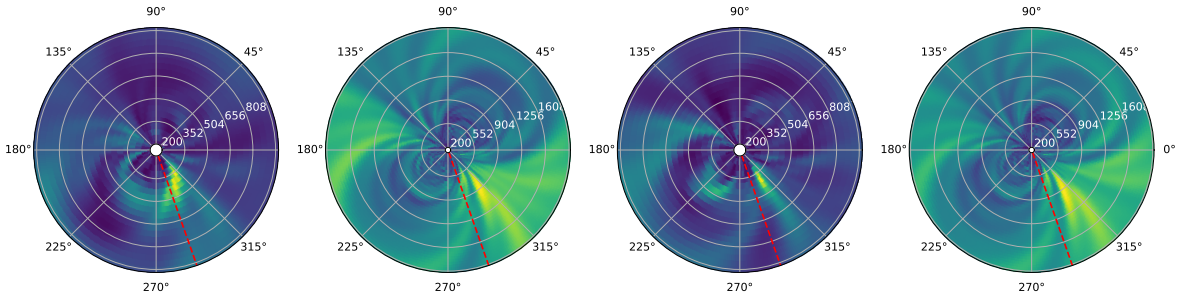

(a) **(b)** **(c)** **(d)**

Fig. 5.28: P-wave beamforming results for the 100 most reliable channels using varying definitions of κ: (a) max(NCCF), (b) max(NCCF)/RMS(W), (c) max(PCCF), and (d) max(PCCF)/RMS(W).

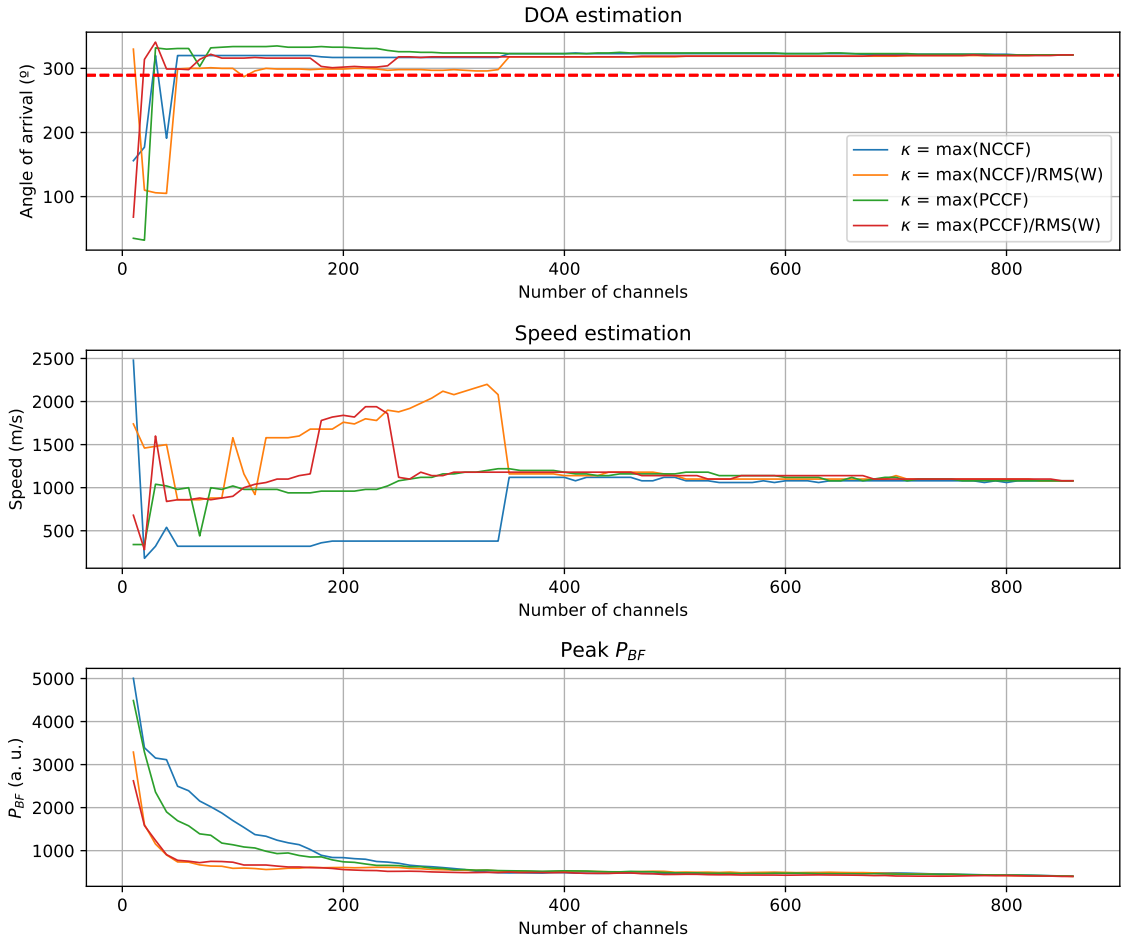

Fig. 5.29: Direction of arrival estimation results for the S-wave interval by channel sorting with β from four different κ definitions.

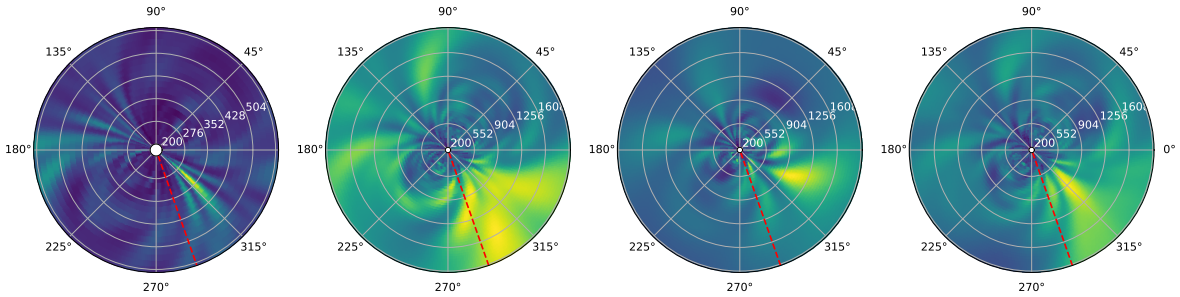

(a) **(b)** **(c)** **(d)**

Fig. 5.30: S-wave beamforming results for the 100 most reliable channels using varying definitions of κ: (a) max(NCCF), (b) max(NCCF)/RMS(W), (c) max(PCCF), and (d) max(PCCF)/RMS(W).

Turning to the P-wave results, when both sorting methods employ the definition of κ based solely on the maximum of their respective cross-correlations, it is observed that propagation speeds around 370 m/s are estimated when selecting the top sorted channels. These estimations also provide more stable results for the top sorted channels, closer to the actual earthquake direction, compared to methods where κ is defined by dividing over the RMS of the peak's vicinity. The propagation speed of 370 m/s is consistent with the seismic wave speed in the terrain surrounding the optical fibre reported in the PoroTomo study [29], and, although not exactly identical, it closely matches the range of propagation speeds estimated for vibroseis sources in the near-field scenario (Fig. 5.23b). In particular, Fig. 5.28a and Fig. 5.28c exhibit clearer contrasts in the estimations, favouring propagation speeds around 370 m/s and improving direction estimation from an error of 30^{o} when using all channels to around 10^{o} with a selection of the top sorted channels. This may indicate a local reflection that is more prominent in a few selected channels identified as the most reliable when using definitions of κ that do not divide over the RMS of the peak correlation vicinity.

In contrast, when examining the S-wave results, no improvement is evident in either case, as the peak P_{BF} is not found in a clear trend for either sorting method. The challenge in analysing S-wave results, also observed in S-waves generated by the vibroseis truck in the near-field (though not reported here), can be attributed to the more complex directivity response pattern associated with these waves. Due to the particle displacement being perpendicular to the wave propagation direction, the strain sensitivity depends on the angle between the fibre axis vectors and both the propagation vector and the polarisation vector [3]. Even when the polarisation is co-planar with the fibre axis vectors, the directivity pattern is represented by $\sin(2\theta)$, which can result in negative values. This characteristic can lead to polarity reversals that are even more unpredictable and detrimental compared to those in the P-wave scenario.

In conclusion, sorting vectors defined by κ using only the peak of their respective cross-correlations appear to yield better results for improving direction of arrival estimations in narrow-band scenarios for P-waves in the far-field. However, for S-waves, the channel sorting method does not work directly, as preprocessing of the measurements is necessary to address the variable and unpredictable perpendicular polarisations of S-waves relative to the direction of wave propagation.

5.5 Summary

An analysis of the DAS measurements from the PoroTomo study [29, 69, 8] is presented, focusing on strategies to enhance seismic source location estimations. Three main contributions are reported:

Firstly, building upon the work in [5], it is proposed to record the minimum value of the cost function minimised for estimating source seismic locations in the near field using hyperbolic triangulation and TDOA estimations. This minimum value is normalised by the number of channels used in each estimation, providing a way of selecting the subset of top sorted channels that generally yield equivalent or better results compared to using all channels and computing the mode of estimations. This approach significantly reduces computation time by avoiding the need to minimise the cost function across all channel combinations.

Secondly, a comprehensive evaluation of near-field imaging based on delay-and-sum beamforming is made, focusing on improving source estimation capabilities with wide-band sources. Although not explicitly reported in all cases, various channel sorting methods are explored to identify the most effective approach. As made explicit in Fig. 5.14 with two examples, and generally in Fig. 5.21a, using all available channels for acoustic (P-wave) imaging in the near field for seismic source estimation often yields ambiguous results that can be enhanced through sorted channel selection. Limitations are discussed and contrasted with array processing theory.

Thirdly, the channel sorting method is evaluated in the far-field in a narrow-band scenario, where the optimal sorting vector differs from that used in the near-field wide-band case. Angle of arrival estimation is improved with sorted channel selection for P-waves; however, for S-waves, the unpredictable polarisation introduces complexities that makes sorting method ill-suited.

Chapter 6

CONCLUSIONS

An exhaustive evaluation of the state-of-the-art channel sorting method was applied to both near field and far field data measured by the DAS deployment in the publicly available PoroTomo dataset. In the near field, both delay-and-sum beamforming imaging and hyperbolic triangulation were applied for seismic source location estimations. For the far field, a distant earthquake was evaluated using only beamforming imaging, as the Time Difference of Arrival obtained by the phase cross-correlation and a reference did not yield results applicable to triangulation.

For the channel sorting algorithm to work properly, there must be some degree of correlation between channels located across all sections of the optical fibre. In the PoroTomo deployment, with a maximum aperture of about 1.5 km, both the controlled vibroseis chirped sources and the distant earthquake at Hawthorne show minimal spatial dispersion of the mechanical wave between measurements at both ends of the fibre. This results generally in an even distribution of reliable channels. However, in datasets with larger fibre deployments relative to seismic wavelengths, special considerations are needed. Measurements from opposite ends of the fibre may not be highly correlated, while those from relatively close sections are. In these cases, the method should be adapted to consider the spatial location of each channel, applying the sorting method independently across sections. Then, the harmonic mean can be applied to the steered response of each section for a complete steered response estimation [76], though this reduces resolution due to the smaller aperture for each sub-array. Additionally, low correlation between distant channels makes hyperbolic triangulation inapplicable, as it depends on robust Time Difference of Arrival estimations. Deep learning methods that can reliably identify P-waves and S-waves TDOAs have been reported to address these issues as an alternative [77].

For near-field source estimation, it is assumed that the medium is homogeneous, and the direct path from each channel to each point in space is scaled by a constant propagation speed to map the time delays. Although this assumption is not accurate, both triangulation and delay-and-sum beamforming generally yielded accurate results, with some outliers. Triangulation is more robust to terrain inhomogeneities because it finds a linear fit that minimises a cost function without needing the TDOAs to match the distance scaled by the propagation speed exactly. Beamforming, however, is less robust to inhomogeneities, leading to more outliers and larger errors in the estimations. By knowing the terrain properties through prior inspection, it would be possible to account for variations in propagation speed along the path for time delay mapping. Another limitation of not knowing the propagation speeds precisely beforehand is the ambiguity in their estimation together with the directions of arrival, especially when the array does not have an extended aperture in all three spatial axes. A uniform linear array (ULA), for instance, extended along only one axis, maps the directions of arrival depending on the wavenumber, which is inversely proportional to the wavelength. The same perceived wavelength projected onto the ULA's axis can occur when a high-velocity wave arrives

almost perpendicularly ($\theta \to 90°$), which can be confused with a low-speed wavefront arriving close to parallel to the fibre ($\theta \to 0°$ or $\theta \to 180°$). Due to the low depth resolution of the employed fibre array, this ambiguity also exists, as the direct path would suggest that the P-waves are propagating on the surface (or even in the air), which is not the case. The estimated propagation speeds are thus inaccurate, as the P-waves travel a longer path below the surface, accounting for reflections. Therefore, the estimated speeds serve only as a lower bound. A fibre with an extended aperture in all directions must be used to correctly estimate propagation speeds from reflections below the surface.

Testing in both near-field and far-field scenarios shows that the way channels are sorted significantly affects beamforming performance. Slight changes in the sorting reliability definition proposed in [5], such as using the κ inter-channel similarity instead of the β global reliability score, can change the median error from about 50 metres to 200 metres. In the far-field scenario, the difference is notable when dividing the peak correlation by the RMS of the vicinity in the definition of κ, as this is a narrow-band case where periodic correlation peaks are more likely found. The variations in the sorting method yield estimates at different propagation speeds, suggesting that channels may be selected where reflections are measured with greater correlation.

For both near-field and far-field scenarios, band-pass Butterworth filtering is applied, assuming a general knowledge of the bandwidth of the seismic signals of interest. It was verified that only by band-pass filtering, both the TDOA errors decrease for triangulation, and the source location error statistics decrease for beamforming. A self-supervised deep-learning filtering approach using a U-Net specifically designed for DAS data [71] was tested but discarded because it negatively affected the reliability sorting method's performance due to artefacts between the time windows produced by the U-Net. Future work could focus on studying DAS data pre-processing for channel sorting and beamforming by evaluating performance in narrower frequency bands and addressing the artefacts caused by auto-encoder-based filtering. Despite these artefacts, this method shows promising results by filtering out interferences coexisting in the same frequency bands that cannot be filtered out by conventional band-pass filtering.

Finally, to study more concretely the effectiveness of the channel sorting method, a laboratory implementation could be used for controlled evaluation of the main limitations of DAS sensing, such as poor coupling, directive gain dependencies, and misalignment in the measurements of adjacent channels. These issues, reported in [2], are attributed to measuring strain/strain rate along one direction in the fibre instead of actual acoustic particle displacement/particle velocity.

REFERENCES

[1] G. P. Agrawal. *Fiber-optic communication systems*. John Wiley & Sons, 2012.

[2] M. P. A. van den Ende and J.-P. Ampuero. Evaluating seismic beamforming capabilities of distributed acoustic sensing arrays. *Solid Earth*, 12(4):915–934, 2021.

[3] S. P. Näsholm, K. Iranpour, A. Wuestefeld, B. D. E. Dando, A. F. Baird, and V. Oye. Array signal processing on distributed acoustic sensing data: Directivity effects in slowness space. *Journal of Geophysical Research: Solid Earth*, 127(2):e2021JB023587, 2022.

[4] A. H. Hartog. *An Introduction to Distributed Optical Fibre Sensors*. CRC Press, 1st edition, 2017.

[5] F. Muñoz and M. A. Soto. Enhancing fibre-optic distributed acoustic sensing capabilities with blind near-field array signal processing. *Nature Communications*, 13(1):4019, Jul 2022.

[6] D. H. Johnson and D. E. Dudgeon. *Array Signal Processing: Concepts and Techniques*. Simon & Schuster, Inc., USA, 1992.

[7] M. van den Ende, A. Ferrari, A. Sladen, and C. Richard. Deep deconvolution for traffic analysis with distributed acoustic sensing data. *IEEE Transactions on Intelligent Transportation Systems*, 24(3):2947–2962, 2022.

[8] K. Feigl, E. Reinisch, J. Patterson, S. Jreij, L. Parker, A. Nayak, X. Zeng, M. Cardiff, N. E. Lord, D. Fratta, C. Thurber, H. Wang, M. Robertson, T. Coleman, D. E. Miller, P. Spielman, J. Akerley, C. Kreemer, C. Morency, E. Matzel, W. Trainor-Guitton, N. Davatzes, and N. Taverna. PoroTomo natural laboratory horizontal and vertical distributed acoustic sensing data. `https://dx.doi.org/10.15121/1778858`, 03 2016. United States.

[9] P. Kearey, M. Brooks, and I. Hill. *An introduction to geophysical exploration; 3rd ed.* Wiley, Hoboken, NJ, 2009.

[10] W. A. Mousa. *Advanced digital signal processing of seismic data*. Cambridge University Press, United Kingdom, 2019. Publisher Copyright: © Wail A. Mousa 2019.

[11] H.-W. Zhou. *Practical Seismic Data Analysis*. Cambridge University Press, Cambridge, 2014.

[12] Wikimedia Commons. Spherical coordinate system. `https://en.wikipedia.org/wiki/Spherical_coordinate_system#/media/File:3D_Spherical_2.svg`, 2012. [Online; accessed 01-May-2023].

[13] L. E. Kinsler, A. R. Frey, A. B. Coppens, and J. V. Sanders. *Fundamentals Of Acoustics, 4th ed.* Wiley India Pvt. Limited, 2009.

[14] E. Kreyszig. *Introductory Functional Analysis with Applications*. Wiley Classics Library. Wiley, 1989.

[15] C. A. Balanis. *Antenna Theory: Analysis and Design*. John Wiley & Sons, second edition, 1997.

[16] G. S. Kino. *Acoustic Waves: Devices, Imaging, and Analog Signal Processing*. Prentice-Hall, 1987.

[17] G. Olivadoti. Sensing, analyzing, and acting in the first moments of an earthquake. *Analog Dialogue*, 35, January 2001.

[18] P. Dehlinger. Inside the earth, evidence from earthquakes: by bruce a. bolt, w. h. freeman and company, san francisco, 1982, xi + 191 pages. *Bulletin of the Seismological Society of America*, 74(2):791–791, 04 1984.

[19] R. E. Sheriff and L. P. Geldart. *Exploration Seismology*. Cambridge University Press, 1995.

[20] K. Zoeppritz. VIIb. Über Reflexion und Durchgang seismischer Wellen durch Unstetigkeitsflächen [VIIb. On reflection and transmission of seismic waves by surfaces of discontinuity]. *Nachrichten von der Königlichen Gesellschaft der Wissenschaften zu Göttingen, Mathematisch-physikalische Klasse*, pages 66–84, 1919.

[21] J. van Opstal. *The Auditory System and Human Sound-Localization Behavior*. Academic Press, San Diego, 2016.

[22] J. Benesty, J. Chen, and Y. Huang. *Microphone Array Signal Processing*, volume 1. Springer, 01 2008.

[23] R. Schmidt. Multiple emitter location and signal parameter estimation. *IEEE Transactions on Antennas and Propagation*, 34(3):276–280, 1986.

[24] B. Ristic, S. Arulampalam, and N. Gordon. *Beyond the Kalman filter: Particle filters for tracking applications*. Artech house, 2003.

[25] R. E. Kalman. A new approach to linear filtering and prediction problems. *Journal of basic Engineering*, 1960.

[26] J. G. Proakis and D. K. Manolakis. *Digital Signal Processing*. Prentice Hall, 4 edition, 2006.

[27] B. P. Lathi. *Signal Processing and Linear Systems*. Oxford series in electrical and computer engineering. Oxford University Press, 2010.

[28] A. Garg, A. Vos, N. Bortych, D. K. Gupta, and D. J. Verschuur. Spatial aliasing removal using deep learning super-resolution. *First Break*, 37(9):87–92, 2019.

[29] K. L. Feigl and L. M. Parker. Porotomo final technical report: poroelastic tomography by adjoint inverse modeling of data from seismology, geodesy, and hydrology. Technical report, Univ. of Wisconsin, Madison, WI (United States), 2019.

[30] R. T. Hoctor and S. A. Kassam. The unifying role of the coarray in aperture synthesis for coherent and incoherent imaging. *Proceedings of the IEEE*, 78(4):735–752, 1990.

[31] J. Serra. *Image Analysis and Mathematical Morphology*, volume 1. Academic Press, 1982.

[32] R. A. Haubrich. Array design. *Bulletin of the Seismological Society of America*, 58(3):977–991, 1968.

[33] V. Murino and A. Trucco. Three-dimensional image generation and processing in underwater acoustic vision. *Proceedings of the IEEE*, 88(12):1903–1948, 2000.

[34] Z.-Q. Wang and D. Wang. Mask weighted stft ratios for relative transfer function estimation and its application to robust asr. In *2018 IEEE International Conference on Acoustics, Speech and Signal Processing (ICASSP)*, pages 5619–5623. IEEE, 2018.

[35] R. G. Lorenz and S. P. Boyd. Robust minimum variance beamforming. *IEEE Transactions on Signal Processing*, 53(5):1684–1696, 2005.

[36] M. Palmese and A. Trucco. Three-dimensional acoustic imaging by chirp zeta transform digital beamforming. *IEEE Transactions on Instrumentation and Measurement*, 58(7):2080–2086, 2009.

[37] P. Vogel, A. Bartolini, and L. Benini. Efficient parallel beamforming for 3D ultrasound imaging. In *Proceedings of the 24th Edition of the Great Lakes Symposium on VLSI*, pages 175–180, 2014.

[38] M. Yang, R. Sampson, S. Wei, T. F. Wenisch, and C. Chakrabarti. Separable beamforming for 3-D medical ultrasound imaging. *IEEE Transactions on Signal Processing*, 63(2):279–290, 2014.

[39] H. B. Lim, N. T. T. Nhung, E.-P. Li, and N. D. Thang. Confocal microwave imaging for breast cancer detection: Delay-multiply-and-sum image reconstruction algorithm. *IEEE Transactions on Biomedical Engineering*, 55(6):1697–1704, 2008.

[40] G. Matrone, A. S. Savoia, G. Caliano, and G. Magenes. The delay multiply and sum beamforming algorithm in ultrasound b-mode medical imaging. *IEEE Transactions on Medical Imaging*, 34(4):940–949, 2014.

[41] X. Ma, C. Peng, J. Yuan, Q. Cheng, G. Xu, X. Wang, and P. L. Carson. Multiple delay and sum with enveloping beamforming algorithm for photoacoustic imaging. *IEEE Transactions on Medical Imaging*, 39(6):1812–1821, 2019.

[42] P. Ferdinand. The evolution of optical fiber sensors technologies during the 35 last years and their applications in structure health monitoring. In *EWSHM-7th European Workshop on Structural Health Monitoring*, pages 914–929. INRIA, 2014.

[43] T. Parker, S. Shatalin, and M. Farhadiroushan. Distributed acoustic sensing - a new tool for seismic applications. *First Break*, 32, 02 2014.

[44] Silixa Ltd, 230, Centennial Park, Elstree, Hertfordshire, WD6 3SN, UK. *iDAS™ intelligent Distributed Acoustic Sensor*, 2014.

[45] H. D. Young, R. A. Freedman, and A. L. Ford. *Sears and Zemansky's University Physics*, volume 2. Pearson Education, 2008.

[46] Lord Rayleigh. XXXIV. on the transmission of light through an atmosphere containing small particles in suspension, and on the origin of the blue of the sky. *The London, Edinburgh, and Dublin Philosophical Magazine and Journal of Science*, 47(287):375–384, 1899.

[47] D. J. Lockwood. Rayleigh and mie scattering. In *Encyclopedia of Color Science and Technology*, pages 1097–1107. Springer New York, New York, NY, 2016.

[48] J. Pastor Graells. *Chirped-Pulse Phase-Sensitive Optical Time Domain Reflectometry*. Doctoral thesis, Universidad de Alcalá, 2018.

[49] D. A. Krohn, T. MacDougall, and A. Mendez. *Fiber optic sensors: Fundamentals and applications: Fourth edition*. Spie Press Bellingham, WA, 01 2015.

[50] G. D. Peng. *Handbook of Optical Fibers*. Springer Nature Singapore, 2019.

[51] G. Mie. Beiträge zur optik trüber medien, speziell kolloidaler metallösungen. *Annalen der Physik*, 330(3):377–445, 1908.

[52] D. A. Long. The raman effect: A unified treatment of the theory of raman scattering by molecules. *The Raman Effect*, 2002.

[53] J. Schroeder, R. Mohr, P. B. Macedo, and C. J. Montrose. Rayleigh and brillouin scattering in k2o–sio2 glasses. *Journal of the American Ceramic Society*, 56(10):510–514, 1973.

[54] M. K. Barnoski and S. M. Jensen. Fiber waveguides: a novel technique for investigating attenuation characteristics. *Applied Optics*, 15(9):2112–2115, 1976.

[55] F. Muñoz Carmona. Blind near-field array signal processing to enhance fibre-optic distributed acoustic sensing capabilities. Master's thesis, Universidad Técnica Federico Santa María, Av. España 1680, Valparaíso, 2022.

[56] H. F. Taylor and C. E. Lee. Apparatus and method for fiber optic intrusion sensing. March 16 1993. US Patent 5,194,847.

[57] R. Juškaitis, A. M. Mamedov, V. T. Potapov, and S. V. Shatalin. Interferometry with rayleigh backscattering in a single-mode optical fiber. *Optics Letters*, 19(3):225–227, 1994.

[58] X. Liu, B. Jin, Q. Bai, Y. Wang, D. Wang, and Y. Wang. Distributed fiber-optic sensors for vibration detection. *Sensors*, 16(8):1164, 2016.

[59] J. Wang. The design of distributed fiber optic vibration sensing system–the research and design of the modified sagnac structure. Master's thesis, Huazhong University of Science & Technology, Wuhan, China, December 2011.

[60] T. Dean, A. Hartog, and B. Frignet. Seismic without sensors–distributed vibration sensing. *ASEG Extended Abstracts*, 2015(1):1–4, 2015.

[61] A. Nap. On the fidelity of distributed acoustic sensing. Master's thesis, ETH Zürich, Switzerland, 2020.

[62] K. Itoh. Analysis of the phase unwrapping algorithm. *Appl. Opt.*, 21(14):2470–2470, 1982.

[63] A. Mateeva, J. Lopez, H. Potters, J. Mestayer, B. Cox, D. Kiyashchenko, P. Wills, S. Grandi, K. Hornman, B. Kuvshinov, et al. Distributed acoustic sensing for reservoir monitoring with vertical seismic profiling. *Geophysical Prospecting*, 62(4-Vertical Seismic Profiling and Microseismicity Frontiers):679–692, 2014.

[64] B. N. Kuvshinov. Interaction of helically wound fibre-optic cables with plane seismic waves. *Geophysical Prospecting*, 64, 09 2015.

[65] M. Li, H. Wang, and G. Tao. Current and future applications of distributed acoustic sensing as a new reservoir geophysics tool. *The Open Petroleum Engineering Journal*, 8(1), 2015.

[66] Z. Tian, L. Yu, X. Sun, and B. Lin. Damage localization with fiber bragg grating lamb wave sensing through adaptive phased array imaging. *Structural Health Monitoring: An International Journal*, 18:147592171875557, 02 2018.

[67] E. Castongia, H. F. Wang, N. Lord, D. Fratta, M. Mondanos, and A. Chalari. An experimental investigation of distributed acoustic sensing (das) on lake ice. *Journal of Environmental and Engineering Geophysics*, 22(2):167–176, 2017.

[68] M. C. Fenta, D. K. Potter, and J. Szanyi. Fibre optic methods of prospecting: A comprehensive and modern branch of geophysics. *Surveys in Geophysics*, 42(3):551–584, 2021.

[69] K. L. Feigl and P. Team. Overview and preliminary results from the porotomo project at brady hot springs, nevada: Poroelastic tomography by adjoint inverse modeling of data from seismology, geodesy, and hydrology. In *42nd Workshop on Geothermal Reservoir Engineering*, pages 1–15. Stanford University, Stanford, CA, 2017.

[70] M. P. Isken, S. Heimann, C. Wollin, H. Bathke, and T. Dahm. Lightguide - seismological tools for das data. `https://doi.org/10.5281/zenodo.6580579`, 2022. Accessed: 2023-04-27.

[71] M. P. A. van den Ende, I. Lior, J.-P. Ampuero, A. Sladen, A. Ferrari, and C. Richard. A self-supervised deep learning approach for blind denoising and waveform coherence enhancement in distributed acoustic sensing data. *IEEE Transactions on Neural Networks and Learning Systems*, 0, 2021.

[72] O. Ronneberger, P. Fischer, and T. Brox. U-net: Convolutional networks for biomedical image segmentation. In *Medical image computing and computer-assisted intervention–MICCAI 2015: 18th international conference, Munich, Germany, October 5-9, 2015, proceedings, part III 18*, pages 234–241. Springer, 2015.

[73] J. O. Smith. *Mathematics of the discrete Fourier transform (DFT): with audio applications*. Julius Smith, 2008.

[74] M. A. Fischler and R. C. Bolles. Random sample consensus: a paradigm for model fitting with applications to image analysis and automated cartography. *Communications of the ACM*, 24(6):381–395, 1981.

[75] D. Kraft. A software package for sequential quadratic programming. *Forschungsbericht- Deutsche Forschungs- und Versuchsanstalt fur Luft- und Raumfahrt*, 1988.

[76] D. W. Rieken and D. R. Fuhrmann. Generalizing music and mvdr for multiple noncoherent arrays. *IEEE Transactions on Signal Processing*, 52(9):2396–2406, 2004.

[77] W. Zhu and G. C. Beroza. Phasenet: a deep-neural-network-based seismic arrival-time picking method. *Geophysical Journal International*, 216(1):261–273, 2019.